UNIVERSITY OF CALIFORNIA SAN DIEGO

Molecular Assisted Recombination Processes in N_2 Seeded D Plasmas

A dissertation submitted in partial satisfaction of the
requirements for the degree
Doctor of Philosophy

in

Engineering Sciences (Engineering Physics)

by

Shota Abe

Committee in charge:

Professor George R. Tynan, Chair
Professor Farhat N. Beg
Professor Ping Liu
Research Scientist Richard A. Moyer
Professor Clifford M. Surko

2018

The dissertation of Shota Abe is approved, and it is acceptable in quality and form for publication on microfilm and electronically:

_____

_____

_____

_____

_____

Chair

University of California San Diego

2018

DEDICATION

To my father Keiichi Abe.

TABLE OF CONTENTS

LIST OF FIGURES

LIST OF TABLES

ACKNOWLEDGEMENTS

I would like to thank all PISCES group members. Foremost, I would like to thank my academic advisor, Dr. George Tynan. I could not finish this work without his supports, thoughtful advice, and critiques. I thank Dr. Russ Doerner for helping me to do experiments very smoothly. Thank you, Dr. Saikat Chakraborty Thakur not only for his technical and scientific advice on my experiments, but for showing me his enthusiasm for educational activities. To Leo Chousal, Rollie Hernandez, and Tyler Lynch, I appreciate your assistance for anything about experimental devices which I have broken as routine. I would like to acknowledge Dr. Jonathan Yu and Dr. Michael Simmonds as PISCES-E crew. I would also like to thank Dr. Maik Sode for supporting me in using his rate-equation model.

Chapter 5, including text and data, is in part a reprint of the material as it appears in S. Abe, R.P. Doerner, G.R. Tynan, Neutralization processes of atomic/molecular deuterium ions assisted by ND_3 in low density D_2-N_2 plasmas, Physics of Plasmas, 25, 073507 (2018). The dissertation author was the primary investigator and author of this paper.

Chapter 6, including text and data, is in part a reprint of the material as it appears in S. Abe, S. Chakraborty Thakur, R.P. Doerner, G.R. Tynan, Hydronitrogen Molecular Assisted Recombination (HN-MAR) processes in ammonia seeded deuterium plasmas, Journal of Nuclear Materials, submitted, (2018). The dissertation author was the primary investigator and author of this paper.

Chapter 7, including text and data, is in part a reprint of the material as it appears in S. Abe, S. Chakraborty Thakur, R.P. Doerner, G.R. Tynan, Dissociative recombination process of ammonium for HN-MAR process in high density D-N plasmas, Physics of Plasmas, submitted (2018). The dissertation author was the primary investigator and author of this paper.

VITA

2010	B.S. in Physics, Kyoto Sangyo University
2012	M.S. in Nuclear Engineering, University of Tokyo
2018	Ph. D. in Engineering Sciences (Engineering Physics), University of California San Diego

PUBLICATIONS

S. Abe, R.P. Doerner, G.R. Tynan, Neutralization processes of atomic/molecular deuterium ions assisted by ND_3 in low density D_2-N_2 plasmas, Physics of Plasmas, 25, (2018) 073507.

S. Abe, S. Chakraborty Thakur, R.P. Doerner, G.R. Tynan, Hydronitrogen Molecular Assisted Recombination (HN-MAR) processes in ammonia seeded deuterium plasmas, Journal of Nuclear Materials, submitted, (2018).

S. Abe, S. Chakraborty Thakur, R.P. Doerner, G.R. Tynan, Dissociative recombination process of ammonium for HN-MAR process in high density D-N plasmas, Physics of Plasmas, 25, (2018).

ABSTRACT OF THE DISSERTATION

Molecular Assisted Recombination Processes in N_2 Seeded D Plasmas

by

Shota Abe

Doctor of Philosophy in Engineering Sciences (Engineering Physics)

University of California San Diego, 2018

Professor George R. Tynan, Chair

The new molecular assisted recombination [MAR] of hydrogen plasmas supported by ammonia is investigated and presented throughout this work. The plasma detachment scheme has been considered to be a practical approach to drastically reduce the harsh heat flux to prevent severe damage onto the divertor plates. In the detached divertor plasma operation, the plasma from the fusion core loses its energy by the radiation loss in the upstream divertor region, and is recombined before it touches the divertor plate in the downstream region, with help of impurity gas seeding. Nitrogen is the strong candidate of cooling gas species, and forms compounds with hydrogen i.e. ammonia. This hydronitrogen-enhanced MAR [HN-MAR] process would occur throughout two steps: 1) charge or ion exchange reactions between hydrogen ions and ammonia

molecules, 2) recombination reactions between NH_3^+ or NH_4^+ ions and electrons.

In this work, the HN-MAR process including those 2 steps is studied combining experiments and rate equation model. The PISCES-E plasma device is used to make plasmas ($n_e \sim 10^{16} - 10^{18}$ m^{-3}, $T_e \sim 3 - 4$ eV) with D_2, N_2, ND_3, and Ar gas feeding. As the 1st step of HN-MAR, the formation processes of ND_3^+ and ND_4^+ are investigated in low density D-N plasmas ($n_e \sim 10^{16}$ m^{-3}). The model shows that dominant neutralization channel of D^+, D_2^+, and D_3^+ in the volume is the creation process of ND_3^+ and ND_4^+ throughout the charge or ion exchange reactions with ND_3. The 2nd step of HN-MAR is studied using high density D-N-Ar plasmas ($n_e \sim 10^{17} - 10^{18}$ m^{-3}), in which the recombination process of ND_3^+ and ND_4^+ cannot be negligible comparing to the wall loss. The result shows that, as the plasma density is increased to these larger values, the ND_4^+ density fraction undergoes a drastic decrease in good agreement with a 0-d chemical kinetics model. These results provide evidence for the dissociative recombination reactions in the HN-MAR process. Finally, it is strongly suggested that the HN-MAR process is major chemical reactions in our D-N plasmas.

Chapter 1

Introduction

1.1 Fusion

The sun, powered by fusion reactions, is the energy source for the earth. The total energy irradiated onto the earth is 174 petawatts while a typical power plant has a capacity of the order of a gigawatt. In the sun's core, the gravity confines high density, 150 g/cm^3, and high temperature, 15.7 million kelvins, fuel in a highly ionized state known as *plasma*. In such high pressure and temperature condition, the kinetic energy of hydrogen nucleus (proton) becomes high enough to overcome coulomb force so that the protons can get close enough so that nuclear forces overwhelm the coulomb repulsion, allowing nuclear fusion reactions to then occur. Controlled thermonuclear fusion has been investigated and developed since 1950s to realize sustainable energy source. Because it has the highest probability of occurring at lower temperatures of 10 keV or so, in the 1st generation of nuclear fusion reactors the reaction below is expected to be used

$$ {}^{2}_{1}\mathrm{D} + {}^{3}_{1}\mathrm{T} \rightarrow {}^{4}_{2}\mathrm{He}(3.5\ \mathrm{MeV}) + {}^{1}_{0}\mathrm{n}(14.1\ \mathrm{MeV}) \tag{1.1} $$

This reaction between deuterium and tritium (which are isotopes of hydrogen) has a higher fusion cross section rate for low kinetic energy (< 100 KeV) than other reactions such as D-D,

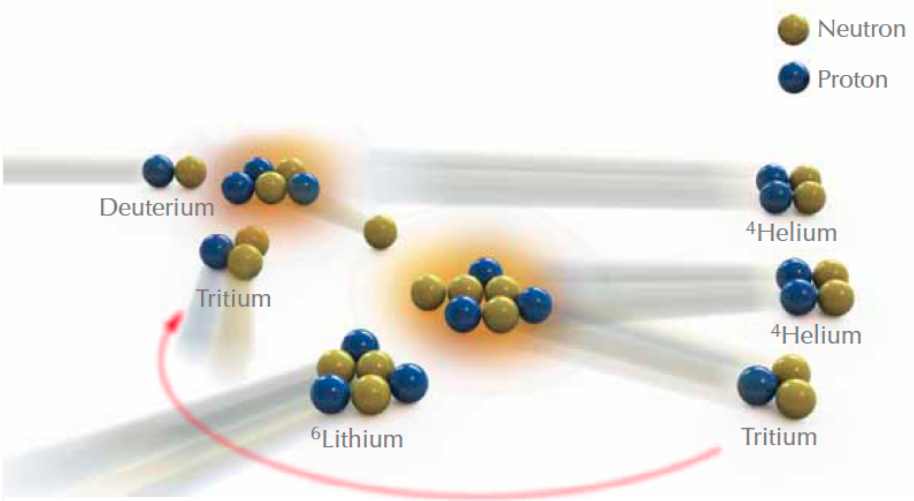

Figure 1.1: D-T nuclear fusion reaction and tritium breeding. [73]

D-^{3}He, p-^{11}B, and so on. The fusion fuel, deuterium, exists in nature with a natural abundance of 0.0156%, so that e.g. 10 kg of water contains 1.5 g of D_2O. The other fusion fuel, tritium, is a radioactive material with a half-life of 12.6 years, and so is extremely rare on Earth. However, it can be bred by irradiating lithium that is held in a blanket that surrounds the plasma by neutrons produced by the fusion reaction (eq. (1.1)). Fig. 1.1 depicts the fusion reaction and tritium breeding. The energy production from those fuels of 1 g is equivalent to the energy produced by using oil of 8 ton which is relevant with the energy consumption per capita in US (7 ton in 2011). Because fusion does not produce long lived fission products, has relatively abundant fuel resources in nature, and does not emit CO_2 into the atmosphere, there is strong global interest in its development.

The key parameter to evaluate performance of nuclear fusion reactors is the triple product of density n_e, plasma temperature T, and confinement time τ_E: $nT\tau_E$. The Lawson criterion is the minimum required triple product

$$nT\tau_E > 5 \times 10^{21}\ \mathrm{m^{-3}s\ keV} \tag{1.2}$$

needed to achieve ignition conditions in which the rate of plasma heating by the fusion products

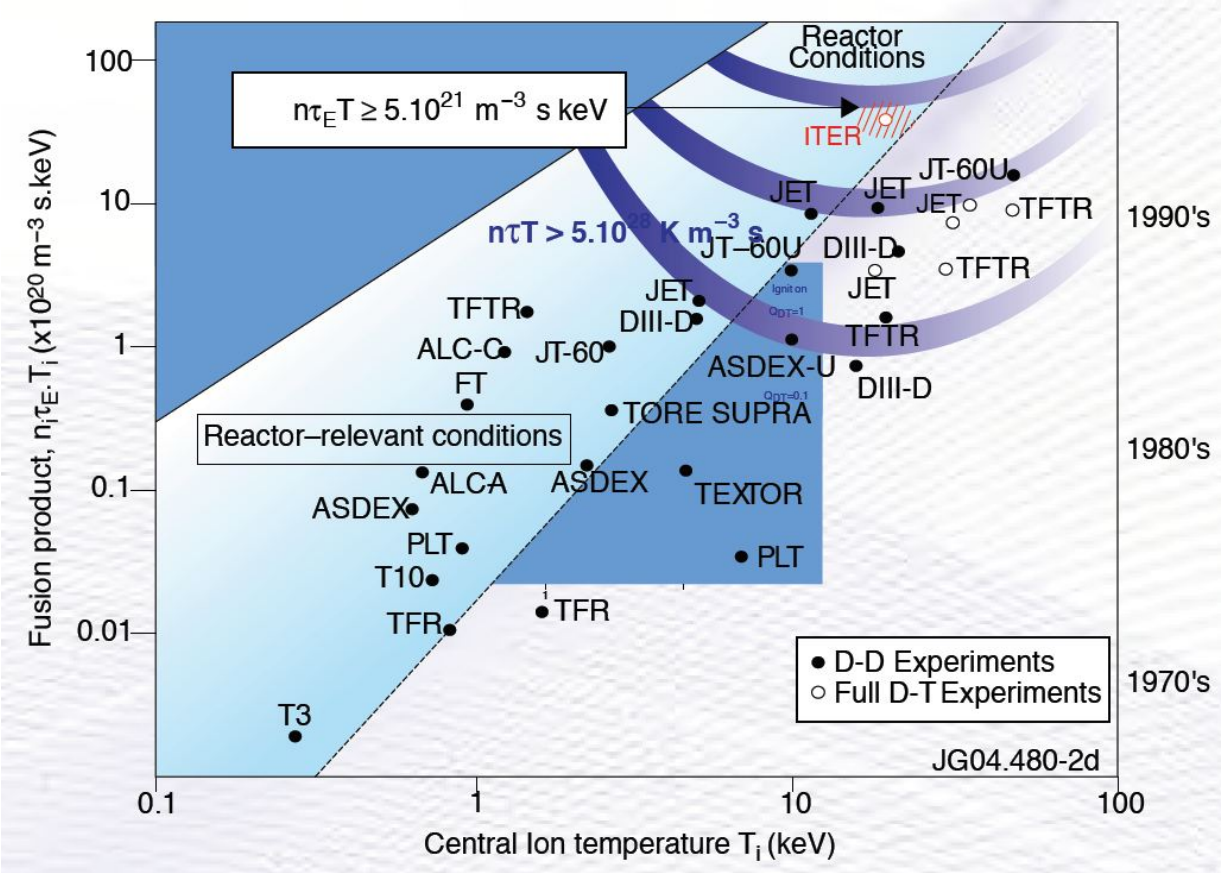

Figure 1.2: Fusion triple product achieved on different magnetic fusion facilities as a function. [73]

becomes sufficiently high to sustain the conditions for fusion reaction without external power input. There have been several methods developed to achieve this criterion. The confinement scheme that is closest to achieving this parameter is called the *tokamak* (fig. 1.2). Tokamak devices consist of a toroidally shaped vacuum chamber in which a sufficiently strong magnetic field along the toroidal direction (fig. 1.3) confines plasma so as to not come in close contact the chamber walls (however as we will see, the plasma does inevitably interact with some of the wall surface). Along the toroidal magnetic field, plasma electrons move along the toroidal direction by the imposition of a (weak) toroidal electric field and carry an electrical current in the toroidal direction. This plasma current forms another magnetic field along the poloidal direction. Those two magnetic fields then form a twisted magnetic field that threads the torus and which prevent

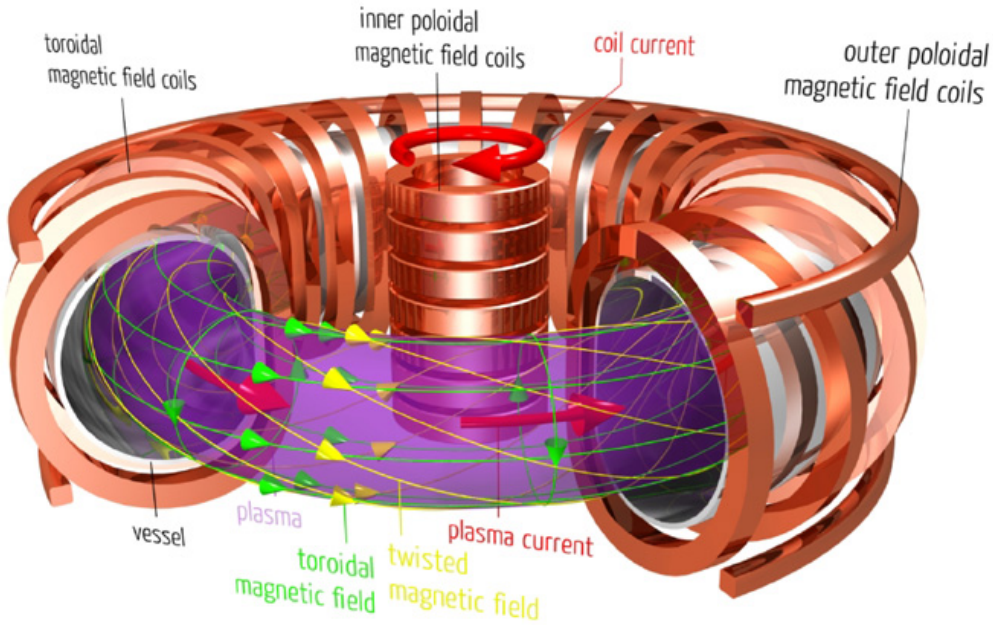

Figure 1.3: Magnetic fields and coils in a tokamak device. (Image courtesy of Max Planck Institute for Plasma Physics)

the escape of particles drifting due to the nonuniform toroidal field which varies like $1/R$, where R denotes the major radius. As an example of the achievements made by tokamak devices, in the JET tokamak, the fusion energy gain factor, which is a ratio between output power and input power, marked slightly above the breakeven $Q_{\mathrm{DT}} = 1.14$ [86]. The JT-60 tokamak also achieved $Q_{\mathrm{DT}} = 1.25$ [32]. Here Q_{DT} is the equivalent fusion multiplication factor estimated by replacing the actual deuterium-deuterium reactions with an assumed tritium-deuterium reactions [31]. However, even though Q value exceeds the breakeven, plasmas cannot be in ignition condition unless $Q \sim 10$.

1.2 ITER and DEMO

The ITER (International Thermonuclear Experimental Reactor) has been under construction since 2013, and aims to to achieve the first plasma in 2025, and start high power deuterium-tritium operation in 2035 [82]. The primary objective of the ITER is to achieve the

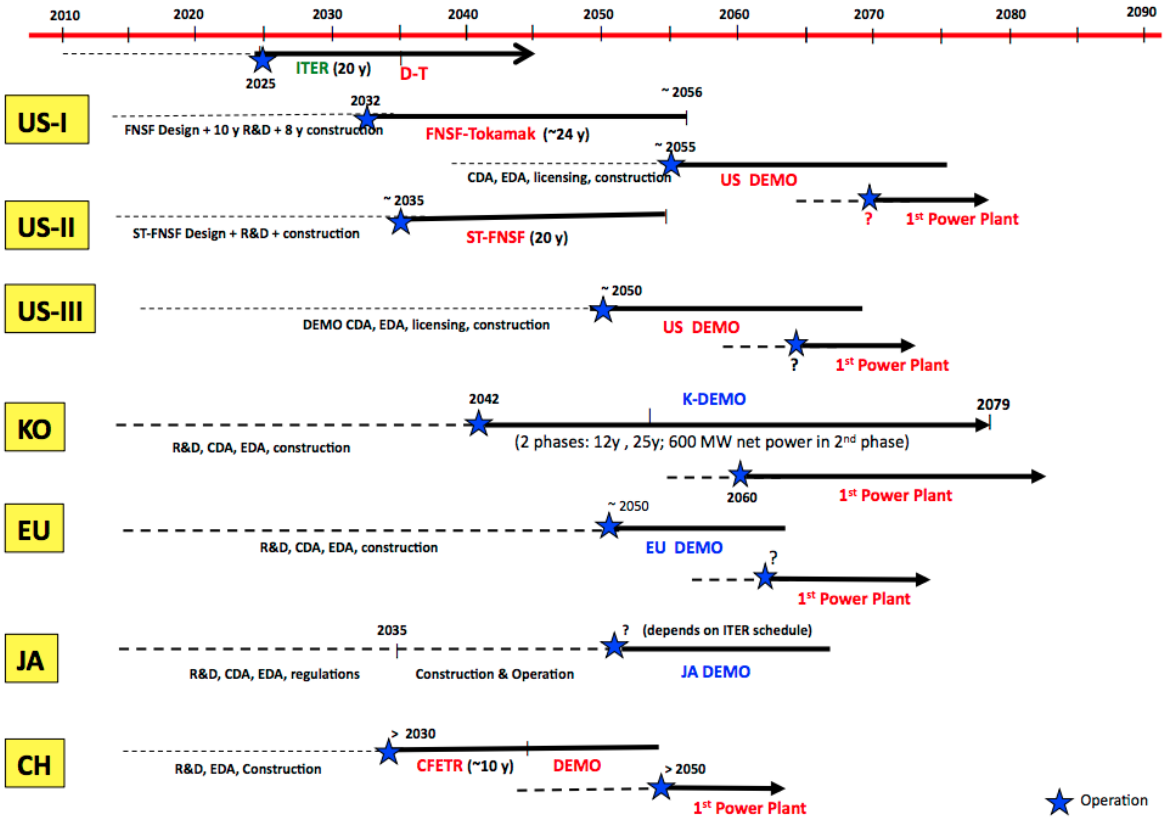

Figure 1.4: Timeline for international fusion roadmaps. [28]

Lawson Criterion (eq. (1.2)) with fusion energy gain factor $Q \geq 10$, producing 500 MW of fusion power from injected thermal power of 50 MW. In a toroidal chamber (major radius of 6.2 m and minor radius of 2.0 m), a toroidal magnetic field of 5.3 T will be formed by the largest and most integrated superconducting magnet system ever built. To obtain an initial glimpse into steady state burning plasma operation, a long pulse ($\leq$ 1000 s) plasma discharge is planned. The divertor plates are located on lower region of the chamber. As described in more detail later on, the divertor region will receive a severe ($\sim$ 10 MW/m^2) heat flux from the plasma. The ITER divertor targets will be made of tungsten (W) because of its high melting point, ability to withstand high steady-state and transient heat fluxes, its low plasma sputtering yield and its low retention of hydrogenic species.

DEMOnstration power plant concepts, or DEMO, are under study by each country participating in ITER as successor of ITER (fig. 1.4). These so-called DEMO reactors are

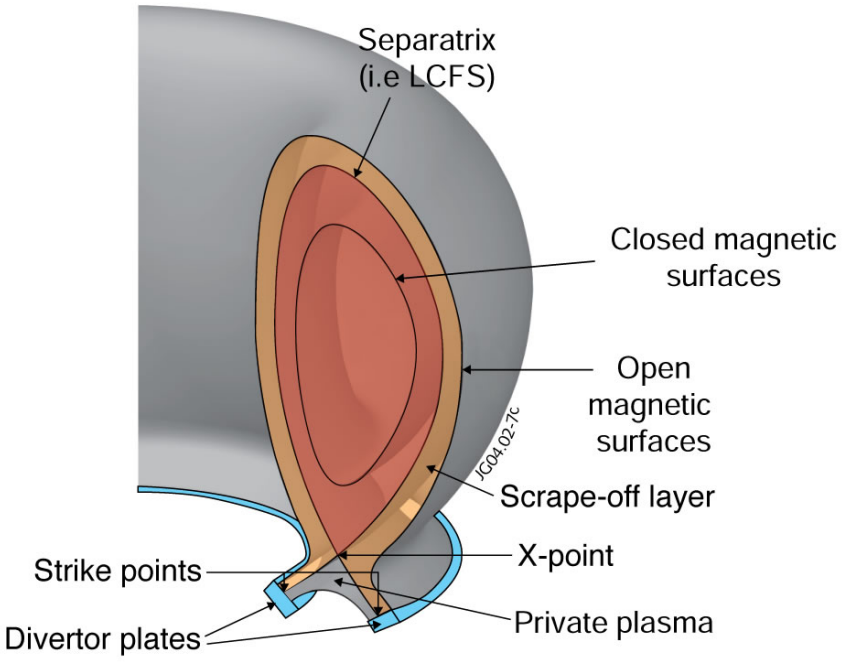

Figure 1.5: Schematic figure showing poloidal cross section of a typical tokamak device.

intended to make electricity to demonstrate the fusion can be used as a reliable power source. The DEMO is supposed to have to achieve the output power of 2 GW on a continuous basis while $Q \geq 25$ [26]. This DEMO power scale of $2-4$ GW is relevant to an electric power plant currently in use.

1.3 Heat flux onto the divertor

After the fusion reactions occur, the helium product (also called helium-ash), must be exhausted from the reaction chamber. The impurities generated in the plasma edge region also need to be removed before too many of them move into the core plasma. For that purpose, in tokamak and other toroidal helical devices a set of special poloidal field coils magnets are used to ”peel off”, or *divert* the magnetic fields lines, and form a region of open magnetic field known as the scrape-off layer [SOL] (fig. 1.5). The interface between the SOL and the core plasma is then known as the separatrix (i.e. Last Closed Flux Surface [LCFS]) and has one or more ”X-points”

that form between the divertor region and the core plasma. The SOL then brings plasma to the divertor target plates located on the end of the opened magnetic field. Because of the high ratio of parallel transport to perpendicular transport, the particle and heat flux escaping to the divertor target is concentrated in a thin region with a characteristic thickness at the outboard midplane measured in a cm or less. For sustained operations, the ITER Organization (IO) requires the design of the W divertor to withstand a heat flux of **10 MW/m^2** during steady state operation and 20 MW/m^2 during slow transient event (up to 10 s) [37]. In ITER, the plasma themal power entering the SOL from the core region is expected to be about 100 MW [60]. It is reported that $50-60\%$ of the entering power can be quenched by the radiation loss from the SOL and edge plasma region, while the much of the remaining power flux to the divertor target can be reduced by introducing so-called *detached plasma* operation. In DEMO reactors, the plasma power entering the SOL is expected about 300 MW/m^2 and therefore the cooling process of the divertor plasma becomes an even more important and critical issue that needs to be solved.

1.4 Detached plasma operation

The detached plasma operation mode is considered necessary to solve the heat flux problem of ITER divertor [68] because it drastically reduces particle and heat fluxes to the wall [58]. Detachment fundamentally involves inducing the volumetric recombination of divertor plasma before it reaches the divertor target [56]. Detailed research about detachmented divertor operation were carried out in 1990s [68]. In that work [68] the *plasma detachment* is defined as "state in which large pressure gradients (static plus dynamic) are observed parallel to the magnetic field with consequently low plasma power and ion fluxes to the material surfaces bounding the system". To prevent damage onto the divertor plate, the divertor detachment operation is a key element of the ITER baseline design. The question then of course emerges: how can one reliably induce divertor plasma detachment in the ITER device?

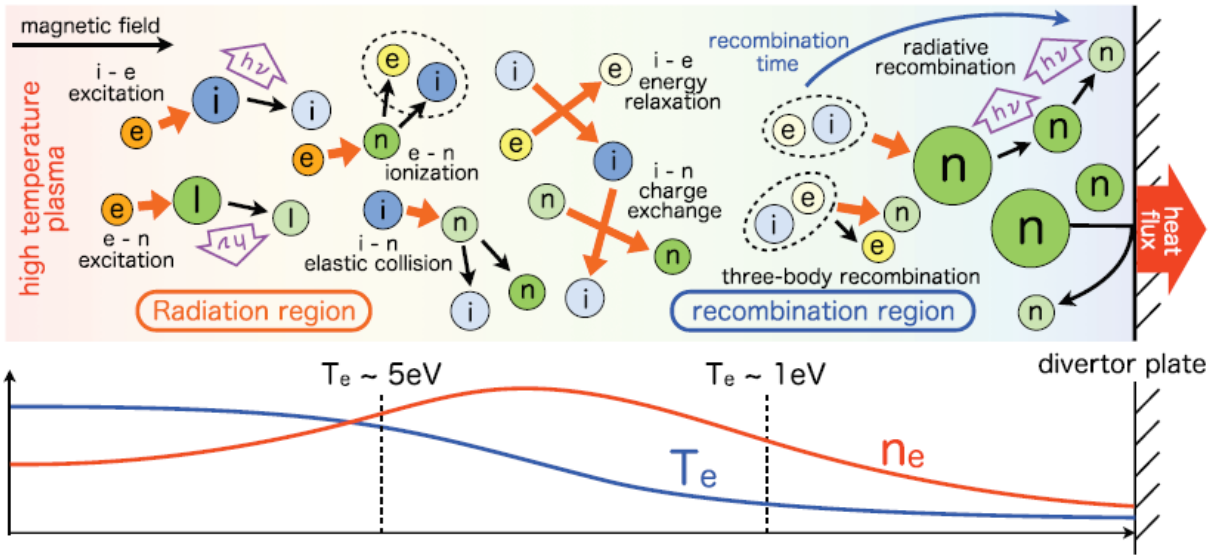

Figure 1.6: Helium divertor plasma cooling scheme. [36]

1.5 Impurity seeding into the divertor plasma

In order for detachment to occur, obviously the hot plasma ($T_e \sim 100$ eV) entering the divertor region from the SOL region has to be cooled down to the point (< 1 eV) where recombination can occur. This is generally difficult to achieve via injection of hydrogenic species alone, as the required neutral gas densities would be unacceptably high. As a result, impurity seeding of nitrogen (N_2), neon (Ne), or argon (Ar) into the divertor plasma is being studied as a mean to enhance the radiation loss and induce plasma detachment for protecting the tungsten divertor target from heat loads in future Tokamak devices [44][87]. The effects of N_2 seeding in divertor region have been investigated in Tokamak devices such as ASDEX Upgrade [48] [74] and JET [77] and is considered a fairly well-established divertor plasma cooling technique. Fig. 1.6 shows schematic description of the divertor plasma cooling process. In the upstream region with high temperature $T_e > 10$ eV, the radiation loss due to Bremsstrahlung and line emissions initially cools down the plasma. It has been reported that N seeding enhances radiation loss within the SOL and divertor plasma region [12], and, for reasons that are not fully understood, improves core plasma confinement time [13][74]. Fig. 1.7 shows radiation distribution of nitrogen seeded

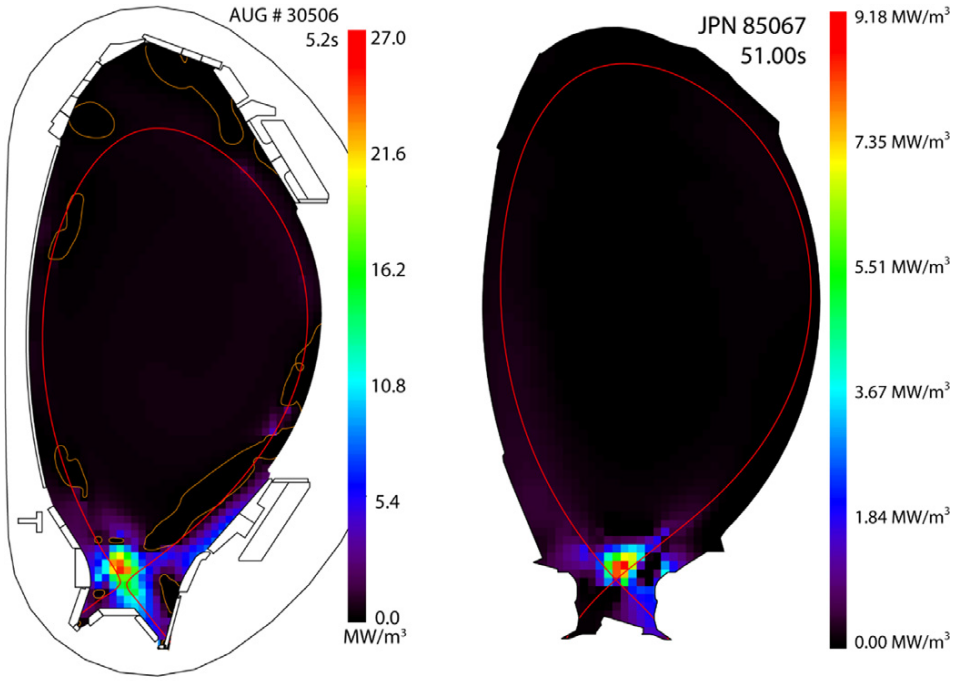

(a) AUG (b) JET

Figure 1.7: Radiation distribution of nitrogen seeded discharges at AUG and JET in the detached state. [12]

discharges in AUG and JET plasmas operating in the detached state [12], where 18 MW of heating power are applied forming H-mode plasmas. In the AUG discharge with a constant N seeding rate (shot #30506), the radiation distribution (fig. 1.7(a)) shows the radiative cooling takes place around the X-point while in the divertor plasma is in a detached state. The radiated power fraction ($f_{\text{rad}} = P_{\text{rad}}/P_{\text{heat}}$) in this discharge is around 75%. Fig. 1.7(b) showthe radiation distribution in the JET pulse discharge (JPN 85067). Again, the strongest radiative power density is located around the X-point when the divertor plate is in fully detached state, and the radiated power fraction is also around 75%. Fig. 1.8 shows time variations of key discharge parameters in AUG-W discharges with nitrogen seeding. In fig. 1.8(a), the confinement enhancement (H-factor) H_{98} increases from 0.8 to 1.2 after nitrogen injection at 2.5 s while the normalized pressure increases from β_N from 2 to 2.8. Here an H-factor of 1 denotes a thermal core plasma confinement given by the H-mode empirical scaling law. In fig. 1.8(b) [13] the experiment is repeated keeping the normalized plasma beta, $\beta_N \sim 2-2.4$, below the MHD limit. In this case, H_{98} also increases

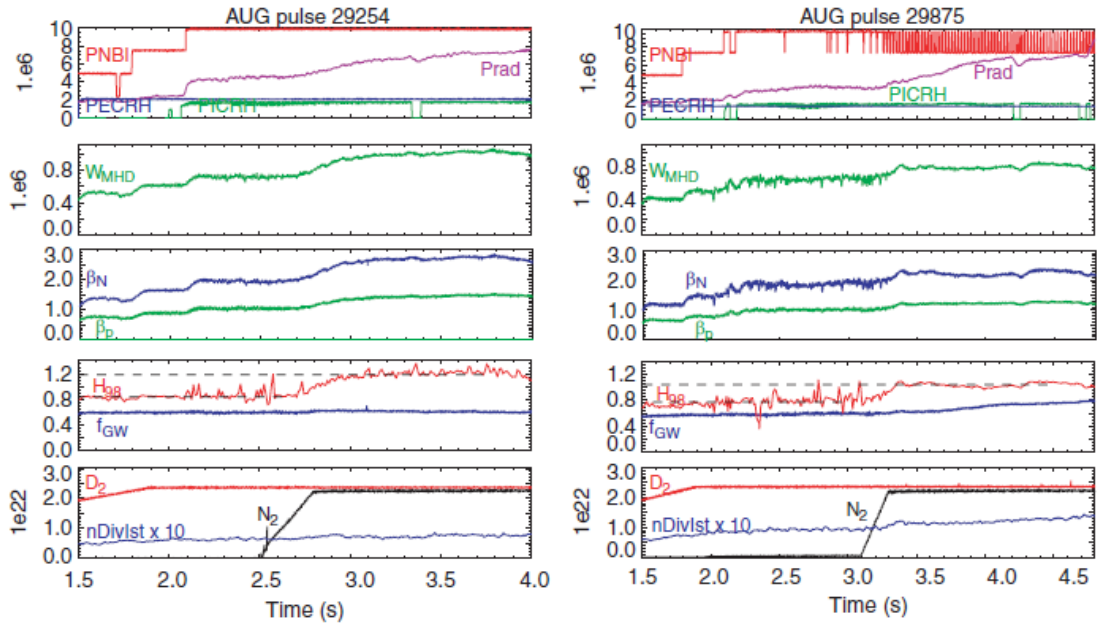

Figure 1.8: Key parameters variations of 2 pulse discharges (shot #29254 and #29875) in AUG-W with nitrogen seeding while the normalized pressure β_N is kept constant in AUG pulse #29875 (right). [13]

from 0.8 to 1.0 as soon as the nitrogen is seeded at 3 s. The N seeding is also observed to change the edge localied mode (ELM) characteristics, reducing their amplitude by a factor of 2-3 and increasing their frequency [92]. Both of these responses then reduce the magnitude of the transient thermal heat flux carried by the ELM events. While several experiments in Tokamak devices show positive results about plasma cooling, the detailed detachment processes and plasma chemical kinetics that lead to the plasma recombination in these N impurity seeded plasmas are not well understood yet. Therefore, the detailed studies using laboratory experiments with theoretical and numerical analysis can help provide deeper understanding of these processes.

1.6 Ammonia formation in Tokamak plasma devices

While N_2 seeding shows good results in Tokamak plasmas for its demonstrated ability to effectively cool the divertor plasma while yielding improved core thermal confinement, N_2 is chemically reactive and thus nitrogen and hydrogen containing compounds such as ammonia

have been observed to form [105]. ASDEX-Upgrade is the one of devices which have reported ammonia formation under fusion-relevant conditions [75][88]. ASDEX-Upgrade has stainless steel as the vacuum vessel wall and tungsten plasma-facing components and divertor plates. After two nitrogen-seeded discharges that formed stable detached H-mode plasmas for several seconds, 8% of the seeded nitrogen atoms were detected in the form of ammonia molecules. The interaction of ammonia with the tungsten plasma wall was observed as well. A strong retention of the injected nitrogen inventory was observed, with up to 30% of injected nitrogen missing after the discharges were completed and all residual gas was evacuated. In the JET, the other fusion-relevant device reporting ammonia formation, 30% of injected nitrogen is also missing. They could not measure ammonia molecules directly by a residual gas analyzer because of overlap by deuterated water and methane molecules which have same mass with deuterated ammonia. Using a gas balance analysis, the authors of the JET work concluded the 15-30% of injected nitrogen was converted to ammonia molecules. These ammonia molecules can then be trapped in the divertor cryopump [89]. Furthermore, the decomposition of ammonia via the formation of $W_xN_yH_z$ compounds on W-based material surfaces has also been reported [83][69][34]. These compounds may be difficult to remove and, as a result, the formation of ammonia in the chamber can impact the key issues of tritium retention and in-vessel inventory.

Motivated by these considerations, this dissertation reports studies of the chemical kinetics of nitrogen seeded deuterium plasmas under conditions that are relevant to those found in tokamak divertor plasmas. The principal finding is that N-injections into D-fueled plasmas leads to the formation of ammonia-based ions which then act to catalyze D-plasma recombination and thereby enhance the recombination at electron temperatures of a few eV. The results validate a chemical kinetics model of N-D plasma mixtures, and suggest that the direct injection of ammonia instead of nitrogen may lead to a more efficient detachment scheme in the tokamak divertor region.

Chapter 2

Previous research on ammonia formation, molecular assisted recombination, global model, and *in-situ* plasma mass spectroscopy

2.1 Ammonia formation in laboratory experiments

The formation processes of these compounds in N_2 seeded hydrogen plasmas have been studied in laboratory researches of both N-H mixed low-pressure plasmas [20][97][24] and atmospheric-pressure N-H plasmas [41]. Those articles reported that the ammonia is mainly formed on the metal surface of the reactor mediated via plasma catalysis effects, the successive hydrogenation of atomic nitrogen and nitrogen containing radicals [20][41] (fig. 2.1). In particular, these workers reported that the ammonia production process on the surface includes two types of

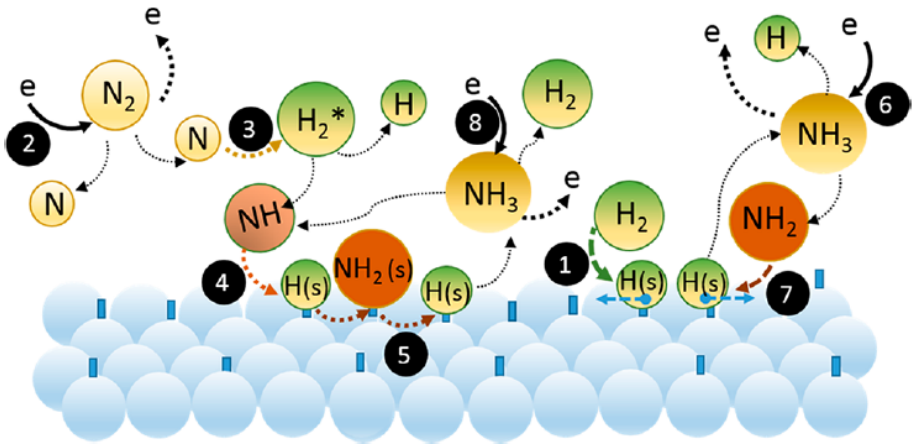

Figure 2.1: Schematic depicting formation mechanism of ammonia. (5) reaction shows NH_3 production by L-H mechanism (eq. (2.1)). [41]

mechanisms. As shown in fig. 2.1, the first type of mechanisms is Langmuir-Hinshelwood (LH)

$$NH_2(s) + H(s) \rightarrow NH_3 \tag{2.1}$$

which is also a step in the Harber-Bosch process, the main industrial ammonia procedure since 1913. '(s)' in the equation stands for materials absorbed on the surface. The second type provided by the plasma synthesis is Eley-Rideal (ER)

$$NH_2 + H(s) \rightarrow NH_3 \tag{2.2}$$

$$H_2 + NH(s) \rightarrow NH_3 \tag{2.3}$$

$$H + NH_2(s) \rightarrow NH_3. \tag{2.4}$$

As we can see in the equations, the molecular radicals produced in the plasma volume play an important role to form ammonia, but the final formation step itself is a surface reaction.

Carrasco *et al.* [20] measured ammonia formation in H-N mixed discharges. The plasma device consists of a grounded cylindrical stainless-steel vessel (10 cm diameter, 34 cm length) and a central anode that was used to generate a DC discharge. Using a total pressure of 6 mTorr,

0.6 mTorr nitrogen gas was mixed with hydrogen gas. The plasma parameters realized by the DC discharge were $T_e = 3.8$ eV and $n_e = 2.6 \times 10^{16}$ m^{-3}. They reported about 25% of injected nitrogen was transformed to the form of ammonia. According to the model calculation including kinetic reactions in gas-phase and on surface, they found that both ER and LH mechanisms were necessary to account for the measured distributions of neutrals while the gas phase volume reactions alone cannot produce such amount of ammonia. Sode *et al.* [97] investigated ammonia formation and chemical plasma reactions in H-N-Ar mixed discharges. The device consists of stainless steel plasma chamber (25 cm diameter, 36 cm height) with a planar coil separated from the vacuum by a quartz dome to produce an RF discharge (13.46 MHz, up to 600 W). Using a total pressure of 11 mTorr and an Ar fraction of $1.2 - 1.5\%$, the nitrogen fraction varied from 0.02% to 56%. The maximum fraction of ammonia, $f_{NH_3} = 10\%$, was found for $f_{N_2} = 20\%$ in the RF power discharge of 200 W. However, the ammonia formation did not increase much even when nitrogen fraction was increased up to 56%. It was speculated that this may be due to the wall becoming saturated by hydrogen/nitrogen radicals at certain fraction range of nitrogen in the volume. Again, the experiments were in a regime where wall-mediated reactions played a key role in the kinetics - a regime that is somewhat different than what is expected to occur in detached divertor operations.

2.2 Molecular assisted recombination for detachment plasma operation

In the downstream region in the divertor plasmas $T_e < 10$ eV shown in fig. 1.6, the volumetric recombination process would take place to introduce further plasma cooling and induce the plasma detachment operation scheme. The Molecular Assisted Recombination [MAR] process is important in fusion plasma detachment operation since it is thought to be a main channel of volumetric recombination of the divertor plasmas [63][16][110]. We provide a brief

summary of this process below.

2.2.1 Molecular assisted recombination [MAR]

Radiative and three-body recombination of hydrogen atomic ions with electrons can occur in regions where electron temperature is $T_e = 0.3$ eV or lower. It has been predicted and reported that the molecular assisted recombination [MAR] process mediated by hydrogen molecule enhances the plasma recombination rate [57]. The MAR process would occur in a relatively higher temperature range where $T_e < 2$ eV. On the other hand, Janev [45] predicted another type of recombination process supported by hydrocarbon molecules of the type C_xH_y. This process would occur in the temperature range of $T_e < 8$ eV due to faster dissociative recombination rate of $C_xH_y^+$ which is formed by charge exchange reactions between hydrogen ions and C_xH_y molecules than recombination rate of H^+. Let us examine these MAR processes in more detail.

2.2.2 Hydrogen molecular assisted recombination [H-MAR]

The MAR process was originally proposed to be associated with vibrationally excited hydrogen molecules [57]. The two schemes of processes are represented as follows;

$$H_2(v) + e \rightarrow H^- + H \tag{2.5}$$

followed by

$$H^- + A^+ \rightarrow H + A \tag{2.6}$$

(charge exchange recombination), and

$$H_2(v) + A^+ \rightarrow AH^+ + H \tag{2.7}$$

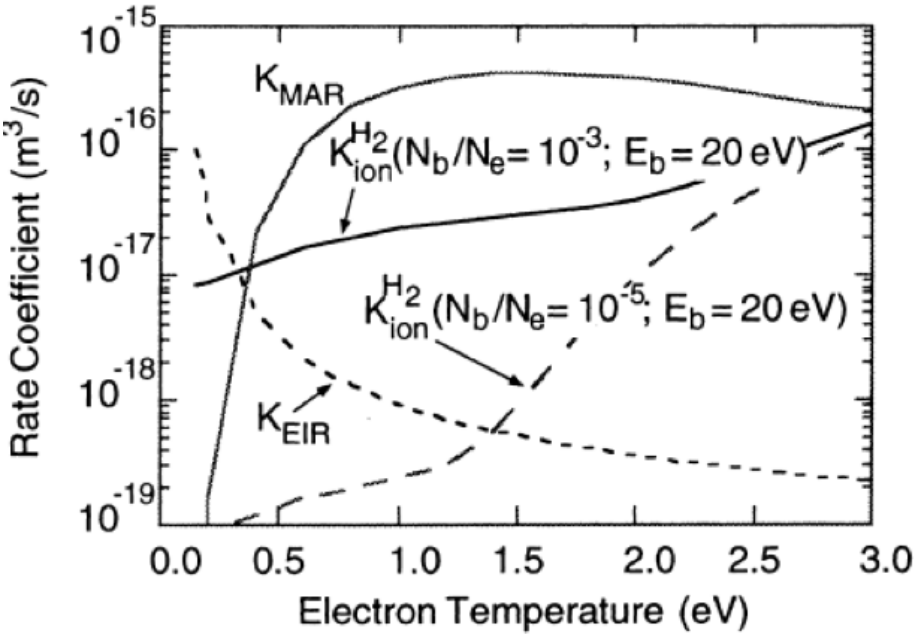

Figure 2.2: Rate coefficients of collisional processses as a function of electron temperature calculated by CRAMD code where the electron density is assumed to be 1×10^{19} m^{-3}. [30]

followed by

$$\mathrm{AH}^+ + \mathrm{e} \rightarrow \mathrm{A} + \mathrm{H} \tag{2.8}$$

(dissociative recombination), where $H_2(v)$ is the vibrationally excited hydrogen molecules and A^+ is an atomic ion in the plasma. Fig. 2.2 taken from [30] shows calculated rate coefficients of the electron-ion recombination K_{EIR} and molecular assisted recombination K_{EIR} of atomic hydrogen ion as a function of electron temperature where the electron density is assumed to be 10^{19} m^{-3}. The K_{MAR} becomes much higher than K_{EIR} for an electron temperature above 0.5 eV. Therefore, this hydrogen-enhanced MAR process [H-MAR] is the dominant recombination mechanism in the electron temperature range $0.3 - 2$ eV while the conventional electron-ion recombination [EIR] only takes place in high density ($\gg 10^{19}$ m^{-3}) and cold ($\ll 1$ eV) plasma. This MAR process was subsequently experimentally investigated in several linear divertor simulators such as NAGDIS [79] [30], MAP-II [80][81], TPD-SheetIV [67], and PISCES-A [19]. Here, some important experimental results about H-MAR are introduced. Ohno *et al.* [79] carried out the first laboratory experiment of MAR in a linear plasma device, NAGDIS. H_2 or He gas was puffed into

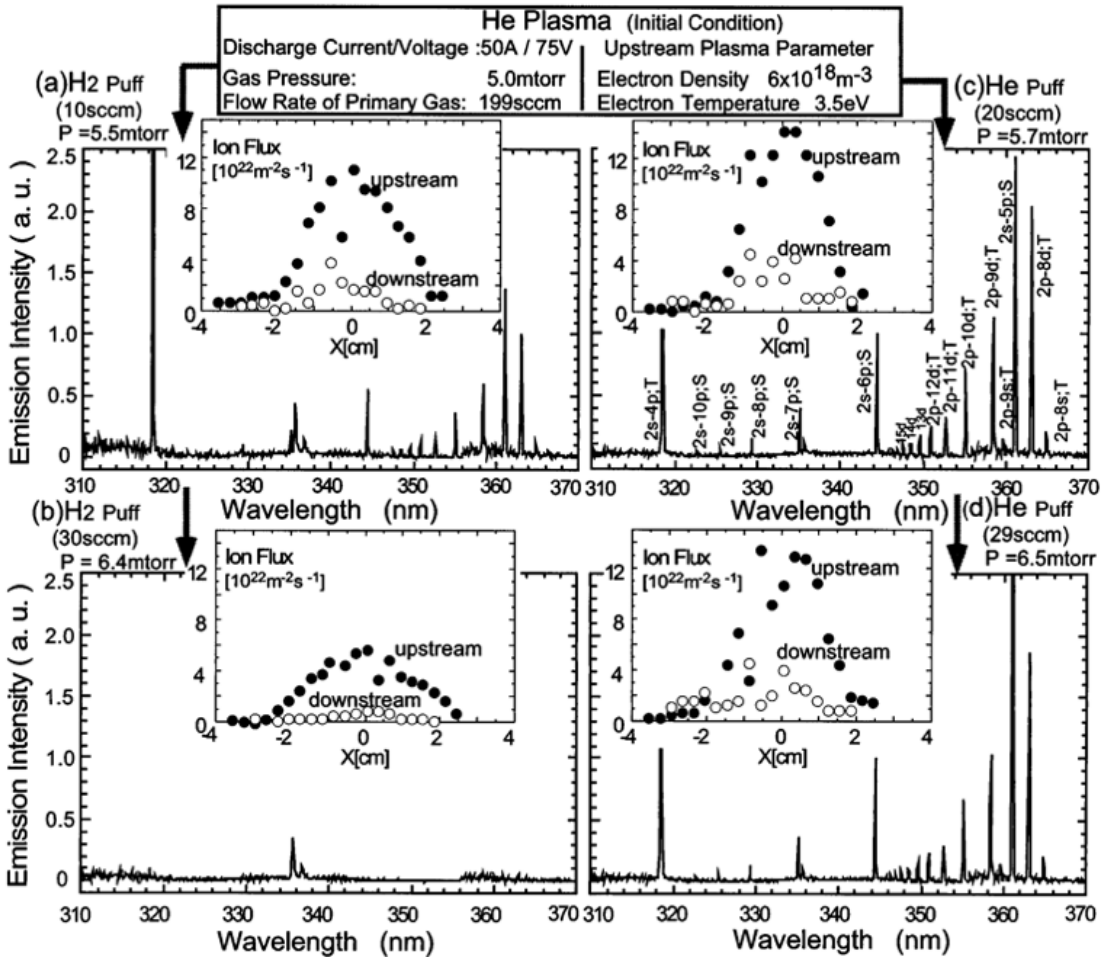

Figure 2.3: Radial profiles of the ion particle flux in the upstream (closed circle) and downstream (open circle), and visible light emission spectra from helium plasmas. [79]

a He plasma ($n_e = 6 \times 10^{18}$ m^{-3} and $T_e = 3.5$ eV) around the target plate. They observed a small amount of H_2 puffing strongly reduced the ion particle flux along the magnetic field near the target (fig. 2.3). As the evidence of MAR process, they observed disappearance of line emission intensity from the conventional EIR processes during the H_2 puffing, and interpreted this result to indicate that the recombination of the plasma during H_2 was occuring via the MAR process. Subsequently Ezumi *et al.* [30] observed the MAR process in the NAGDIS-II device where H_2 was puffed into the H_2 upstream plasmas ($n_e = 10^{19}$ m^{-3}). The reduction of the ion particle flux during the hydrogen gas puff was observed clearly as well.

2.2.3 Hydrocarbon molecular assisted recombination [HC-MAR]

Another MAR process mediated by hydrocarbon molecules was suggested by Janev *et al.* [45], and experimentally investigated in the linear divertor plasma simulator MAP-II [47]. In this process, bulk ions are neutralized through charge exchange with hydrocarbon molecules; this step is then followed by dissociative recombination of ionized hydrocarbon molecules with electrons in a higher temperature regime ($< 5 - 10$ eV). In equations, this process is represented as

$$H^+ + C_xH_y \rightarrow H + C_xH_y^+ \tag{2.9}$$

which is then followed by

$$e + C_xH_y^+ \rightarrow \sum_{k,l} C_{x\text{-}k}H_{y\text{-}l} + \hat{H}. \tag{2.10}$$

Fig. 2.4 shows rate coefficients of hydrocarbon molecules relating to the HC-MAR process. We see that these dissociative recombination rates (eq. (2.10)) are higher than the charge exchange reaction rates (eq. (2.9)) in a temperature range below $5 - 10$ eV. Therefore, the charge exchange reactions are the rate determinant in this process. Those charge exchange rates are in an order of 10^{-8} cm^3/s $=$ 10^{-14} m^3/s which is much higher than the rate of H-MAR (fig. (2.2)) about 10^{-16} m^3/s. Kado *et al.* [47] brought the experiments about the HC-MAR process in the linear divertor plasma simulator, MAP-II [Tsukuba University (formerly at University of Tokyo)]. In this work, several gas species including He, H_2, CH_4, and C_2H_6 were injected into the upstream helium plasma, and the downstream ion flux was then monitored. As shown in fig. 2.5, the ion flux was quenched in hydrocarbon gas puffing cases, especially for C_2H_6. These experiments provide controlled demonstrations of the ability of molecular gas injection to induce recombination and thus provide for plasma detachment in the downstream region of these linear devices. However, these experiments do not strongly provide insight into the underlying chemical kinetics that leads to the recombination and detachment. In order to address these questions, we next summarize

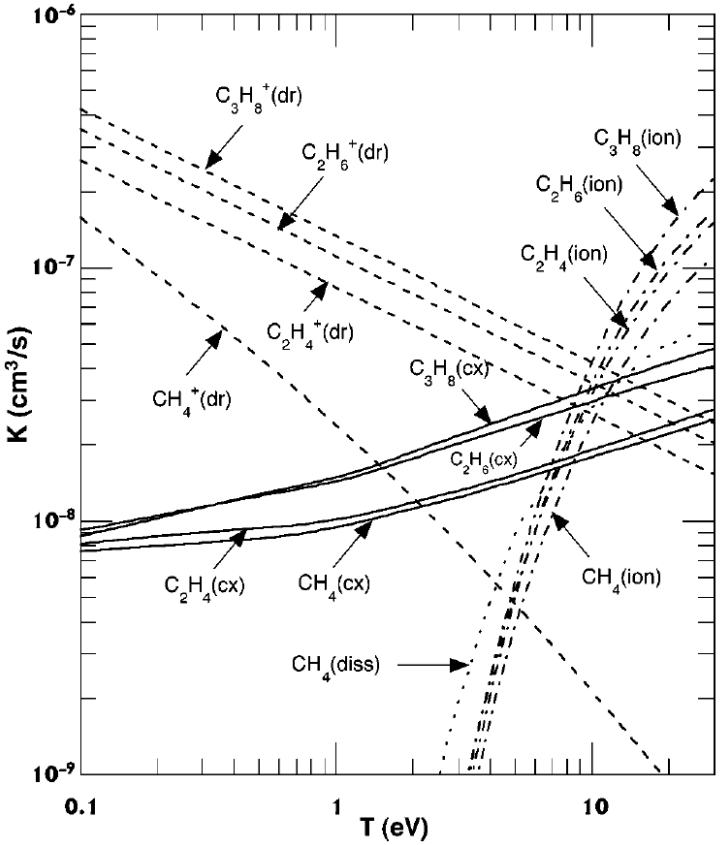

Figure 2.4: Rate coefficient of formation and deformation processes of hydrocarbon molecules CH_4, C_2H_4, C_2H_6, and C_3H_8. Solid lines: Total charge exchange (cx); dashed lines: dissociative recombination (dr); dash-dotted lines: electron-impact total ionization (ion); dotted line: dissociative excitation of CH_4 to neutrals (diss). [45]

the development of so-called global, or 0-d, models of the chemical kinetics in spatially uniform plasmas.

2.3 Global model

A zero-dimensional (volume averaged) rate equation model also known as a 'global model' is used to study the chemical reactions in plasmas fueled by D-N-Ar mixtures. This type of model has been developed, and applied to H_2 [40], H_2-Ar [53][38], and H_2-N_2-Ar plasma [97]. The model used in this dissertation is basically based on the model used in the article [97]. The model consists of the particle balance equation, based on the continuity equation, describing

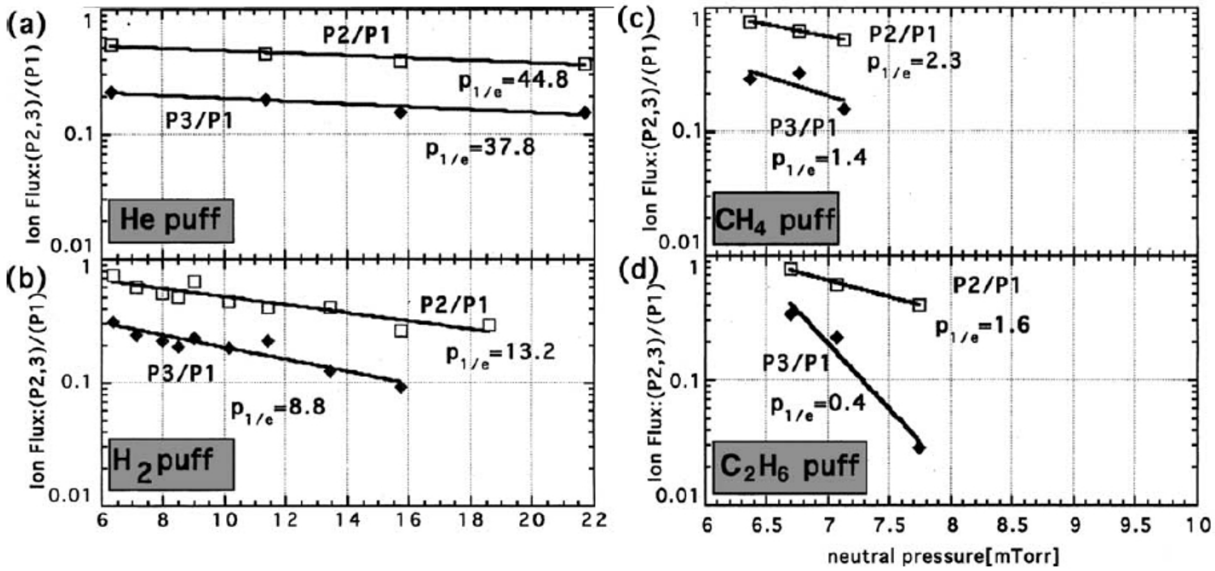

Figure 2.5: Comparison of ion flux reduction efficiency for different injected gas species. Evolution of the ion saturation current at P2 (mid-stream) and P3 (downstream), normalized to P1 (upstream), as a function for neutral pressure for injected gas species. [47]

production and loss in the volume and on the surface. By supposing steady state approximation, the rate equation of species j is represented as

$$\frac{\partial n_j}{\partial t} = 0 = R_{\text{tot}}^{j\text{S}} - R_{\text{tot}}^{j\text{L}} - X_{\text{loss}}^{j} \tag{2.11}$$

where n_j is the density, $R_{\text{tot}}^{j\text{S}}$ and $R_{\text{tot}}^{j\text{L}}$ are the total reaction rates for production (source) and loss, and X_{loss}^{j} is the wall loss rate, respectively. The source rate for a typical volumetric reaction between species k and l is

$$R_k^{j\text{S}} = n_k n_j K_{jk} \tag{2.12}$$

where K_{jk} is the rate coefficient mainly determined by experimental methods. Tables 2.1-2.7 summarize the rate coefficients used in this research. Almost all rate coefficients K_{jk} are identical to those found in the article [97]. It should be noted that these coefficients are for the hydrogen species, not the deuterium. The coefficients for recombination process are mainly taken from [20]. The rate coefficients of ion-molecular reactions are mainly obtained by experiments under the

room temperature. The loss rate for a typical volumetric reaction with species k is

$$R_k^{j\mathrm{L}} = n_k n_j K_{jk} = n_k \nu_k^{j\mathrm{L}} \tag{2.13}$$

where $\nu_k^{j\mathrm{L}} = n_j K_{jk}$ is the loss frequency. The wall loss rate is

$$X_{\mathrm{loss}}^{j} = n_j \nu_{\mathrm{w}j} \tag{2.14}$$

where $\nu_{\mathrm{w}j}$ is the wall loss frequency, which may be a function of neutral/ion species, wall materials, and wall temperature. In this research for D_2-N_2 plasma, the model includes 24 nonlinear rate equations of 12 ion species (D^+, D_2^+, D_3^+, N^+, ND^+, ND_2^+, ND_3^+, ND_4^+, N_2^+, N_2D^+, Ar^+, ArD^+), 4 neutral species (D, N, ND, ND_2), and 9 metastable nitrogen/argon species ($N(^2D)$, $N(^2P)$, N_2(a'), N_2(A), N_2(B), N_2(C), Ar(m), Ar(r), Ar(4p)). The set of 24 nonlinear equations are solved by MATLAB's 'fsolve' function by inputting input parameters such as the rate coefficients, K_{kl}, electron density n_{e}, neutral gas temperature T_{g}, neutral gas density fractions f_j during plasma discharge, total pressure p_0, and dimension of the reaction chamber. We have to note that in higher density plasma configurations the hydrogen atom D is measured and used as an input parameter (Chapter 3). The electron temperature T_{e} was treated as a free parameter in the model to achieve the quasi-neutrality $n_{\mathrm{e}} = \sum n_{\mathrm{i}}$. In this research, T_{e} is adjusted to satisfy $0.98 \leq \sum n_{\mathrm{i}}/n_{\mathrm{e}} \leq 1.02$. Finally, the calculation gives the ion and neutral densities of 24 species as solution.

2.3.1 Volumetric rate coefficient measurement methods

Almost all coefficients of dominant ion-molecule/atom reactions were obtained by **SIFT** (Selected Ion Flow Tube) [96], **ICR** (Ion Cyclotron Resonance) [42][50], and **CRESU** (Cinetique de Reactions en Ecoulement Supersonique Uniforme) methods [66][90]. In those methods,

the disappearance rates of ions injected to specific neutral gas held at room temperature is measured [42] while the T_g range is measured to lie in the range 390-910 K in our plasmas. This difference does not make significant change for the coefficients because those are usually a function of the electron temperature [98]. The rate coefficient is calculated by an equation

$$k_{ij} = < \sigma_{ij} v_{ij} > = \int\int \sigma_{ij}(v_{ij}) v_{ij} f_i(\vec{v}_i) f_j(\vec{v}_j) \mathrm{d}\vec{v}_i \mathrm{d}\vec{v}_j \tag{2.15}$$

where σ_{ij} is teh cross section, $v_{ij} = |\vec{v}_i - \vec{v}_j|$ is the absolute value of the relative velosity, and $f_i(\vec{v}_i)$ is the velocity distributions. Typically ion-molecule reactions are the ion-induced dipole scattering where σ_{ij} is proportional to v_{ij} in the low energy range up to 1.10 eV [62][9]. Therefore, the product $\sigma_{ij} v_{ij}$ in the integral is independent of $v_{ij} = \sqrt{2E_{ij}/\mu_{ij}}$, where $\mu_{ij} = m_i m_j/(m_i + m_j)$, i.e. the neutral gas temperature T_g because $E_{ij} = 1.5 k_B T_g$. The disappearance rate, τ, is a product of the neutral gas density, n, and rate coefficients, k, of the reaction, if ion density, n_i, decays exponentially as a function of time such as

$$n_i = n_i^0 e^{-nK_B t} = n_i^0 e^{-\tau t}. \tag{2.16}$$

Hence, the rate coefficient can be determined by measuring the disappearance rate. The difference between those methods are in a setup of reactions between the ions and neutrals. The cross sections for the DR process of NH_3^+ and NH_4^+ (Chapter 4) were obtained by **Merged Beam Technique** (MBT) method [17][25][109]. In this method, a mass-selected ion beam with a high kinetic energy is merged with a fast electron beam. The formed neutrals are then counted using a surface barrier detector. By tuning the velocity of the two ion and electron beams, the cross section can be determined as a function of the relative kinetic energy between the ion and electron.

2.3.2 Wall loss rate for neutrals

The effective wall loss rate X^j_{loss} for neutral species in a cylindrical chamber is estimated by the diffusion model [22][21][15]. According to the continuity equation and Fick's law,

$$\frac{1}{n}\frac{dn}{dt} = \frac{1}{n}D\nabla^2 n(j) = -\frac{D}{\Lambda^2} = -\nu_{wj} \tag{2.17}$$

where D is the diffusion coefficient, Λ is the diffusion length of the fundamental mode, and ν_{wj} is the net particle loss frequency. Λ can be determined by solving eq. (2.17) with a boundary condition, which is represented in terms of the linear extrapolation length, λ,

$$\frac{1}{n}\left(\frac{dn}{dq}\right)_b = -\frac{1}{\lambda} \tag{2.18}$$

where q represents a generalized spatial coordinate, $\lambda = \varepsilon\lambda_m(2-\beta)/\beta$, $\lambda_m = (N\sigma_m)^{-1} = 3D/\nu$, β is surface loss probability, and v is the average velocity of species j. Chantry has shown good approximation to the numerically calculated Λ for various shapes of containers such as, spherical, rectangular parallelepiped, and right circular cylinder. From that work, Λ is given as

$$\Lambda^2 = \Lambda_0^2 + \frac{V}{A}\lambda \tag{2.19}$$

where Λ_0 is the diffusion length also determined by solving eq. (2.17) but with a vanishing boundary condition $n = 0$ at the container surface. Therefore, the second term represents an effect of taking wall reflections into account (eq. (2.18)). The worst fractional error, $\Lambda_{\text{approx.}}/\Lambda_{\text{calc.}}$, for a cylinder shape container case is 9%. Then, the wall loss rate coefficient ν_{wj} of neutral radicals is given by

$$\nu_{wj} = \left(\frac{\Lambda_0^2}{D} + \frac{V}{A}\frac{(2-\beta_j)}{\bar{v}\beta_j}\right)^{-1} \tag{2.20}$$

where Λ_0 is the diffusion length, D is diffusion constant, V/A is the volume-to-surface ratio, and β_j is surface loss probability of the considered species j.

2.3.3 Wall loss rate for ions

In the unmagnetized limit, the wall loss rate ν_{wj} for ions is given by [53]

$$\nu_{wj} = \frac{2(R^2 h_l + RLh_r)}{R^2 L}\sqrt{\frac{eT_e}{m_i}}. \tag{2.21}$$

On the right hand side, the first term represents the effective surface area divided by the volume and the second term is the Bohm velocity u_B of ions hitting into the wall. The terms h_l and h_r are the center-to-edge density ratio [33][62]. Those are obtained from the steady-state ion continuity equation,

$$\nabla \cdot (n\mathbf{u_i}) = \nu_{iz} n. \tag{2.22}$$

Making the assumption that the ion drift velocity due to the electric field dominates over the velocity due to the pressure gradient, the ion drift velocity

$$\mathbf{u_i} = \mu_i \mathbf{E}. \tag{2.23}$$

Making the other assumption that the electric field is dominantly formed by the electrons, we obtain

$$\mathbf{E} = -T_e \frac{\nabla n_e}{n_e} \tag{2.24}$$

where the electrons are supposed to be governed by a Boltzmann distribution. For axial direction of the cylindrical chamber, combining eqs. (2.23) and (2.24) with supposing a parallel plane geometry,

$$\mathbf{u_i} = -\mu_i T_e \frac{1}{n_e}\frac{\mathrm{d}n_e}{\mathrm{d}x} \tag{2.25}$$

where the mobility can be given as

$$\mu_{\mathrm{i}} = \frac{2\mathrm{e}\lambda_{\mathrm{i}}}{\pi m_{\mathrm{i}} u_{\mathrm{i}}}. \tag{2.26}$$

Here, the mean free path for ions λ_i is given by

$$\frac{1}{\lambda_{\mathrm{i}}} = \sum_{j,k} \sigma_k n_j. \tag{2.27}$$

Then, substituting eq. (2.26) into eq. (2.25),

$$u_{\mathrm{i}}^2 = -u_{\mathrm{B}}^2 \frac{2}{\pi} \frac{\lambda_{\mathrm{i}}}{n_{\mathrm{e}}} \frac{\mathrm{d}n_{\mathrm{e}}}{\mathrm{d}x}. \tag{2.28}$$

Substituting the square root of eq. (2.28) into the continuous equation (2.22),

$$u_{\mathrm{B}} \left(\frac{2\lambda_{\mathrm{i}}}{\pi} \right)^{1/2} \frac{\mathrm{d}}{\mathrm{d}x} \left(-n \frac{\mathrm{d}n}{\mathrm{d}x} \right)^{1/2} = \nu_{\mathrm{iz}} n \tag{2.29}$$

The heuristic solution of this equation for the boundary condition s that $u_{\mathrm{i}} = 0$ at the plasma center and $u_{\mathrm{i}} = u_{\mathrm{B}}$ was obtained by Godyak as

$$h_{\mathrm{l}} = \frac{0.86}{\sqrt{3 + \frac{L}{2\lambda_{\mathrm{i}}}}}. \tag{2.30}$$

For radial direction of the cylindrical chamber, Godyak also found a heuristic solution

$$h_{\mathrm{r}} = \frac{0.8}{\sqrt{4 + \frac{R}{\lambda_{\mathrm{i}}}}}. \tag{2.31}$$

2.4 EQP analyzer

The plasma monitor as known as electrostatic quadrupole plasma [EQP] analyzer is a combination of an energy analyzer and a mass spectrometer, and is used in this work to measure

the chemical composition of the neutral and ionized species in our plasma discharge. The EQP is mainly used in two modes, Secondary Ion Mass Spectrometer [SIMS] analysis of positive or negative ions or Residual Gas Analyzer [RGA] of neutrals and radicals. Fig. 2.6 shows the electrode configuration of the EQP. The EQP analyzer consists of those parts:

- Ion optics (a)-(f). This part has two functions: 1) focusing ions to the energy analyzer part (E), 2) accelerating or decelerating ions. The ion optics consists of 8 for SIMS and 9 for RGA tunable electrodes.

- Ionization source (B). It is used in RGA mode to ionize neutrals and radicals. The electrons emitted from 1 or 2 filaments are accelerated by electrodes to arbitral energy. In this research the typical value 70 eV is used for EQP calibration. The neutrals and radicals are ionized by the electron-impact.

- 45° electrostatic analyzer (ESA) (E). At the ESA part (E), ions with a specific energy-to-charge ratio, ε, are able to pass through. ε was kept at 40 eV/q, where q is the unit of the ion charge, in this experiment.

- RF quadrupole mass filter (F).

- Secondary electron multiplier (SEM) detector.

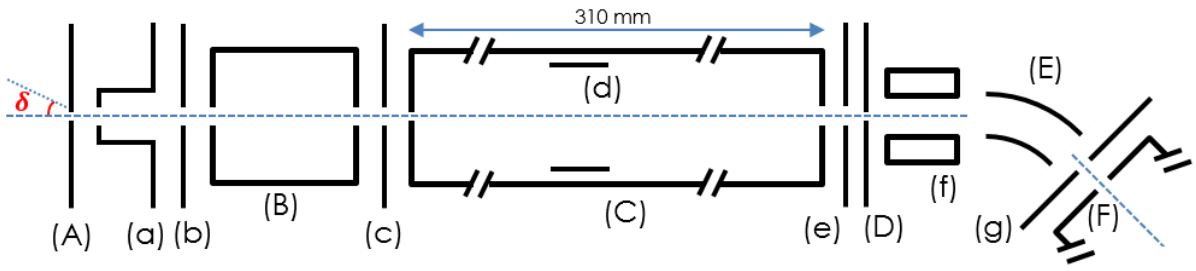

Figure 2.6: The configuration of the EQP: (A) entrance orifice (50 μm), (B) electron impact ionizer, (C) 310 mm length drift tube with 3 mm diameter entrance diaphragm, (D) entrance orifice of ESA, (E) ESA, (F) quadrupole mass spectrometer followed by SEM detector; tunable ion optics lenses (a) extractor, (b) lens 1, (c) source focus, (d) flight focus, (e) lens 2, (f) D.C. quad, vert, horiz lens, and (g) focus 2. δ is the acceptance angle at the entrance orifice.

The use of EQP in plasma experiments has been discussed in several articles [35][18]. Ions and neutrals are sampled by passing through a sampling orifice (A), which has an aperture of 50 μm diameter. When operating in the Residual Gas Analysis [RGA] mode, the neutral gasses are ionized by the electron impact ionizer (B) following the entrance orifice (A). Sampled ions or those formed in the ionizer stage travel to the ion optics. The ion optics act to focus ions to the ESA part, and act to either accelerate/decelerate those ions. The focusing effect is very sensitive to the potential setting of the 8-9 electrodes. Therefore, in this research, all electrodes are set to the same potential, -40 V, to the EQP's reference potential so that the ion optics is defocused. Sampled/formed ions go to the ESA part (E) through the 310 mm length drift tube (C). The ESA part (E) follows a 2 mm diameter entrance orifice (D). In this research, the reference potential of all ion optics electrodes after the ionizer part is scanned to accelerates/decelerates ions of a particular initial kinetic energy to $\varepsilon = 40$ eV/q. The resolution of the ESA is $\Delta E = 1.0$ eV (full width at half maximum [FWHM]) which was determined by measuring neutral Ar gas ionized in (B) (Sec. 3.2.2). After the ESA part, the selected ions enter the RF quadrupole mass filter which passes ions with chosen mass-to-charge ratio. Finally, the selected ions are detected as a pulse by the SEM detector. The pulse signals from the SEM detector are counted by a Plasma Mass Spectrometer Interface Unit [MSIU], which is controlled by a personal computer.

2.4.1 Interpretation model of EQP

An interpretation model of output signals from an EQP analyzer was theoretically given by [29]. The particle current density $\mathrm{d}j$ of ions with a velocity range between v and $v + \mathrm{d}v$ is given by

$$\mathrm{d}j = v\mathrm{d}n = v f_v \mathrm{d}^3 v = \mathbf{v} v^2 f_v \sin\theta \mathrm{d}\theta \mathrm{d}\phi \mathrm{d}v \tag{2.32}$$

in the spherical co-ordinates (fig. 2.7) where the $\theta = 0$ direction is perpendicular to the EQP entrance flat head. The velocity distribution function f_v is the function of the location r and

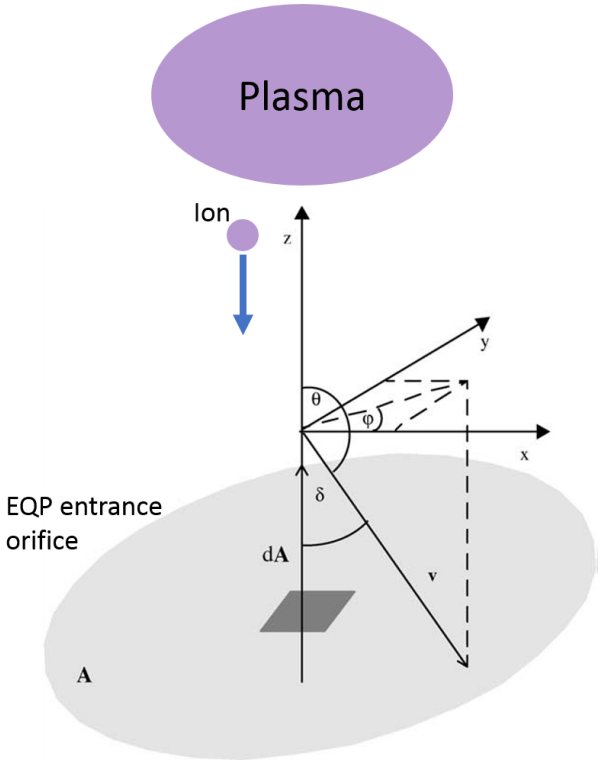

Figure 2.7: Spherical co-ordinates and definition of $\theta = 0$ i.e. the z axis is perpendicular to the EQP entrance flat head. [29]

velocity v so that $f_v(r,v) = f_v(r,v,\theta,\phi)$. The electric current hitting onto the differential surface area dA is represented as

$$\mathrm{d}(\mathrm{d}I) = q\mathrm{d}j\mathrm{d}A \tag{2.33}$$

where q is the ion charge and dA is the normal vector. For the simplicity, those two conditions are assumed: 1) the ion flux to be homogeneous, and 2) the transmission probability to be constant across the area A of the EQP entrance orifice. As a result of these assumptions, the integration regarding to dA can be replaced by the simple multiplication with its magnitude A. Therefore, eq. (2.33) becomes

$$\mathrm{d}I = 2\pi qA\left\{\int_{\theta_{0(v)}}^{\pi} \mathrm{d}\theta\cos\theta\sin\theta v^3 f_v(r,v)\right\}\mathrm{d}v \tag{2.34}$$

where we define $\theta_0 = \pi - \delta$ and δ is the acceptance angle of the EQP. The definition of the acceptance angle σ is as the maximum entrance angle with respect to the ion optical axis at

which an incoming ion is able to enter the ESA [35]. In Chapter 3, the acceptance angle for our configurations is estimated about 0.2°. When the acceptance angle of the ion optics at the entrance orifice is small enough ($\leq 1^\circ$) to assume that the trajectory of incoming ion is parallel to the axis of the ion optics, the distribution function $f_v(r, v, \theta, \phi)$ is replaced by $f_v(r, v, \pi)$ where the particles go into the EQP along the $-z$ direction as shown in fig. 2.7, and the dependency on ϕ is ignored because of homogeneity assumption of ion flux. Eq. (2.34) then becomes

$$\mathrm{d}I = 2\pi qA \left\{ \int_{\theta'_{0(v')}}^{\pi} \mathrm{d}\theta' \cos\theta' \sin\theta' v'^3 f_v(r, v', \pi) \right\} \mathrm{d}v'. \tag{2.35}$$

The characters highlighted by ()' refer to a parameter inside EQP. Performing integration,

$$\mathrm{d}I = -\delta'^2(v)\pi qAv'^3 f_v(\mathbf{r}, v', \pi)\mathrm{d}v' = qA\mathrm{d}j_A \tag{2.36}$$

where $\mathrm{d}j_A$ is the current density of ions entering the EQP entrance orifice with the velocity in a range between v' and $v' + \mathrm{d}v'$. The total ion current entering the EQP system and reaching the detector is then given by the integral

$$I_\mathrm{D} = \int P(\varepsilon, E'_\mathrm{kin})\mathrm{d}I \tag{2.37}$$

where $\mathrm{d}I$ is given above and $P(\varepsilon, E'_\mathrm{kin})$ denotes the transmission function of EQP system which is a function of the passing energy of ESA, ε, and E_kin. E_kin denotes the kinetic energy of detected ions. Then, from eqs. (2.36) and (2.38), the output signal counts for ion species j from an EQP analyzer is represented as,

$$I_{\mathrm{D},j} = -\left(\frac{2\pi qA}{m_j^2}\right) \int \delta'^2(E'_\mathrm{kin}) P(\varepsilon, E'_\mathrm{kin}, m_j) E'_\mathrm{kin} f_v(\mathbf{r}_\mathrm{a}, E'_\mathrm{kin}) \tag{2.38}$$

where m_j is the ion mass appearing due to transformation of variable $m_j v^2/2 = E'_{\text{kin}}$. Because the ion optics are defocused, $\delta'^2(E'_{\text{kin}})$ is assumed as constant. In our work, the passing energy, ε, of ESA was kept constant, 40 eV/q which the manufacture sets as recommended setting. Therefore, the transmission function, P, is dependent only on the kinetic energy and mass of ions. In our experimental setup, ion optics were defocused so that only ions with an initial trajectory lying within the acceptance angle are measured. As discussed in Section 3.2.1, the acceptance angle is estimated as 0.2° from the ion optics geometry. Thus, the acceptance angle is small enough to apply the interpretation model to our EQP's output signal. In the case where the distribution function broadening from the ion or neutral gas temperature is much smaller than the ESA's resolution, the variation of P over the integration in eq. (2.38) can be negligible for both SIMS and RGA measurements. Therefore we can take P out of the integrand and then write,

$$I_{\text{D},j}(\varepsilon, V_{\text{a}}) = j_{\text{A}} A P(\varepsilon, V_{\text{a}}, m_j) \tag{2.39}$$

where j_A is the current density at the orifice and $q = 1$ (singly ionized),

$$j_{\text{A}} = \frac{2\pi}{m_j^2} \int f_v(r_{\text{a}}, E'_{\text{kin}}) \delta'^2 E'_{\text{kin}} \mathrm{d}E'_{\text{kin}}. \tag{2.40}$$

This result then implies that if P is known, we can obtain the distribution function f_v and thus the density of ions from the measured EQP signals.

2.5 Ion density measurements and predictions in N-H plasmas

Results from the global model have been compared with ion densities experimentally measured by the EQP analyzer. Figure 2.8 shows the results from experiments of Carrasco *et al*. [20].

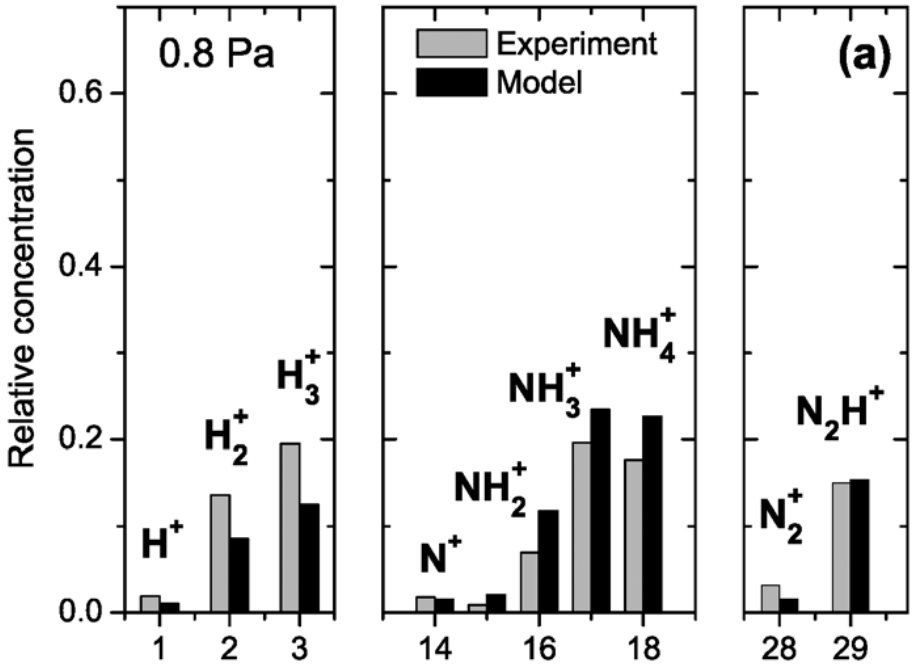

Figure 2.8: w
ith H_2/(10%)N_2 at 15 mTorr [20].]Measured (grey bars) and calculated (black bars) ion concentration for a plasma [$n_e \sim 3.5 \times 10^{16}$ m^{-3}, $T_e \sim 3.4$ eV] with H_2/(10%)N_2 at 15 mTorr [20].

Fig. 2.8(a) shows the measured ion density concentration for a plasma with H_2/(10%)N_2 at 15 mTorr, $n_e \sim 3.5 \times 10^{16}$ m^{-3}, $T_e \sim 3.4$ eV. The important intermediate products of HN-MAR, NH_3^+ and NH_4^+ are shown as dominant ion species. The model well reproduced its concentration especially for NH_4^+. According to the model calculation, the reactions $H_3^+ + NH_3 \rightarrow NH_4^+ + H_2$, $NH_3^+ + NH_3 \rightarrow NH_4^+ + NH_2$, and $N_2H^+ + NH_3 \rightarrow NH_4^+ + N_2$ would contribute to form NH_4^+. Fig. 2.9 also measured density for a plasma at $n_e \sim 10^{16}$ m^{-3}, $T_e \sim 3$ eV with scanning H_2/N_2 gas pressure ratio while the total pressure was kept 11 mTorr. Fig. 2.9(b) shows NH_3^+ and NH_4^+ ions as dominant ion species as well as fig. 2.8 case when $f_{N_2} > 5\%$. At nitrogen pressure fruction $f_{N_2} = p_{N_2}/p_{tot} \sim 10\%$, the rate equation model calculation suggested the main formation of NH_4^+ is $H_3^+ + NH_3 \rightarrow NH_4^+ + H_2$. Those reactions play an important role in the new recombination process discussed in this thesis. In those experiments, the electron-ion recombination process was ignored because the recombination on the wall surface dominates its loss process because

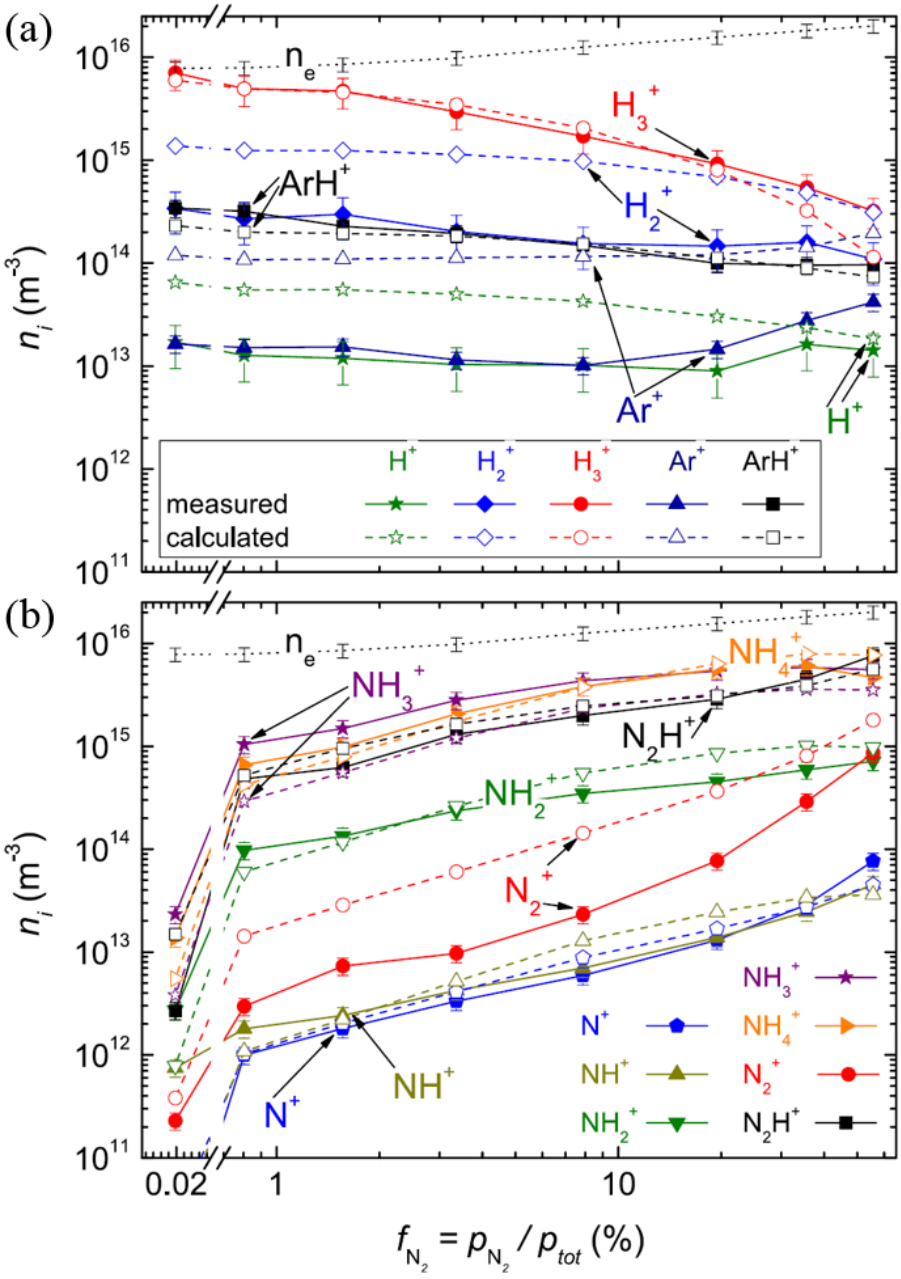

Figure 2.9: Measured (solid lines) and calculated (dashed lines) ion density for a plasma [$n_e \sim 10^{16}$ m^{-3}, $T_e \sim 3$ eV] at 11 mTorr.

of low electron density. This experiment expand the electron range up to 10^{18} m^{-3} in which the volumetric recombination process plays an important role.

Table 2.1: Rate coefficients for electron collision besides recombination reactions

k	Reaction	Rate coefficient [m^3s^{-1}]	Reference
1.1	$e^- + H_2 \rightarrow 2H + e^-$	$8.4 \times 10^{-14} T_e^{-0.45} \times e^{-11.18/T_e}$	Yoon [112]
1.2	$e^- + H \rightarrow H^+ + 2e^-$	$1.1 \times 10^{-14} T_e^{0.29} \times e^{-15.28/T_e}$	Shah [93]
1.3	$e^- + H_2 \rightarrow H_2^+ + 2e^-$	$2.3 \times 10^{-14} T_e^{0.19} \times e^{-17.87/T_e}$	Yoon [112]
1.4	$e^- + H_2 \rightarrow H^+ + H + 2e^-$	$9.4 \times 10^{-16} T_e^{0.45} \times e^{-29.94/T_e}$	Yoon [112]
1.5	$e^- + Ar \rightarrow Ar^+ + 2e^-$	$3.7 \times 10^{-14} T_e^{0.38} \times e^{-17.64/T_e}$	Wetzel [111]
1.6	$e^- + N_2 \rightarrow N + N(D) + e^-$	$2.4 \times 10^{-14} T_e^{0.27} \times e^{-15.53/T_e}$	Itikawa [43]
1.7	$e^- + N \rightarrow N_2^+ + 2e^-$	$9.3 \times 10^{-15} T_e^{0.56} \times e^{-16.66/T_e}$	Kim [51]
1.8	$e^- + N_2 \rightarrow N_2^+ + 2e^-$	$1.3 \times 10^{-14} T_e^{0.56} \times e^{-17.07/T_e}$	Itikawa [43]
1.9	$e^- + N_2 \rightarrow N^+ + N + 2e^-$	$2.9 \times 10^{-15} T_e^{0.72} \times e^{-29.71/T_e}$	Itikawa [43]
1.10	$e^- + NH_3 \rightarrow NH_3^+ + 2e^-$	$1.5 \times 10^{-14} T_e^{0.40} \times e^{-13.61/T_e}$	Tarnovsky [103]
1.11	$e^- + NH_3 \rightarrow NH_2^+ + H + 2e^-$	$1.6 \times 10^{-14} T_e^{0.34} \times e^{-15.41/T_e}$	Tarnovsky [103]
1.12	$e^- + NH_3 \rightarrow NH^+ + 2H + 2e^-$	$5.4 \times 10^{-16} T_e^{0.37} \times e^{-26.06/T_e}$	Tarnovsky [103]
1.13	$e^- + NH_3 \rightarrow N^+ + H + H_2 + 2e^-$	$8.8 \times 10^{-17} T_e^{0.59} \times e^{-29.00/T_e}$	Märk [65]
1.14	$e^- + NH_3 \rightarrow H^+ + H + NH_2 + 2e^-$	$1.3 \times 10^{-16} T_e^{0.47} \times e^{-28.55/T_e}$	Märk [65]
1.15	$e^- + NH_2 \rightarrow NH_2^+ + 2e^-$	$1.3 \times 10^{-14} T_e^{0.50} \times e^{-12.40/T_e}$	Tarnovsky [103]
1.16	$e^- + NH_2 \rightarrow NH^+ + H + 2e^-$	$2.2 \times 10^{-14} T_e^{0.21} \times e^{-17.97/T_e}$	Tarnovsky [103]
1.17	$e^- + NH \rightarrow NH^+ + 2e^-$	$2.1 \times 10^{-14} T_e^{0.37} \times e^{-15.49/T_e}$	Tarnovsky [103]
1.18	$e^- + NH \rightarrow N^+ + H + 2e^-$	$7.6 \times 10^{-15} T_e^{0.29} \times e^{-16.82/T_e}$	Tarnovsky [103]
1.19	$e^- + NH_3 \rightarrow NH_2 + H + e^-$	$4.2 \times 10^{-14} T_e^{-0.19} \times e^{-7.59/T_e}$	Yousfi [113]
1.20	$e^- + NH_3 \rightarrow NH + 2H + e^-$	$1.3 \times 10^{-14} T_e^{0.38} \times e^{-11.06/T_e}$	Yousfi [113]
1.21	$e^- + NH_3 \rightarrow NH + H_2 + e^-$	$4.1 \times 10^{-14} T_e^{-0.26} \times e^{-4.84/T_e}$	Yousfi [113]
1.22	$e^- + NH_2 \rightarrow NH + H + e^-$	$4.5 \times 10^{-14} T_e^{-0.22} \times e^{-7.61/T_e}$	Laer [61]
1.23	$e^- + NH_2 \rightarrow N + H_2 + e^-$	$1.5 \times 10^{-14} T_e^{0.38} \times e^{-11.44/T_e}$	Laer [61]
1.24	$e^- + NH \rightarrow N + H + e^-$	$4.7 \times 10^{-14} T_e^{-0.22} \times e^{-7.69/T_e}$	Laer [61]
1.25	$e^- + H_2^+ \rightarrow H^+ + H + e^-$	$1.5 \times 10^{-13} \times e^{-1.97/T_e}$	Kimura [53]

Table 2.2: Rate coefficients for ion-molecule reactions.

k	Reaction	Rate coefficient [m^3s^{-1}]	Reference
2.1	$H_2^+ + H_2 \rightarrow H_3^+ + H$	2.0×10^{-15}	Anicich [6][7]
2.2	$ArH^+ + H_2 \rightarrow H_3^+ + Ar$	6.3×10^{-16}	Anicich [6][7]
2.3	$H_2^+ + Ar \rightarrow ArH^+ + H$	2.1×10^{-15}	Anicich [6][7]
2.4	$H_2^+ + Ar \rightarrow Ar^+ + H_2$	2.0×10^{-16}	Anicich [6][7]
2.5	$H_3^+ + Ar \rightarrow ArH^+ + H_2$	3.7×10^{-16}	Anicich [6][7]
2.6	$Ar^+ + H_2 \rightarrow ArH^+ + H$	8.7×10^{-16}	Anicich [6][7]
2.7	$Ar^+ + H_2 \rightarrow H_2^+ + Ar$	1.8×10^{-17}	Anicich [6][7]
2.8	$N^+ + N_2 \rightarrow N_2^+ + N$	2.0×10^{-17}	Tao [102]
2.9	$N_2^+ + N \rightarrow N^+ + N_2$	1.0×10^{-17}	Anicich [6][7]
2.10	$Ar^+ + N_2 \rightarrow N_2^+ + Ar$	1.1×10^{-17}	Anicich [6][7]
2.11	$N_2^+ + Ar \rightarrow Ar^+ + N_2$	2.0×10^{-19}	Anicich [6][7]
2.12	$N_2^+ + D_2 \rightarrow N_2D^+ + D$	2.2×10^{-15}	Anicich [6][7]
2.13	$D_2^+ + N_2 \rightarrow N_2D^+ + D$	1.6×10^{-15}	Anicich [6][7]
2.14	$D_3^+ + N_2 \rightarrow N_2D^+ + D_2$	1.1×10^{-15}	Anicich [6][7]
2.15	$H_3^+ + NH_3 \rightarrow NH_4^+ + H_2$	4.4×10^{-15}	Anicich [6][7]
2.16	$N^+ + D_2 \rightarrow ND^+ + D$	1.5×10^{-16}	Anicich [6][7]
2.17	$NH_2^+ + H_2 \rightarrow NH_3^+ + H$	2.0×10^{-16}	Anicich [6][7]
2.18	$H_2^+ + N \rightarrow N^+ + H_2$	5.0×10^{-16}	Arakoni [8]
2.19	$Ar^+ + NH_2 \rightarrow NH^+ + H + Ar$	5.5×10^{-17}	Arakoni [8]
2.20	$D^+ + ND_3 \rightarrow ND_3^+ + D$	3.1×10^{-15}	Anicich [6][7]
2.21	$H_2^+ + NH_3 \rightarrow NH_3^+ + H_2$	5.7×10^{-15}	Anicich [6][7]
2.22	$H_3^+ + N \rightarrow NH^+ + H_2$	2.6×10^{-16}	Anicich [6][7]
2.23	$H_3^+ + N \rightarrow NH_2^+ + H$	3.9×10^{-16}	Anicich [6][7]
2.24	$N^+ + NH_3 \rightarrow NH_2^+ + NH$	4.7×10^{-16}	Anicich [6][7]
2.25	$N^+ + NH_3 \rightarrow NH_3^+ + N$	1.7×10^{-15}	Anicich [6][7]
2.26	$N^+ + NH_3 \rightarrow N_2H^+ + H_2$	2.1×10^{-16}	Anicich [6][7]
2.27	$NH^+ + H_2 \rightarrow H_3^+ + N$	1.8×10^{-16}	Anicich [6][7]
2.28	$NH^+ + H_2 \rightarrow NH_2^+ + H$	1.0×10^{-15}	Anicich [6][7]
2.29	$NH^+ + NH_3 \rightarrow NH_3^+ + NH$	1.8×10^{-15}	Anicich [6][7]
2.30	$NH^+ + NH_3 \rightarrow NH_4^+ + N$	6.0×10^{-16}	Anicich [6][7]

Table 2.3: Rate coefficients for ion-molecule reactions.

k	Reaction	Rate coefficient [m^3s^{-1}]	Reference
2.31	$NH^+ + N_2 \rightarrow N_2H^+ + N$	6.5×10^{-16}	Anicich [6][7]
2.32	$NH_2^+ + NH_3 \rightarrow NH_3^+ + NH_2$	1.2×10^{-15}	Anicich [6][7]
2.33	$NH_2^+ + NH_3 \rightarrow NH_4^+ + NH$	1.2×10^{-15}	Anicich [6][7]
2.34	$ND_3^+ + D_2 \rightarrow ND_4^+ + ND_2$	1.0×10^{-19}	Anicich [6][7]
2.35	$ND_3^+ + ND_3 \rightarrow ND_4^+ + ND_2$	1.7×10^{-15}	Anicich [6][7]
2.36	$N_2^+ + NH_3 \rightarrow NH_3^+ + N_2$	2.0×10^{-15}	Anicich [6][7]
2.37	$N_2H^+ + H_2 \rightarrow H_3^+ + N_2$	5.1×10^{-24}	Anicich [6][7]
2.38	$N_2H^+ + NH_3 \rightarrow NH_4^+ + N_2$	2.3×10^{-15}	Anicich [6][7]
2.39	$Ar^+ + NH_3 \rightarrow NH_3^+ + Ar$	1.6×10^{-15}	Anicich [6][7]
2.40	$ArH^+ + NH_3 \rightarrow NH_3^+ + H + Ar$	5.3×10^{-16}	Anicich [6][7]
2.41	$ArH^+ + NH_3 \rightarrow NH_4^+ + Ar$	1.6×10^{-15}	Anicich [6][7]
2.42	$ArH^+ + N_2 \rightarrow N_2H^+ + Ar$	8.0×10^{-16}	Anicich [6][7]
2.43	$N^+ + H \rightarrow H^+ + N$	2.0×10^{-15}	Arakoni [8]
2.44	$H_2^+ + NH_3 \rightarrow NH_4^+ + H$	5.0×10^{-17}	Arakoni [8]
2.45	$H_2^+ + NH_2 \rightarrow NH_3^+ + H$	5.0×10^{-17}	Arakoni [8]
2.46	$H_2^+ + NH \rightarrow NH_2^+ + H$	5.0×10^{-17}	Arakoni [8]
2.47	$NH^+ + NH_2 \rightarrow NH_2^+ + NH$	1.8×10^{-15}	Arakoni [8]
2.48	$Ar^+ + NH_3 \rightarrow NH_2^+ + H + Ar$	5.5×10^{-17}	Arakoni [8]
2.49	$Ar^+ + NH_3 \rightarrow ArH^+ + NH_2$	9.2×10^{-17}	Arakoni [8]
2.50	$H_2^+ + H \rightarrow H_2 + H^+$	$10^{-16} \times (8.7 - 1.3T_e + 1.0 \times 10^{-1}T_e^2 - 3.3 \times 10^{-3}T_e^3)$	Pigarov [84]
2.51	$H^+ + H_2 \rightarrow H_2^+ + H$	$-4.3 \times 10^{-17} + 4.9 \times 10^{-17}T_e - 1.8 \times 10^{-19}T_e^2$	Pigarov [84]

Table 2.4: Rate coefficients for electron collision and molecule-excited species reactions.

k	Reaction	Rate coefficient [s^{-1}]	Reference
3.1	$e^- + Ar \rightarrow Ar(m) + e^-$	$5.0 \times 10^{-15} \times e^{-12.64/T_e}$	Kimura [53]
3.2	$e^- + Ar \rightarrow Ar(4p) + e^-$	$2.1 \times 10^{-14} \times e^{-13.13/T_e}$	Kimura [53]
4.1	$e^- + N_2 \rightarrow N_2(A) + e^-$	$1.2 \times 10^{-14} \times e^{-7.34/T_e}$	Kimura [52]
4.2	$e^- + N_2 \rightarrow N_2(B) + e^-$	$5.6 \times 10^{-15} \times e^{-6.81/T_e}$	Kimura [52]
4.3	$e^- + N_2 \rightarrow N_2(C) + e^-$	$6.4 \times 10^{-15} \times e^{-9.87/T_e}$	Kimura [52]
4.4	$e^- + N_2 \rightarrow N_2(a) + e^-$	$5.1 \times 10^{-15} \times e^{-11.69/T_e}$	Kimura [52]
4.5	$e^- + N_2(A) \rightarrow N_2^+ + 2e^-$	$8.3 \times 10^{-15} \times e^{-12.84/T_e}$	Kimura [52]
4.6	$e^- + N_2(B) \rightarrow N_2^+ + 2e^-$	$2.1 \times 10^{-14} \times e^{-11.0/T_e}$	Kimura [52]
4.7	$e^- + N_2(a) \rightarrow N_2^+ + 2e^-$	$4.3 \times 10^{-14} \times e^{-10.32/T_e}$	Kimura [52]
4.8	$e^- + N \rightarrow N(D) + e^-$	$2.7 \times 10^{-14} T_e^{-0.4} \times e^{-3.35/T_e}$	Kimura [52]
4.9	$e^- + N \rightarrow N(P) + e^-$	$9.1 \times 10^{-14} T_e^{-0.45} \times e^{-4.80/T_e}$	Kimura [52]
4.10	$e^- + N(D) \rightarrow N^+ + 2e^-$	$1.7 \times 10^{-14} T_e^{-0.5} \times e^{-13.07/T_e}$	Kimura [52]
4.11	$e^- + N(P) \rightarrow N^+ + 2e^-$	$9.4 \times 10^{-15} T_e^{-0.67} \times e^{-11.25/T_e}$	Kimura [52]
4.12	$N_2(a) + N_2(A) \rightarrow N_2^+ + e^-$	9.0×10^{-18}	Kimura [52]
4.13	$2N_2(a) \rightarrow N_2^+ + e^-$	2.5×10^{-17}	Kimura [52]
4.14	$N_2(A) + N \rightarrow N(P) + N_2^+$	5.0×10^{-16}	Kimura [52]
4.15	$N_2(A) + N_2 \rightarrow 2N_2$	4.0×10^{-17}	Kimura [52]
4.16	$N(P) + N(D) \rightarrow N_2^+ + e^-$	3.0×10^{-18}	Kimura [52]
5.1	$Ar(m) + H_2 \rightarrow 2H + Ar$	1.1×10^{-16}	Kimura [53]
5.2	$Ar(r) + H_2 \rightarrow 2H + Ar$	1.1×10^{-16}	Kimura [53]
5.3	$Ar(m) + N_2 \rightarrow N_2(C) + Ar$	3.0×10^{-17}	Kimura [52]
5.4	$N_2(A) + H \rightarrow N_2 + H$	5.0×10^{-17}	Tatarova [104]
5.5	$N_2(A) + H_2 \rightarrow N_2 + 2H$	2.0×10^{-16}	Tatarova [104]
5.6	$N_2(A) + NH_3 \rightarrow N_2 + NH_3$	1.6×10^{-16}	Tatarova [104]
5.7	$N_2(B) + H_2 \rightarrow N_2(A) + H_2$	2.5×10^{-17}	Tatarova [104]
5.8	$N_2(a) + H \rightarrow N_2(A) + H_2$	1.5×10^{-17}	Tatarova [104]
5.9	$N_2(a) + H_2 \rightarrow N_2 + 2H$	2.6×10^{-17}	Tatarova [104]
5.10	$N(D) + H_2 \rightarrow NH + H$	2.3×10^{-18}	Tatarova [104]
5.11	$N(D) + NH_3 \rightarrow NH_2 + NH$	1.1×10^{-16}	Tatarova [104]
5.12	$N(P) + H_2 \rightarrow NH + H$	2.5×10^{-20}	Tatarova [104]

Table 2.5: Rate coefficients for radiative process.

k	Reaction	Rate coefficient [s^{-1}]	Reference
3.3	Ar(r) $\rightarrow$ Ar + $h\nu$	1.0×10^5	Kimura [53]
3.4	Ar($4p$) $\rightarrow$ Ar(r) + $h\nu$	3.0×10^7	Kimura [53]
3.5	Ar($4p$) $\rightarrow$ Ar(m) + $h\nu$	3.0×10^7	Kimura [53]
4.17	$N_2(B) \rightarrow N_2(A) + h\nu$	2.0×10^5	Kimura [52]
4.18	$N_2(C) \rightarrow N_2(B) + h\nu$	2.7×10^7	Kimura [52]

Table 2.6: Rate coefficients for wall loss process.

k	Reaction	Rate coefficient [m^3s^{-1}]	Reference
3.6	Ar(m) + wall $\rightarrow$ Ar	$K_{\mathrm{wAr(m)}}(\beta_{\mathrm{Ar(m)}} = 1)$	Hjartarson [38]
4.19	$N_2(A)$ + wall $\rightarrow N_2$	$K_{\mathrm{wN_2(A)}}(\beta_{\mathrm{N_2(A)}} = 1)$	Thorsteinsson [106]
4.20	$N_2(a)$ + wall $\rightarrow N_2$	$K_{\mathrm{wN_2(a)}}(\beta_{\mathrm{N_2(a)}} = 1)$	Kimura [52]
4.21	N(D) + wall $\rightarrow 0.5N_2$	$K_{\mathrm{wN(D)}}(\beta_{\mathrm{N(D)}} = 0.99)$	
4.22	N(P) + wall $\rightarrow 0.5N_2$	$K_{\mathrm{wN(P)}}(\beta_{\mathrm{N(P)}} = 0.99)$	
4.23	N(D) + wall $\rightarrow$ N	$K_{\mathrm{wN(D)}}(\beta_{\mathrm{N(D)}} = 0.01)$	
4.24	N(P) + wall $\rightarrow$ N	$K_{\mathrm{wN(P)}}(\beta_{\mathrm{N(P)}} = 0.01)$	

Table 2.7: Rate coefficients for electron ion recombination reactions.

k	Reaction	Rate coefficient [m^3s^{-1}]	Reference
6.1	$e^- + H_2^+ \rightarrow 2H$	$10^{-16} \times (7.5 \times 10 - 1.1 \times 10T_e$ $+1.0T_e^2 - 4.2 \times 10^{-2}T_e^3$ $+5.9 \times 10^{-4}T_e^4)$	Méndez [70]
6.2	$e^- + H_3^+ \rightarrow 3H$	$10^{16} \times (4.2 \times 10 + 1.5 \times 10T_e$	”
6.3	$e^- + H_3^+ \rightarrow H_2 + H$	$-1.9T_e^2 + 6.5 \times 10^{-2}T_e^3$ $+1.2 \times 10^{-3}T_e^4 - 1.2 \times 10^{-4}T_e^5$ $+1.8 \times 10^{-6}T_e^6)$	
6.4	$e^- + N_2^+ \rightarrow 2N$	$2.8 \times 10^{-13} \times (0.026/T_e)^{0.5}$	Kossyi [54]
6.5	$e^- + NH^+ \rightarrow N + H$	$4.3 \times 10^{-14} \times (0.026/T_e)^{0.5}$	Mitchell [72]
6.6	$e^- + NH_2^+ \rightarrow NH + H$	$1.0 \times 10^{-13} \times (0.026/T_e)^{0.4}$	Vikor [109]
6.7	$e^- + NH_2^+ \rightarrow N + 2H$	$2.0 \times 10^{-13} \times (0.026/T_e)^{0.4}$	Vikor [109]
6.8	$e^- + NH_3^+ \rightarrow NH + 2H$	$1.6 \times 10^{-13} \times (0.026/T_e)^{0.5}$	Mitchell [72]
6.9	$e^- + NH_3^+ \rightarrow NH_2 + H$	$1.6 \times 10^{-13} \times (0.026/T_e)^{0.5}$	Mitchell [72]
6.10	$e^- + NH_4^+ \rightarrow NH_3 + H$	$8.01 \times 10^{-13} \times (0.026/T_e)^{0.605}$	Vikor [109]
6.11	$e^- + NH_4^+ \rightarrow NH_2 + 2H$	$1.23 \times 10^{-13} \times (0.026/T_e)^{0.605}$	Vikor [109]
6.12	$e^- + N_2H^+ \rightarrow N_2 + H$	$7.1 \times 10^{-13} \times (0.026/T_e)^{0.72}$	Amano [5]
6.13	$e^- + Ar^+ \rightarrow Ar$	$10^{-16} \times (-1.3 + 2.5T_e - 1.0T_e^2$ $+2.2 \times 10^{-1}T_e^3 - 2.6 \times 10^{-2}T_e^4$ $+1.6 \times 10^{-3}T_e^5 - 3.8 \times 10^{-5}T_e^6)$	Kato [49]
6.14	$e^- + ArH^+ \rightarrow Ar + H$	$10^{-16} \times (-1.5 + 1.3 \times 10T_e$ $-1.6 \times 10T_e^2 + 8.4T_e^3 - 1.9T_e^4$ $+2.0 \times 10^{-1}T_e^5 - 8.2 \times 10^{-3}T_e^6)$	Mitchell [71]
6.15	$e^- + N_2H^+ \rightarrow NH + N$	$8.9 \times 10^{-15} \times (1/T_e)^{0.5}$	”

Chapter 3

Experimental methods and data analysis

3.1 PISCES-E RF plasma device

Fig. 3.1 shows schematic drawing of the plasma device, denoted here as PISCES-E, that is used in this work [108][107]. The device has a cylindrical anodized aluminum reaction chamber, with a 350 mm diameter and, depending on the chamber in use, with a height of either 300 mm or 400 mm. Because the volume-to-surface ratio, V/A, of this chamber is about 10-50 times larger than used in previous research [20][97], if the plasma density was high enough, we could operate in a regime dominated by volumetric reactions. The plasma source is located on top of the reaction chamber. An inductively coupled plasma is created in a 100 mm diameter Pyrex bell-jar surrounded by a double loop $m = 0$ antenna driven at 13.56 MHz by a radio frequency power supply unit connected to the antenna via a matching network. The input power is varied from 500 W to 3300 W in this experiment while the reflected power is less than 1% of input power.

The experimental configurations are slightly different for 3 ranges of plasma densities such as [A] $n_e \sim 10^{16}$ m^{-3}, [B] $n_e \sim 4 \times 10^{15} - 3 \times 10^{17}$ m^{-3}, and [C] $n_e \sim 1 \times 10^{17} - 2 \times 10^{18}$ m^{-3}. Table 3.1 lists the operational settings and device specifications of each of these three configurations. The double loop antennas have diameter of 110 mm and are axially spaced

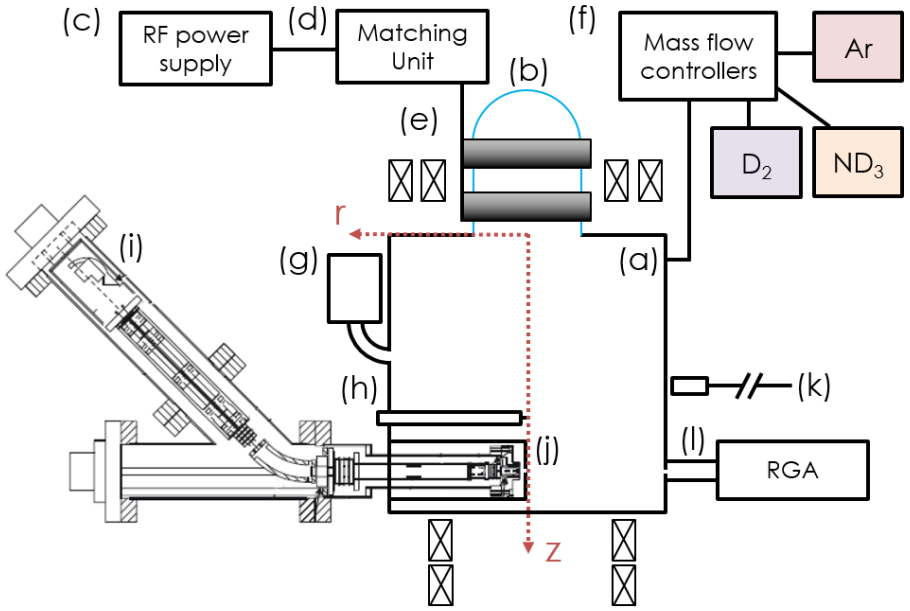

Figure 3.1: Schematic drawing of the Etcher plasma machine consisting of parts: (a) reaction chamber, (b) bell jar surrounded by double loop antennas, (c) RF power supply, (d) matching unit, (e) magnetic coils (f) mass flow controllers connected to D_2 and N_2 gas cylinders, (g) Baratron gauge, (h) Langmuir probe, (i) EQP analyzer, (j) water cooled heat shield, (k) collimation lens with optical fiber transporting lights to the 1.3 m spectrometer and the low dispersion spectrometer, and (l) residual gas analyzer.

Table 3.1: Experimental configurations for 3 ranges of electron densities: [A] $n_e \sim 10^{16}$ m^{-3}, [B] $n_e \sim 4\times10^{15} - 3\times10^{17}$ m^{-3}, and [C] $n_e \sim 1\times10^{17} - 2\times10^{18}$ m^{-3}. $z = 0$ mm at the source exit.

	n_e [m^{-3}]	Discharge power	Gas species	Chamber height	Source coil
A	$\sim 10^{16}$	500 W	D_2, N_2	400 mm	50 A [Out]
B	4×10^{15} -3×10^{17}	500-3300 W	D_2, ND_3, Ar	400 mm	50 A [In/Out]
C	1×10^{17} -2×10^{18}	500-3300 W	D_2, N_2, Ar	300 mm	20 A [In/Out]

	Target coil	B-field at EQP	EQP entrance	Probe tip	Collimator
A	none	~ 2 G	$z = 350$ mm	$z = 300$	$z = 190$
B	120 A	~ 30 G	$z = 350$ mm	$z = 130$	$z = 170$
C	120 A	~ 40 G	$z = 250$ mm	$z = 78$	$z = 58$

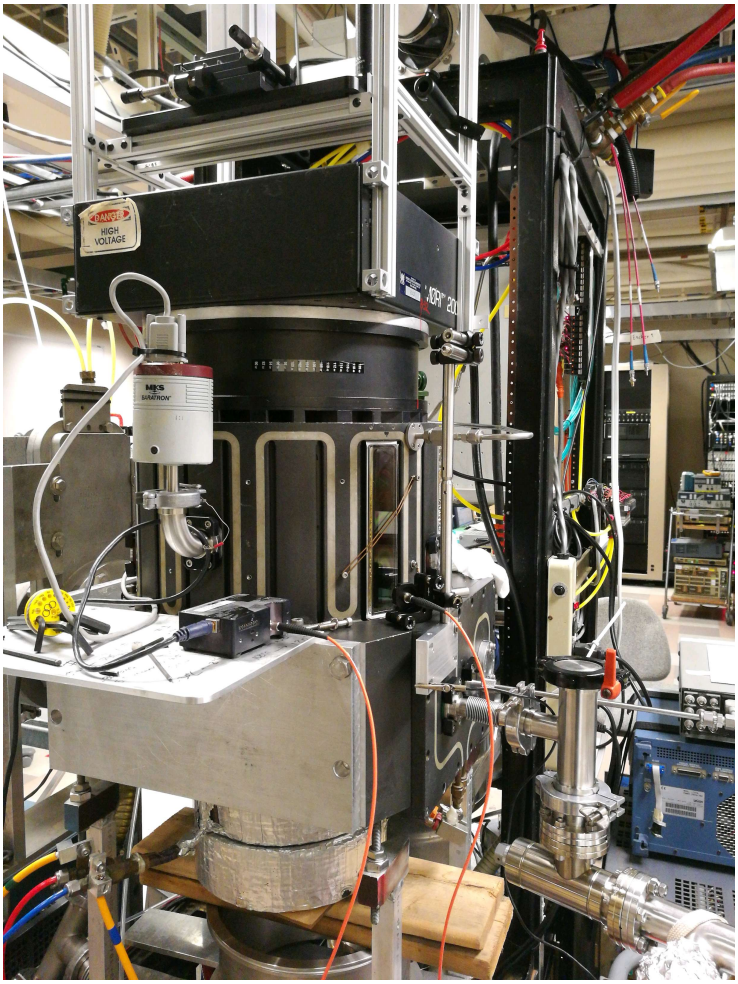

Figure 3.2: A photo of the PISCES-E RF plasma device.

150 mm apart. The RF currents in the two antennas are 180° out of phase. A matching unit (RFPP AM-30 PMT/AMNPS-2A) couples the RF power to the antenna. The two magnetic coils surround the double loop antennas. The 215 mm diameter (inner) coil has 40 turns, while the 315 mm diameter (outer) coil has 20 turns. Both magnets are connected in series. Two other magnet coils are located on the bottom of the chamber. Both coils are also connected in series, and make a magnetic field in the same direction with the source coils. When only the outer coil at the source part is used (configuration [A]), current of 50 A through the outer coil creates a magnetic field of 10 gauss at the center of the belljar. In this case, the magnetic field decays rapidly along the axial direction so that magnetic field in the reaction chamber is supposed to be negligible

so that the plasma in the reaction chamber is considered as un-magnetized [114]. The magnetic fields at the EQP entrance orifice for other cases are listed in table 3.1 with configurations of other diagnostics devices. A Langmuir probe with cylindrical tip, 0.6 mm diameter and 2.2 mm length, is used to measure the electron temperatures and densities. The probe tip is located at the chamber center and different axial positions for each configuration. The rotational temperatures of N_2 and D_2 molecules are determined by measuring spectral line intensities with a 1.33 m Czerny-Turner monochromator (McPHERSON, Model 209) equipped with an intensified CCD camera (Princeton Instruments PI-MAX). The monochromator has a 2400 grooves$/$mm grating giving a resolution of 0.055 nm (FWHM) at $\lambda = 365$ nm. The density of D atom is determined by measuring emission line from D and Ar atoms with a low dispersion spectrometer (Ocean Optics, USB4000). Those spectrometers are calibrated with an integration sphere (Gooch & Housego, Model 455-12-1). A collimation lens collects light from the line-of-sight across the plasma column radially through a quartz viewing window and transmits it via an optical fiber to the spectrometer. The neutral gas pressures are measured by a Baratron gauge installed on the reaction chamber. An Electrostatic Quadrupole Plasma [EQP] analyzer (HIDEN Analytical Inc.) is used to take direct measurements of the ion densities. The inside of the EQP system is differentially pumped so that the pressure within the measurement is kept under 4×10^{-8} Torr. The probe head of the EQP is inserted in the chamber along the radial direction. A water cooled cylindrical heat shield (stainless steal) covers the probe head to prevent over heating of EQP due to the heat flux from the plasmas. The heat shield has an orifice, 1.5 mm or 3.0 mm diameter, on the flat side facing the center of the chamber. The shield also provides magnetic-field free region within the instrument. The entrance orifice of the EQP analyzer is located 7 mm behind from the heat shields orifice part. A differentially pumped Residual Gas Analyzer (RGA), i.g. quadrupole mass spectrometer, is used to determined partial gas pressures. The RGA is connected to the chamber via a right angle valve (Vacuum Generators Ltd, Model CR38). The particle density in RGA is proportional to the pressure in the chamber. Therefore, the RGA is calibrated with the

pressure of each neutral gas species in the chamber measured by the Baratron gauge.

3.2 EQP Analyzer

3.2.1 Acceptance angle

The definition of the acceptance angle δ of the EQP is as the maximum entrance angle with respect to the ion optical axis at which an incoming ion is able to enter the ESA [35]. Hamers *et al.* [35], O'Connell *et al.* [78] and others reported that the acceptance angle varies as a function of the incoming ion energy because of the chromatic aberration effects which is the change of focal length of the ion optics with ion energy. However, in this experiment, the ion optics is defocused by setting all electrodes the same potential, -40 V. Therefore, the acceptance angle can be estimated by the possible trajectories for each ion species, which only depends on geometry inside of the EQP (fig. 2.6). The diameters of the entrance orifice and the diaphragm of the ESA entrance are 50 μm and 2 mm, respectively, separated by 310 mm which is the length of the drift tube. For this geometry, the estimated acceptance angle is then 0.2°.

3.2.2 Resolution of ESA

The resolution of the ESA was determined by measuring neutral Ar gas which was then ionized within the EQP instrument at position (B) in fig. 2.6 and transmitted to (C) while the reference potential of the electrodes, was scanned so as to vary the energy of the detected ions. During this procedure, the gas was held at room temperature, 0.03 eV. Its energy broadening was small enough to be negligible comparing to the typical energy resolution of the ESA. Therefore, the width of obtained energy scan profile then corresponds to the energy resolution of ESA (fig. 3.3). The measurement shows the ESA resolution in our configuration is $\Delta E = 1.0$ eV (full width at half maximum [FWHM]). Knowing this value is important to apply the interpretation

model in Section 2.4.1.

3.2.3 Calibration of EQP

The measured neutral gas temperatures in our plasmas are less than 0.1 eV (see Chapter 5). It has been reported that the calculated ion temperatures at the PISCES-E chamber center are less than 0.1 eV for Ar-N_2 plasma [94]. Those neutral and ion temperatures are much less than 1.0 eV, which is the FWHM of our EQP's transmission factor P. Therefore, eq. (2.40) can be applied to our case. When the ions follow the Maxwell-Boltzmann distribution, eq. (2.40) becomes

$$j_A = n_j \langle v_j \rangle / 4 \tag{3.1}$$

where

$$\langle v_j \rangle = \sqrt{8 k_B T_j / \pi m_j}. \tag{3.2}$$

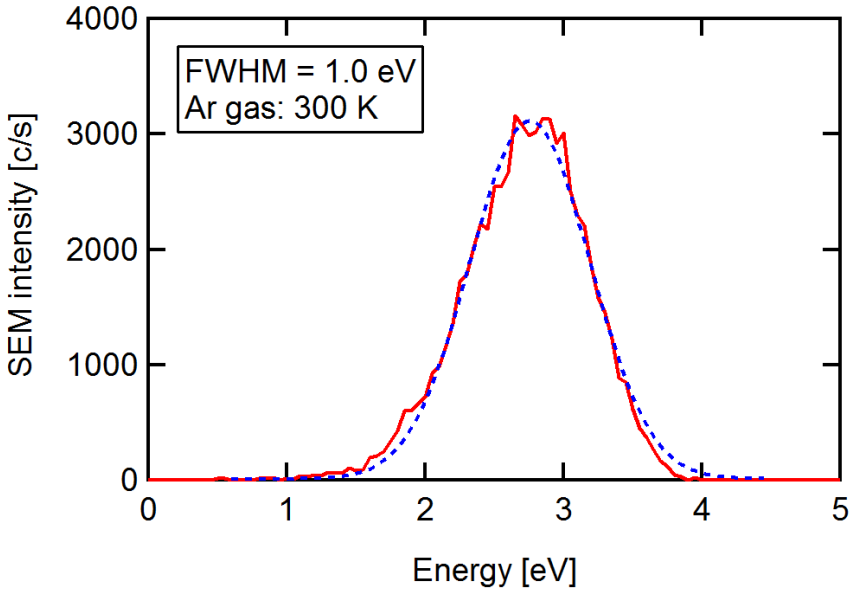

Figure 3.3: The energy scan profile of Ar gas in room temperature (300 K) by RGA mode with defocused ion optics. [1]

By assuming thermal equilibrium between ion species, the transmission factor P is derived from eq. (2.39) as

$$P_{m_j}(V_\mathrm{a}) = \frac{I_{\mathrm{D},j}(E'_\mathrm{kin})}{j_\mathrm{A}A} = \frac{\sqrt{2\pi m_j} I_{\mathrm{D},j}(qV_\mathrm{a})}{n_j\sqrt{k_\mathrm{B}T_j}A}. \tag{3.3}$$

P_{m_j} can therefore be determined experimentally by measuring I_D for each gas species mass m_j by using the relation $n_j = \sigma_{j,70\ \mathrm{eV}} N_j$ where $\sigma_{j,70\ \mathrm{eV}}$ is the cross sections of the electron impact ionization with electron energy of 70 eV for species j [101][111], and N_j is the neutral gas density. Fig. 3.4 shows the measured transmission factors P_{m_j} for different SEM multiplier setting normalized by $P_{40(\mathrm{Ar})}$. During experiments, the electron energy of the electron impact ionizer was kept constant as 70 eV, and the chamber was filled with Ar gas. The partial pressures were monitored by RGA. For multiplier = 1900 V case (fig. 3.4(a)), the measured value of P does not show strong dependence on species (ion mass). On the other hand, fig. 3.4(b) for multiplier = 2500 V case shows a profile as a function of the ion mass. As a result, in the following work those determined P is used for each experimental configuration ([A][B] multiplier = 1900 V, [C] 2500 V).

3.2.4 Conversion of EQP signals to density fractions

When the measured ion species has Maxwell-Bolzman distribution having the peak at potential V_a, the ion density can be obtained from the EQP signal $I_{\mathrm{D},j}$ by using equation 3.3,

$$n_j = \frac{\sqrt{2\pi}}{\sqrt{k_\mathrm{B}T_j}A}\sqrt{m_j} I_{\mathrm{D},j}(qV_\mathrm{a}). \tag{3.4}$$

When the thermal equilibrium between ion species is assumed, the former fraction part of the right hand side of the equation does not depend on ion species. Therefore, the ion density fraction can be obtained as

$$f_j = \frac{n_j}{\sum_i n_i} = \frac{\sqrt{m_j} I_{\mathrm{D},j}(V_\mathrm{a})}{\sum_i \sqrt{m_i} I_{\mathrm{D},i}(V_\mathrm{a})} \tag{3.5}$$

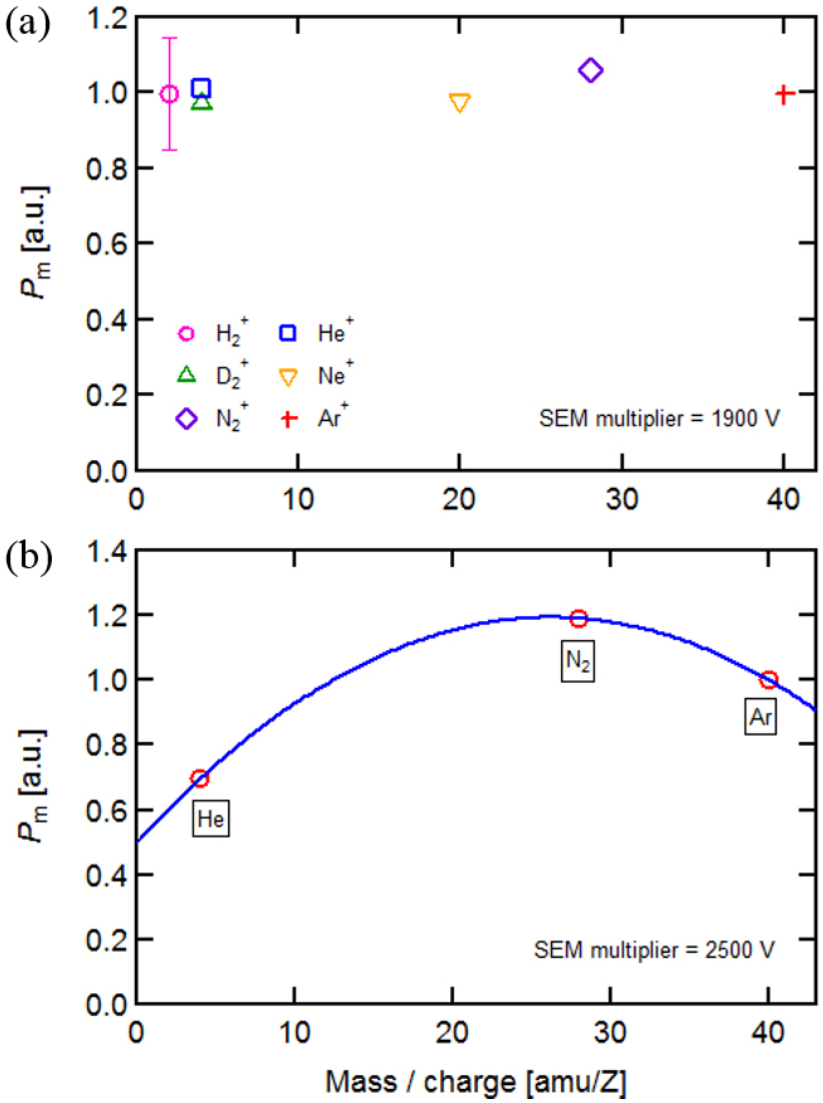

Figure 3.4: Transmission factors measured by RGA mode for different multiplier setting. Each transmission factor P_m is normalized by P_m of Ar. P_m does not show strong dependence on the ion mass when multiplier = 1900 V (a), while it does when multiplier = 2500 V (b). In (b), P_m is fitted by a quadratic function which is used to estimate P_m of other species.

When the energy scanned profile does not obey Gaussian distribution, we need another conversion method. Expressed as a summation, eq. (2.38) is given as

$$I_j(\varepsilon, V_a) = -\left(\frac{2\pi qA}{m_j^2}\right)\delta'^2 \Delta E'_{kin} \sum_{E'_{kin}} P(E'_{kin} - V_a, m_j) E'_{kin} f_v(E'_{kin}). \tag{3.6}$$

Thus, the matrix form of the equation is

$$\begin{pmatrix} I_{j,V_\mathrm{a}=0\ V} \\ \vdots \\ I_{j,V_\mathrm{a}=20\ V} \end{pmatrix} = -\left(\frac{2\pi qA}{m_j^2}\right)\delta'^2\Delta E'_\mathrm{kin}U(E'_\mathrm{kin}-V_\mathrm{a},m_j)\cdot\mathbf{G}(E'_\mathrm{kin}). \tag{3.7}$$

The matrix

$$U=(u_{ij}) \tag{3.8}$$

where

$$u_{ij}=E_j p_{ij} \tag{3.9}$$

which is a product of elements of the vector

$$\mathbf{E}=\left(0,\cdots,E'_\mathrm{kin},\cdots,20\right)\ \mathrm{V}, \tag{3.10}$$

and the matrix

$$(p_{ij})=\begin{pmatrix} P(E'_\mathrm{kin}-V_\mathrm{a}=0\ \mathrm{V},m_j) & \cdots & P(20\ \mathrm{V},m_j) \\ \vdots & \ddots & \vdots \\ P(-20\ \mathrm{V},m_j) & \ldots & P(0\ \mathrm{V},m_j) \end{pmatrix}. \tag{3.11}$$

The vector form of the distribution function

$$\mathbf{G}=\begin{pmatrix} f_v(E'_\mathrm{kin}=0\ \mathrm{V}) \\ \vdots \\ f_v(20\ \mathrm{V}) \end{pmatrix}. \tag{3.12}$$

Therefore, the distribution function $f_v(E'_\mathrm{kin})$ can be obtained from $\mathbf{G}$ by calculating the inverse matrix of U. The transmission function P is measured by experiments using the defocused ion

optics for neutral gas species. The measured P for Ar as a function of V_a is well fitted by Gaussian function with 1.0 eV (FWHM) as shown in fig. 3.3. The ion density fraction is then calculated by integrating the obtained function f_v.

3.3 Optical Spectroscopy

We used a high resolution 1.33 m Czerny-Turner monochromator (McPHERSON, Model 209) equipped with an intensified CCD camera (Princeton Instruments PI-MAX) and a low dispersion spectrometer (Ocean Optics, USB4000) to determine D_2 and N_2 rotational temperature and the density of D atom. The monochromator has a 2400 grooves/mm grating giving a resolution of 0.055 nm (FWHM) at $\lambda = 365$ nm. The density of D atom is determined by measuring emission line from D and Ar atoms with a low dispersion spectrometer (Ocean Optics, USB4000).

3.3.1 Calibration

Those spectrometers are calibrated with an integrating sphere (Gooch & Housego, Model 455-12-1). The integrating sphere is a combination of a tungsten halogen lamp and spherical cavity which inside covered with a diffuse white reflective coating. The radiance distribution of the integration sphere given by the manufacture is shown in fig. 3.5. The distribution is fit by the polynomial function (degree 8) in a range 350-900 nm where lines in our interest exist. Because in this research we only use intensity ratio of spectral lines, relative intensity calibration is performed for both spectrometers by using the integrating sphere.

3.3.2 Neutral gas temperature measurement

In this work, the neutral gas temperatures T_g is determined by measuring the rotational temperatures of D_2 molecules. T_0, the rotational temperature of the ground vibrational state is considered equal to $T_{trans} \sim T_g$ [10][94], as is common practice in unmagnetized and weakly

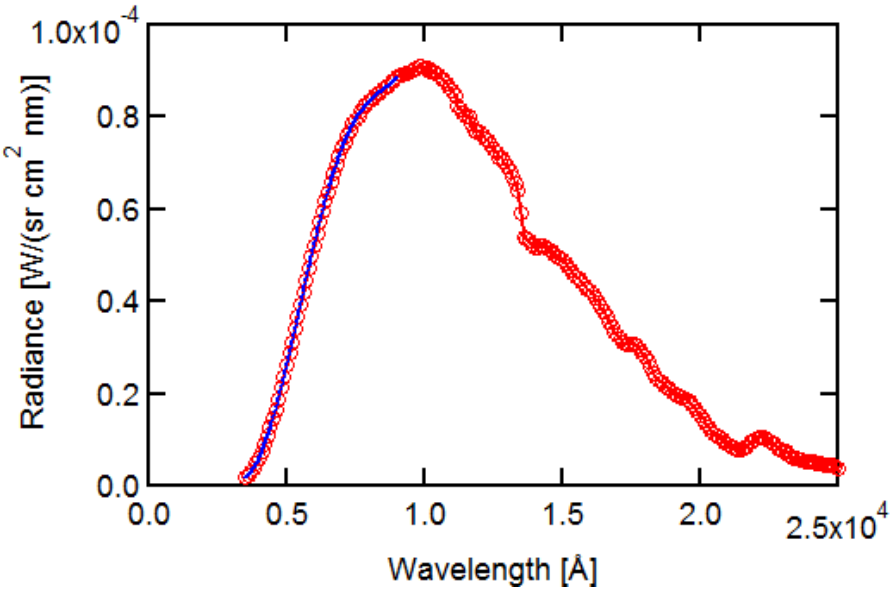

Figure 3.5: Radiance distribution of the integration sphere given by the manufacture and its fitting by the polynomial function (degree 8).

ionized plasmas. The rotational temperature of N_2 was also measured to confirm the thermal equilibrium between D_2 and N_2 molecules. Rotational temperatures of D_2 and N_2 are measured by spectroscopy of the Fulcher-α diagonal band [$\nu' = \nu'' = 2$] of deuterium molecules and the second-positive band from nitrogen molecules using the 1.3 m spectrometer.

For D_2 molecules, only the Q-branches of Fulcher-α band emission ($d^3\Pi_u^- \rightarrow a^3\Sigma_g^+$) existing around 614-617 nm are used because of its strong line intensities. Fig. 3.6 shows typical spectrum of Fulcher-α band emission lines measured by the 1.3 m monochromator. To determine line intensity by excluding background intensities, the lines are fitted with a gaussian function. In the notations of the electronic state, first alphabetic letter corresponds to excited state of electrons. X denotes the ground state, and then $a, b, c, \cdots$ denote the 1st, 2nd, 3rd... excited states. The number on the first alphabets shoulder is spin multiplicity $= 2S + 1$. Next Greek character corresponding to the molecular term is used to refer to each value: $\Sigma, \Pi, \Delta, \Phi, \cdots$ are $0, 1, 2, 3, \cdots$. +/- symbol is the reflections symmetry. u/g represents the symmetric/antisymmetric with respect to the inversion operator i. By supposing the relative population of rotational states obeys Boltzmann distribution, the rotational temperature $T_{\mathrm{rot}}^{\mathrm{d}\nu'}$ of the excited state is estimated by

linear fitting to the function of the term value $F_d(J',\nu')$ [cm^{-1}]

$$\ln\left(\frac{I^{d\nu'J'}_{a\nu''J''}\lambda^{d\nu'J'\ 4}_{a\nu''J''}}{g^{J'}_{\rm as}S_{J'J''}}\right) = \text{const.} - \frac{E_{n',\nu',N'}}{k_{\rm B}T^{d\nu'}_{\rm rot}} \tag{3.13}$$

where $I^{d\nu'J'}_{a\nu''J''}$ is the intensity of a line with a wave length $\lambda^{d\nu'J'}_{a\nu''J''}$; $g^{J'}_{\rm as}$ is the statistical weight of the n',ν',N' ro-vibrational level; $S_{J'J''}$ is the Hönl-London (HL) factors [64][55]. In our case ($\Lambda = 1$, Q branch ($J' - J'' = 0$)),

$$S_{J'J''} = \frac{2J'+1}{4}, \tag{3.14}$$

and

$$E_{n',\nu',N'} = T_{n'} + G_{\nu'} + F_{N'} \tag{3.15}$$

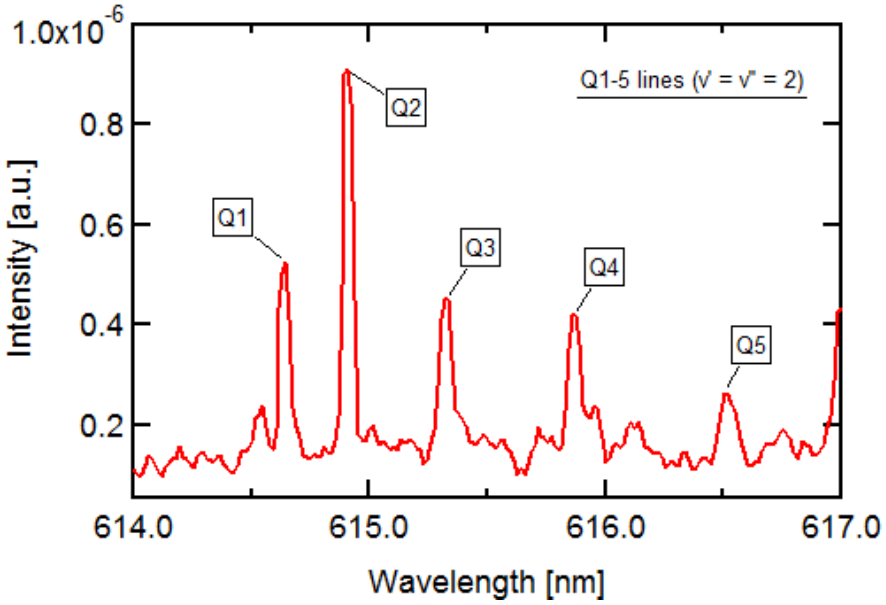

Figure 3.6: Typical Q-branch Fulcher-α band emission lines measured by 1.3 m monochromator.

Table 3.2: Molecular constants for deuterium ground state and a Fulcher-α electronic state. [64]

State	T_e [cm^{-1}]	ω_e [cm^{-1}]	$\omega_e\chi_e$ [cm^{-1}]	B_e [cm^{-1}]	α_e [cm^{-1}]
$d^3\Pi_u$	112707	1678.22	32.94	15.200	0.5520
$a^3\Sigma_g^+$	0	3118.4	64.09	30.429	1.0492

where

$$T_{n'} = T_e, \tag{3.16}$$

$$G_{v'} = \omega_e\left(v+\frac{1}{2}\right) - \omega_e\chi_e\left(v+\frac{1}{2}\right)^2 + \cdots, \tag{3.17}$$

$$F_{J'} = BJ'(J'+1). \tag{3.18}$$

Here,

$$B = B_e - \alpha_e\left(v+\frac{1}{2}\right). \tag{3.19}$$

The molecular constants used in this research are listed on table 3.2. Using the relation

$$\frac{T_0}{B_{X0}} = \frac{T_{rot}(n'v')}{B_{n'v'}}, \tag{3.20}$$

the rotational temperature of the ground state, T_0, can be estimated from the measured rotational temperature of the excited state, T_{rot}.

For N_2 molecules, we measure lines from the vibrational transition $v' = 0 \rightarrow v'' = 2$ of the electronic transition of $C^3\Pi_u \rightarrow B^3\Pi_g$ of the N_2 spectrum of the second positive system (SPS) corresponding to the wavelength range between 377.24 nm and 380.75 nm with $Z = 70$ (number of considered wavelength channels of the measured spectrum) [85][14]. The rotational distribution of the $X^1\Sigma_g$ ground state is unchanged even after electron impact excitation since the electron is too light to change the rotational momentum. Therefore, the line intensity from the

Table 3.3: Molecular constants of nitrogen excited states [Krames:1999]

p	B_e [cm^{-1}]	α [cm^{-1}]	D_e [cm^{-1}]
$B^3\Pi_g$	1.63772	0.01816	0.00000584
$C^3\Pi_u$	1.82677	0.024	0.00000511

excited state $C^3\Pi_u$ keeping the rotational distribution is given as

$$I^{p'\nu'J'}_{p''\nu''J''} \propto \left(\lambda^{p'\nu'J'}_{p''\nu''J''}\right)^{-3} S^{J'}_{J''} \exp\left(-\frac{E^{J'}_{\rm rot}}{k_{\rm B} T^{\nu'}_{\rm rot}(C^3\Pi_u)}\right) \equiv I^{J'}_{J''} \tag{3.21}$$

where $S^{J'}_{J''}$ is the HL factor for N_2 [91],

$$S^{J'}_{J''=J'+1} = 6(J'+1) - 10/(J'+1) \qquad \text{(P branch)} \tag{3.22}$$

$$S^{J'}_{J''=J'} = 10/J' + 10/(J'+1) \qquad \text{(Q branch)} \tag{3.23}$$

$$S^{J'}_{J''=J'-1} = 6J' - 10/J' \qquad \text{(R branch)} \tag{3.24}$$

and

$$E^{J'}_{\rm rot} = B_\nu J'(J'+1) - D_e J'^2 (J'+1)^2. \tag{3.25}$$

Here,

$$B_\nu = B_e - \alpha(\nu + 1/2). \tag{3.26}$$

Table 3.3 shows molecular constants of nitrogen excited states used to determine the N_2 rotational temperature. The calculated spectrum (P, Q, R branches for $J' = 1-70$) which would be observed by the monochromator as

$$I^c_x(\lambda_x) = \sum_{P,Q,R} \sum_{J'=1}^{70} f\left(w, \lambda_x, \lambda^{J'}_{0,J''}\right) I^{J'}_{J''}\left(\lambda^{J'}_{0,J''}, T^{\rm N_2}_{\rm rot}\right) \tag{3.27}$$

where the mathematical description of line broadening caused by the spectrometer,

$$f\left(w,\lambda_x,\lambda_{0,J''}^{J'}\right)=\frac{\sqrt{4\ln 2}}{\pi w}\exp\left[-\frac{4\ln 2}{w^2}\left(\lambda_x-\lambda_{0,J''}^{J'}\right)^2\right], \tag{3.28}$$

w is the line width in FWHM, λ_x is the spectrometer wavelength, $\lambda_{0,J''}^{J'}$ is the theoretical wavelength position of the observed rotational line. Therefore, eq. (3.27) includes three free parameters $T_{\mathrm{rot}}^{\mathrm{N_2}}(C^3\Pi_u)$, w, and $\lambda_{0,J''}^{J'}$ which could be determined by fitting the observed spectrum with the calculated spectrum (eq. (3.27)). For fitting, the least-squares method is used to minimize the function

$$\chi^2\left(T_{\mathrm{rot}}^{\mathrm{N_2}},w,\lambda_{0,J''}^{J'}\right)=\sum_{x=1}^{Z}\frac{\left[I_x^{\mathrm{m}}/I_{\mathrm{max}}^{\mathrm{m}}-I_x^{\mathrm{c}}/I_{\mathrm{max}}^{\mathrm{c}}\left(T_{\mathrm{rot}}^{\mathrm{N_2}},w,\lambda_{0,J''}^{J'}\right)\right]^2}{I_x^{\mathrm{m}}/I_{\mathrm{max}}^{\mathrm{m}}}, \tag{3.29}$$

where 'm' denotes the measured experimental value and I_{max} is the maximum value of the spectrum so that I_x/I_{max} is the normalized intensity. Using a similar relation with eq. (3.20),

$$T_{\mathrm{rot}}^{\mathrm{v}=0}(X^1\Sigma_g^+)=\frac{B_{\mathrm{v}=0}(X^1\Sigma_g^+)}{B_{\mathrm{v}'=0}(C^3\Pi_u)}T_{\mathrm{rot}}^{\mathrm{v}'=0}(C^3\Pi_u), \tag{3.30}$$

we can finally determine the rotational temperature of the N_2 ground state.

3.3.3 Wall loss probability β determination

In the global model, the wall loss probability β for radicals except D are supposed to be 0.99. Yet in some articles, it is suggested that this assumption is not always true [4]. For example, Singh *et al.* [95] found that the loss probability β of the N radical is 0.14. However, this difference of β does not change the calculation results significantly for the conditions of our experiments because the radical species densities are small enough to ignore their contributions in the volumetric reactions. On the other hand, the density of deuterium atom is relatively high so that β of D, β_{D}, can affect calculation results. Therefore, the D wall loss probability, β_{D}, for our experimental configuration was experimentally determined. The possible dominant source and

loss processes of D atom are the electron impact dissociative ionization of D_2 molecules and the wall loss, respectively. Thus, the rate equation of the D density is given by

$$\frac{\partial n_{\mathrm{D}}}{\partial t} = 2n_{\mathrm{D}_2} n_{\mathrm{e}} K_{\mathrm{diss}}(T_{\mathrm{e}}) - n_{\mathrm{D}} \nu_{\mathrm{wD}}. \tag{3.31}$$

By supposing steady state, the equation can be solved for the wall frequency

$$\nu_{\mathrm{wD}} = \left(\frac{n_{\mathrm{D}}}{n_{\mathrm{D}_2}} \right)^{-1} 2n_{\mathrm{e}} K_{\mathrm{diss}}(T_{\mathrm{e}}). \tag{3.32}$$

Hence, by substituting eq. (2.20), β_{D} can be determined using the measured dissociation degree $n_{\mathrm{D}} n_{\mathrm{D}_2}$ and electron density n_{e}. It should be noted that n_{D_2} is for the plasma OFF phase and n_{D} is for the plasma ON phase. The dissociation degree of D can be determined by actinometry [99]. In this technique the spontaneous emissions line intensity of D (486 nm (D_β)) and another actinomer species are measured. In this research, He (501 nm) is used as another actinomer. This method assumes the corona equilibrium where the collisional excitation is balanced by radiative decay. Under this assumption, the line intensity can be expressed as a function of the ground state population density n_1

$$I_{ij} = n_1 n_{\mathrm{e}} k_{1i} \frac{A_{ij}}{\sum_{l<i} A_{il}} = n_1 n_{\mathrm{e}} k_{1i}^{\mathrm{eff}} \tag{3.33}$$

where $k_{1\mathrm{j}}$ is the electron impact excitation rate coefficient, A_{ij} is Einstein A coefficient, and k_{1i}^{eff} is effective the effective rate coefficient. Then, the density of deuterium atom is represented as

$$n_{\mathrm{D}} = \frac{I_{\mathrm{D}_\beta}}{n_{\mathrm{e}} k_{\mathrm{D}_\beta}^{\mathrm{eff}}} = \frac{I_{\mathrm{D}_\beta}}{n_{\mathrm{e}} k_{\mathrm{D}_\beta}^{\mathrm{eff}}} \frac{n_{\mathrm{He}} n_{\mathrm{e}} k_{\mathrm{He}}^{\mathrm{eff}}}{I_{\mathrm{He}_{501}}} \tag{3.34}$$

$$= \frac{I_{\mathrm{D}_\beta}}{I_{\mathrm{He}_{501}}} \frac{k_{\mathrm{He}}^{\mathrm{eff}}}{k_{\mathrm{D}_\beta}^{\mathrm{eff}}} n_{\mathrm{He}}. \tag{3.35}$$

Therefore, by measuring the line intensities of D and He atoms, I_{D_β} and $I_{\mathrm{He}_{501}}$, the dissociation degree can be estimated.

3.3.4 Actinometry

An actinometry method is used to determine the partial pressure of D atom, P_{D}, as an input parameter of the rate equation model. In this technique, the spontaneous emission line intensities of D [486 nm (D_β)] and Ar [750 nm] are measured [100]. The model employed in this method assumes corona equilibrium where collisional excitation is balanced by radiative decay because due to low electron density the probability of electron impact de-excitation processes is much lower than by spontaneous emission. The maximum in our experiment is $n_{\mathrm{e}} \sim 10^{18}\ \mathrm{m}^{-3} \sim 10^{-2} \times n_0$ in which the corona equilibrium can still be assumed. Under this assumption, the line intensity can be expressed as a function of the ground state population density n_1

$$I_{\mathrm{ij}} = n_1 n_{\mathrm{e}} K_{1i} \frac{A_{ij}}{\sum_{l<i} A_{il}} = n_1 n_{\mathrm{e}} K_{1i}^{\mathrm{eff}}, \tag{3.36}$$

where $K_{1\mathrm{i}}$ the electron impact excitation rate coefficient, and A_{ij} is Einstein A coefficient. Therefore, the ratio of the ground state atom density $n_{\mathrm{D}}/n_{\mathrm{Ar}}$ is obtained by measuring the line intensities of D and Ar, I_{D_β} and $I_{\mathrm{Ar}_{750}}$. By measuring n_{Ar} (RGA), n_{D} can then be determined. The direct excitation rate coefficient of D and Ar are taken from [46][23], respectively. A coefficients for each species are taken from NIST Atomic Spectra Database [76].

3.4 Calibration of RGA

The neutral gas pressure is measured by the differentially pumped residual gas analyzer [RGA]. The RGA is connected to the chamber via a right angle valve. While a right angle valve is fully closed, there was still flux into the RGA from the chamber due to slight leak of the valve. We use this setting during the experiment to keep the pressure in RGA lower than 10^{-5} Torr. Because the RGA pressure is proportional to the pressure in the chamber, the calibration factor can be obtained by comparing RGA pressure and the chamber pressure measured by Baratron

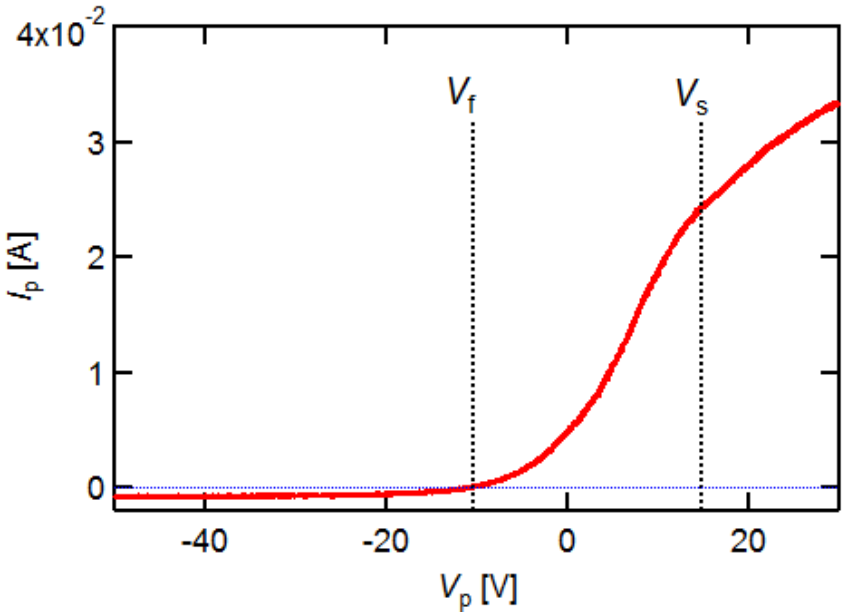

Figure 3.7: Typical I-V characteristic measured by the single tip probe.

gauge. In equation, the calibration factor

$$f_{\mathrm{RGA}} = P_{\mathrm{Baratron}}/P_{\mathrm{RGA}}. \tag{3.37}$$

3.5 Langmuir Probe

The single-tip Langmuir probe is used to measure the electron density and temperature. The probe tip is cylindrical shape, 0.6 mm diameter and 2.2 mm length. While the probe tip is inserted into the probe, the input voltage is swept with 5 Hz and the output current is measured. Using the I-V characteristics obtained, plasmas parameters can be determined. Figure 3.7 shows a typical I-V profile obtained by the single tip probe. This I-V profile can be categorized to 3 sections. The ion saturation region is the first range below V_{f}, the potential at which an isolated probe that cannot draw a current will sit. When the probe bias voltage $V \ll V_{\mathrm{f}}$, the negatively biased probe repels electrons and attracts ion so that the probe current is dominated by the ions. As the bias voltage is raised above V_{f}, the probe current changes sign due to the collection of

plasma electrons and reaches the plasma potential V_s at which the probe has the same potential with the plasma. This range between V_f and V_s, is called the electron repelling region in where I_p is mainly determined by the electrons because of their high mobility. In the range $V_p > V_s$, the probe current begins to saturate. This range is called the electron saturation current. In this research, V_s is defined as the intersection of strait lines drawn tangent to the electron repelling region and tangent to electron saturation region.

In the electron repelling region, the probe current can be given as

$$I_p = I_{es} \exp\left(\frac{e\left(V_p - V_s\right)}{k_B T_e}\right) \tag{3.38}$$

where the I_{es} is the electron saturation current. Taking logarithm and derivative to eq. (3.38),

$$\frac{\mathrm{d}\ln\left(I_p\left(V_p\right)\right)}{\mathrm{d}V_p} = \frac{e}{k_B T_e} \tag{3.39}$$

Therefore, fitting a linear function to I_p plotted on a natural log scale, the electron temperature T_e can then obtained by the slope. However, I_p includes ion current even if it is tiny amount compared to the electron current. Then the extrapolated ion current, which is fitted with the ion current in the ion saturation current, is subtracted from I_p during analysis.

On the other hand, in the ion saturation current region, supposing ions follow the Maxwell-Boltzmann distribution, the current is given by

$$I_{is} = \exp\left(-1/2\right) n_e \mathrm{e} A C_s = 0.61 n_e e A \sqrt{\frac{k_B T_e}{m_{eff}}} \tag{3.40}$$

where A is the surface area of the probe tip. Thus, by substituting T_e determined by eq. (3.39), the electron density n_e is also determined. The effective ion mass m_{eff} is determined by using the ion

species density measured by the EQP into the following equation

$$m_{\text{eff}} = \left[\frac{\sum_j \sqrt{m_j} j_{\text{PM},j,\text{rel}}}{\sum_j j_{\text{PM},j,\text{rel}}} \right]^2 \tag{3.41}$$

where j_{rel} is the ion current fraction measured by the calibrated EQP.

Chapter 4

Molecular Assisted Recombination in H-N plasmas

4.1 Hydronitrogen Molecular Assisted Recombination

In the divertor region with nitrogen seeding, a MAR process mediated by the ammonia molecules can occur via a process similar to that of the hydrocarbon-enhanced MAR [HC-MAR] (Chapter 2). The new MAR process enhanced by the ammonia was originally proposed, and named **Hydronitrogen Molecular Assisted Recombination [HN-MAR]** in our first paper [1]. The HN-MAR process is initiated with charge exchange (CX) reactions forming NH_3^+

$$H^+ + NH_3 \rightarrow H + NH_3^+ \tag{4.1}$$

$$H_2^+ + NH_3 \rightarrow H_2 + NH_3^+, \tag{4.2}$$

or H^+ exchange reactions forming NH_4^+

$$H_3^+ + NH_3 \rightarrow H_2 + NH_4^+, \tag{4.3}$$

These CX reactions are then followed by the dissociative recombination (DR) process of NH_3^+ with electrons

$$NH_3^+ + e^- \rightarrow NH + 2H, \tag{4.4}$$

$$NH_3^+ + e^- \rightarrow NH_2 + H. \tag{4.5}$$

or the DR process of NH_4^+ with electrons

$$NH_4^+ + e^- \rightarrow NH_3 + H, \tag{4.6}$$

$$NH_4^+ + e^- \rightarrow NH_2 + 2H. \tag{4.7}$$

Fig. 4.1 shows rate coefficient data related to the reactions above (eqs. (4.1)-(4.7)) as a function of electron temperature. The rate coefficients for CX reactions (4.1) and (4.2), and the H^+ exchange reaction (4.3) are taken from a compilation by Anicich [6][7], which summarizes a collection of experimentally determined rate coefficients for ion-molecular reactions. We have to note that, because these coefficients were measured only in room temperature and those electron temperature dependence have not been studied, the profiles shown are flat. Higher electron temperature would enhance the charge exchange reaction, because it excites electron state in molecules. The experimental error of these coefficients are within 10%. Then coefficients could be higher than shown values in this electron temperature range. The rate coefficients of DR processes (4.4)-(4.7) were also experimentally obtained [17][25][109]. Those experimental methods were summarized briefly in Chapter 3; descriptions of these techniques have been given in the cited articles.

Fig. 4.1 also shows the reactions for the electron impact ionization of NH_3, and EIR of hydrogen atoms/molecules. In fig. 4.1(a), the direct electron-ion recombination process of NH_3^+ (eq. (4.4)) is 5-10 times faster than the charge exchange process of H^+ and H_2^+ with NH_3

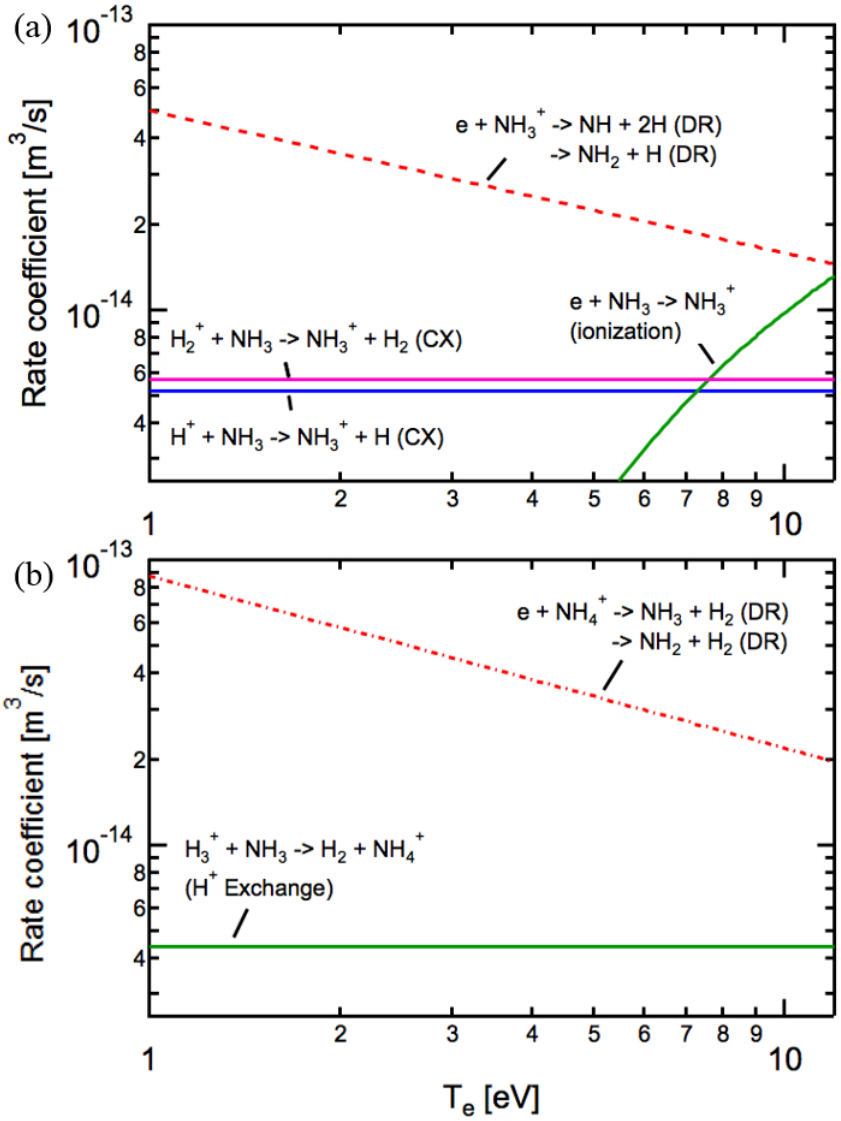

Figure 4.1: Rate coefficients related to neutralization process of H^+, H_2^+, and H_3^+, and recombination processes of NH_3^+ and NH_4^+ with electrons as a function of electron temperature. [1]

(eqs. (4.1)-(4.7)), which is supposed to initiate the reaction above. Therefore, when there is an abundance of electrons, NH_3^+ ions immediately recombine with electrons after its formation by CX reactions. In other words, the CX reactions determine the rate of reactions (4.1), (4.2), (4.4), and (4.5). The rate of the H_2^+ recombination process with electrons is lower than CX reaction rate of (4.2) for the range of T_e shown in the figure. The intersection of the rate coefficient of the direct electron impact ionization of NH_3 with CH reaction (4.1) and (4.2) occurs at $7-8$ eV.

Therefore, the processes described by reactions (4.1), (4.2), (4.4), and (4.5) dominate the NH_3^+ and NH_4^+ kinetics for T_e up to $7-8$ eV. Fig. 4.1(b) shows the dissociative recombination of NH_4^+ (eqs. (4.6) and (4.7)) which is $5-10$ times faster than the H^+ charge exchange reaction (4.3) of H_3^+ with NH_3. The rate of the direct recombination process of H_3^+ with electrons shown in the figure becomes faster than the reaction (4.3) when T_e is larger than 3 eV, H^+ exchange reaction is probably comparable with DR reaction in a higher T_e range because NH_3 density is usually higher than electron density in a weakly-ionized plasma. Thus, the DR reactions (4.6) and (4.7) occur consequently after the reaction (4.3) in the T_e range of few eV.

4.2 Efficiency of HN-MAR in Tokamak divertor plasmas

The calculated loss rates are shown in fig. 4.2 for the rate determining step of those MAR processes, D^+ or H^+ due to HN-MAR, H-MAR for D^+, and EIR for H^+, so accordingly it represents the efficiency of those MAR processes. Here we show rates of deuterium because it is fusion relevant species. Those rates are given for ITER-relevant plasma parameters such as a plasma density of $n_e = 10^{19}$ m^{-3} supposing $n_e = n_{D^+} = 0.1 n_0$ for several density fractions of ND_3 and D_2 as a function of the electron temperature. The equations for the loss rates of HN-MAR, H-MAR, and EIR(H^+) are $n_{D^+} n_{D_2} k_{H-MAR}$ [59], $n_{D^+} n_{ND_3} k_{HN-MAR}$ [7], and $n_{H^+} n_e k_{EIR}$ [30], respectively. It has been reported that D/(D+N) ratio is in the range 90-99% in the ITER divertor [105]. The partial pressure fraction of ammonia observed in the ASDEX-Upgrade tokamak is up to 8% of the injected nitrogen [75]. Using the ITER-relevant parameters, we then estimate that for an ND_3 fraction $f_{ND_3} = 1\%$, the loss rate of HN-MAR exceeds the loss rate of H-MAR in a range $T_e < 1.5$ eV and 4 eV $< T_e$. In the case where $f_{ND_3} = 5\%$, the HN-MAR loss rate becomes larger than the H-MAR loss rate in the entire range of T_e. We note that a ND_3 fraction of larger than 5% could be achieved by directly injecting ND_3, instead of injecting N_2 and then relying on subsequent reactions within the divertor region to produce ND_3. These

estimates then show that the HN-MAR processes should be relevant and perhaps even dominate the recombination in detached divertor plasmas that use N injection.

4.3 Investigation of HN-MAR in PISCES-E device

The HN-MAR process i.e. reactions in eqs. (4.1)-(4.7) are investigated using PISCES-E RF discharges using fusion relevant species D instead of H. Besides general arguments about hydrogen isotopes, notation D is used to discuss experimental and calculation results in further chapters. Direct measurement of signatures from those reactions (line emission etc.) is not practical. Therefore, the reactions in the plasmas are studied by comparing molecular ion density fractions measured by the EQP (Chapter 3) with results from the global model (Chapter 2) for a wide range of plasma conditions. Chapter 5 provides initial experimental results obtained for

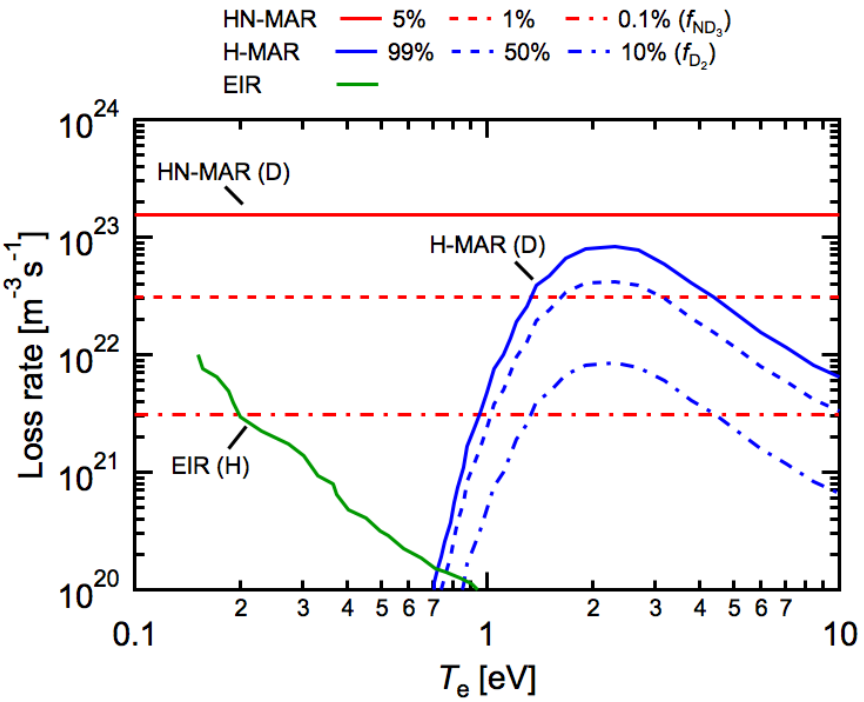

Figure 4.2: Loss rates of $D(H)^+$ due to HN-MAR, H-MAR for D^+, and EIR for H^+. Rates are given for a plasma density of $n_e = 10^{19}$ m^{-3} supposing $n_e = n_{D^+} = 0.1n_0$ for several density fractions of ND_3 and D_2 as a function of the electron temperature. [1]

relatively low plasma densities and provides the first evidence for the first step in the HN-MAR reaction sequence. Those results also then provide a testable prediction: If the plasma density can be raised to high enough values, then volumetric recombination will begin to dominate wall losses in the overall particle balance. Chapters 6 and 7 then describe follow-on experiments in which we produced sufficiently high plasma densities. The results then provide support for the onset of recombination mediated by the HN-MAR processes. Chapter 8 then provides a summary of the main findings, and provides suggestions for future work.

Chapter 5

Neutralization processes of atomic/molecular deuterium ions assisted by ND_3 in low density D_2-N_2 plasmas

5.1 Introduction

The foregoing discussion in Chapter 4 proposed that N injection into D plasmas can lead to recombination via a two-step process. In the first step, ammonia molecules formed as a consequence of the N injection interact with the plasma to form ammonia-based molecular ions. Then, in the second step these molecular ions recombine with plasma electrons, resulting in the release of an ammonia molecular back into the plasma (i.e. the ammonia is recycled and thus is a catalyst), and the elimination of a free electron. The net result is then a loss of D ions and free plasma electrons. In this chapter, the first step in this process, i.e. the formation processes of ND_3^+ and ND_4^+ are investigated in D-N plasmas as the initial step of this new recombination process in plasma discharges. In this chapter, the plasmas were formed with the PISCES-E device setup with configuration [A] (Chapter 3) and systematic scans of the neutral gas pressure ratio,

D_2/N_2 were carried out at fixed plasma power input and total fill pressure. The partial pressure fractions of neutral and ionized molecular fractions were measured by a calibrated electrostatic quadrupole plasma analyzer inserted into the D-N plasma using the techniques described in previous chapters. The results show the formation of ND_3 in a discharge fueled by a combination D_2 and N_2. The total neutral pressure is kept constant as 10 mTorr while the partial pressure of the D_2/N_2 mixture is changed. A low-power (500 W) RF discharge is used to create the low density, low temperature plasma. The typical plasma parameters are $n_e \sim 10^{16}$ m^{-3} and $T_e \sim 3$ eV while the background gas temperature $T_g = 390 - 470$ K. Ion density fractions calculated by a rate equation model including source and loss processes of each ion species are compared to these experimental results. We find that the model can reproduce the observed ion densities in the plasma. Model calculations suggests that the dominant neutralization processes of D^+, D_2^+, and D_3^+ are electron charge exchange or D^+ exchange process forming ND_3^+ or ND_4^+ as final products, and confirm the chemical kinetics of the first step in the HN-MAR process.

5.2 Results

5.2.1 Thermal equilibrium between D_2 and N_2

Both D_2 and N_2 rotational temperatures are measured to make sure that there is thermal equilibrium between both for a plasma ($f_{N_2} = 43\%$, $P_{total} = 3$ mTorr) discharged in configuration [A] (Chapter 3). As described in Chapter 3, the rotational temperature of D_2 molecules was determined by using Q-branches of Fulcher-α band emission ($d^3\Pi_u \rightarrow a^3\Sigma_g^+$) existing around $614 - 617$ nm. The resulting Boltzman plot is shown in fig. 5.1, which is a logarithm plot of d-state populations divided by the nuclear-spin and rotational statistical weights as a function of the total energy. The linear fit to the plot gives $T_0 = 360$ K. Fig. 5.2 shows measured and calculated spectrum of the transition of the second positive system ($\nu' = 0 \rightarrow \nu'' = 2$) of N_2 normalized by the peak intensity at $\lambda = 380.66$ nm. The fitted spectrum, reproducing a kink at

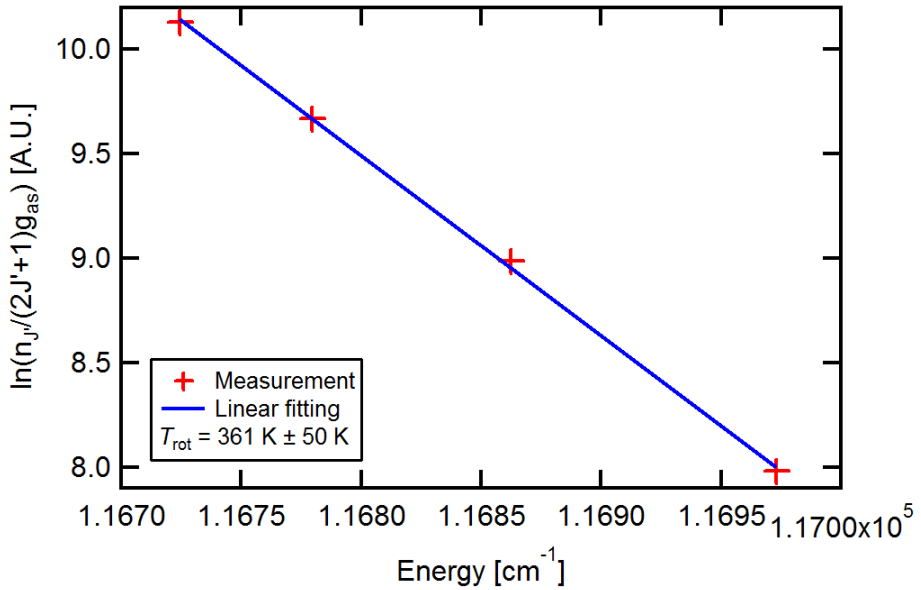

Figure 5.1: Boltzman plot - logarithm plot of d-state (excited state) populations divided by the nuclear-spin and rotational statistical weights as a function of the total energy for $f_{N_2} = 43\%$ ($P_{\text{total}} = 3$ mTorr) plasma using configuration [A] (table 3.1). [1]

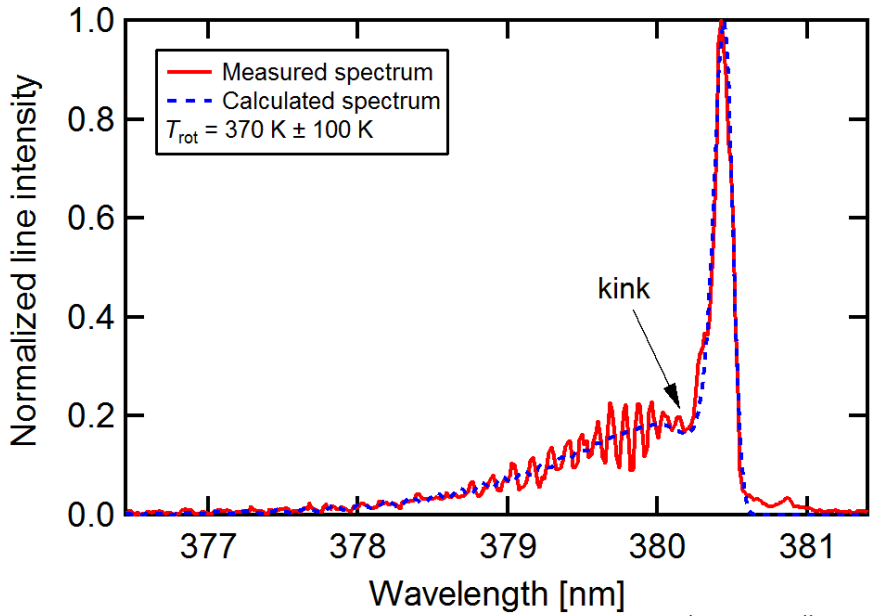

Figure 5.2: Measured and calculated spectrum of the transition $\nu' = 0 \rightarrow \nu'' = 2$ of the second positive system ($d^3\Pi_u \rightarrow a^3\Sigma_g^+$) of N_2 normalized by the peak intensity at $\lambda = 380.66$ nm for $f_{N_2} = 43\%$ ($P_{\text{total}} = 3$ mTorr) plasma using configuration [A]. The fitted spectrum reproduces a kink at 380.4 nm and a tail shape in lower wavelength range. [1]

380.4 nm and a tail shape in lower wavelength range, gives $T_0 = 370$ K. Those temperatures of D_2 and N_2 show quite good agreement. Therefore, in this research, a thermal equilibrium between both gas species is assumed so that the rotational temperature T_0 of D_2 is used as an input parameter, T_g, in the model.

5.2.2 Wall loss probability

The wall loss coefficient for D atom, β_D, is determined by spectroscopy method mentioned in Chapter 3 for the plasma [$T_e = 3.9$ eV, $n_e = 5.1 \times 10^{15}$ m^{-3}, $T_g = 410$ K] using the configuration [A] with special input gas setting $P_{D_2} = 9$ mTorr and $P_{He} = 1$ mTorr. Estimated dissociation degree by spectroscopy was $n_D/n_{D_2(off)} = 0.035$. By substituting this value to eq. (2.20), we found $\beta_D = 0.14$. This value has been used in our global chemical kinetics modeling. In an article [100], determined β_H for aluminum wall with $T_g = 450$ K was $\beta_H = 0.07 \pm 0.03$. However, we note that the anodized aluminum used in our vacuum vessel has microscopic pores on its surface (fig. 5.3). This structure can make actual surface area larger than the flat surface case. Therefore, the determined wall loss coefficient, i.e. sticking coefficient, $\beta_D = 0.14$, which is larger than pure aluminum wall case, seems reasonable.

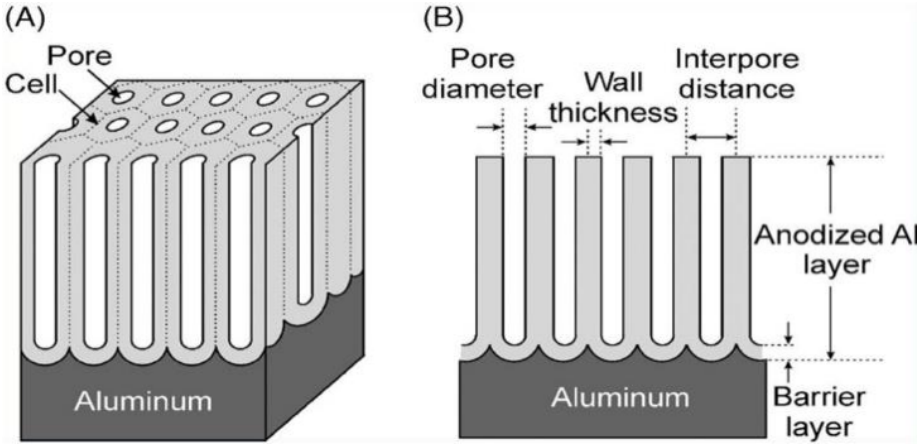

Figure 5.3: Schematic figure of surface structure of the anodized aluminum surface with pores. Typical pore diameter is $0.01 - 0.03$ μm. [27]

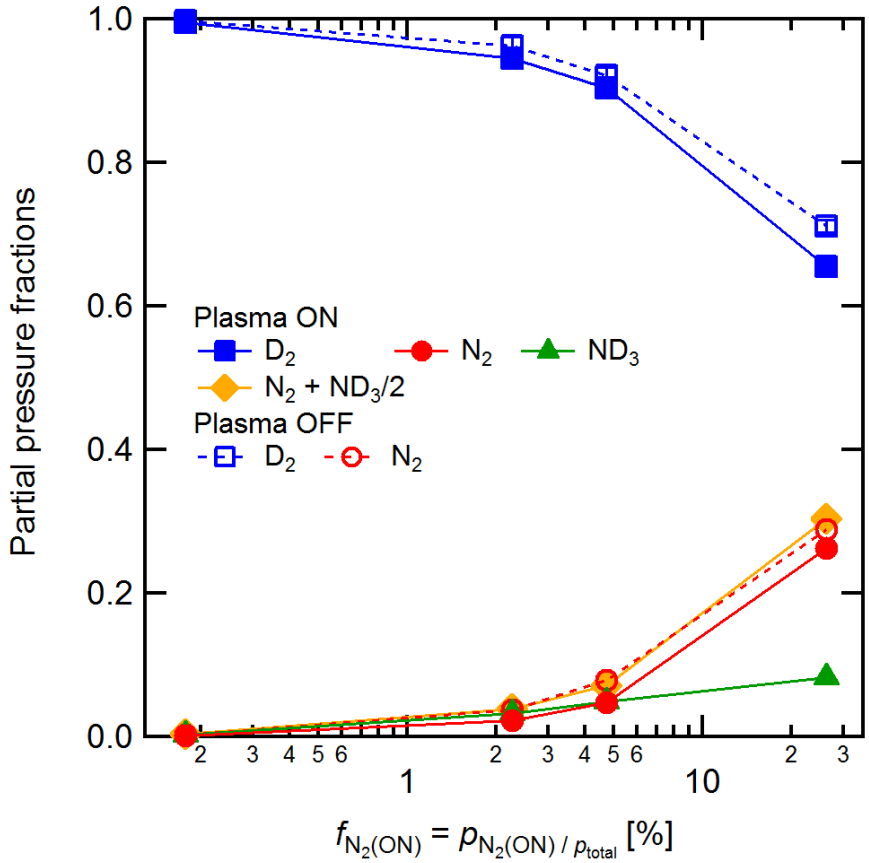

Figure 5.4: Partial pressure fractions of neutral gas measured by the RGA during plasma on (solid) and off (dashed) phase as a function of f_{N_2} for plasma off phase. [1]

5.2.3 Ammonia formation

Fig. 5.4 shows the partial pressure fractions f_j of D_2, N_2 and ND_3 measured by the RGA, where j corresponds to each species, during plasma ON and OFF phase as a function of the N_2 partial pressure fraction f_{N_2} measured when the plasma is off phase. Note that the horizontal axis is logarithmic in scale. N_2 partial pressure fraction is varied from 0.2% to 29% during plasma OFF phase. The figure clearly shows the evidence of formation of ND_3 during the plasma ON phase. f_{ND_3} increases from 0.3% to 8.3% as the input f_{N_2} gas is increased from 0.2% to 29%.

5.2.4 Ion concentration

Fig. 5.5 shows measured and calculated ion density fractions as a function of partial pressure f_{N_2}. The ion fractions of ND^+, ND_2^+, and N^+ are not plotted in the figure, due to the observed very small fractions (< 0.01) for these species across the range of conditions of this experiment. As the N_2 partial pressure during plasma OFF phase, $p_{D_2(off)}$, varied from 0.02 to 2.9 mTorr ($p_{total} = 10$ mTorr), when the discharge was then ignited the plasma density increased from 1.1×10^{16} to 3.9×10^{16} m^{-3}. The gas temperature also increased from 390 to 470 K. The modeled molecular concentrations show good quantitative and qualitative agreement with the measurements especially for the dominant ion species D_3^+, ND_3^+, and ND_4^+. In fig. 5.5(a), the ion species, D_3^+, is shown to be the dominant D-containing ion species for a D partial pressure in the range of $0.02 \leq p_{D_2} \leq 0.23$ mTorr, while the total pressure was kept 10 mTorr. The main creation process of D_3^+ would be $D_2^+ + D_2 \rightarrow D_3^+ + D$ which is also the main volumetric loss channel of D_2^+. The possible creation process of D_2^+ is the electron impact ionization of the background gas D_2. The main loss channel of D_3^+ would be the D^+ exchange reaction with N_2/ND_3 as well as wall losses. Therefore, the fraction of D_2^+ and D_3^+ is expected to decrease when the D_2 partial pressure decreases. This trend can be seen in fig. 5.5(a). For the dominant molecular ion species D_3^+, ND_3^+, and ND_4^+ the model also shows quantitative agreement with the EQP measurements. The calculated electron temperatures $T_e \sim 3$ eV is in reasonable agreement with the measured electron temperature $T_{e,exp} \sim 3.8 \pm 0.5$ eV (fig. 5.6). Thus the model accurately predicts the density of ND_3^+, and ND_4^+, which are the two species that are thought to play a key role in causing plasma recombination in mixed D_2-N_2 plasmas.

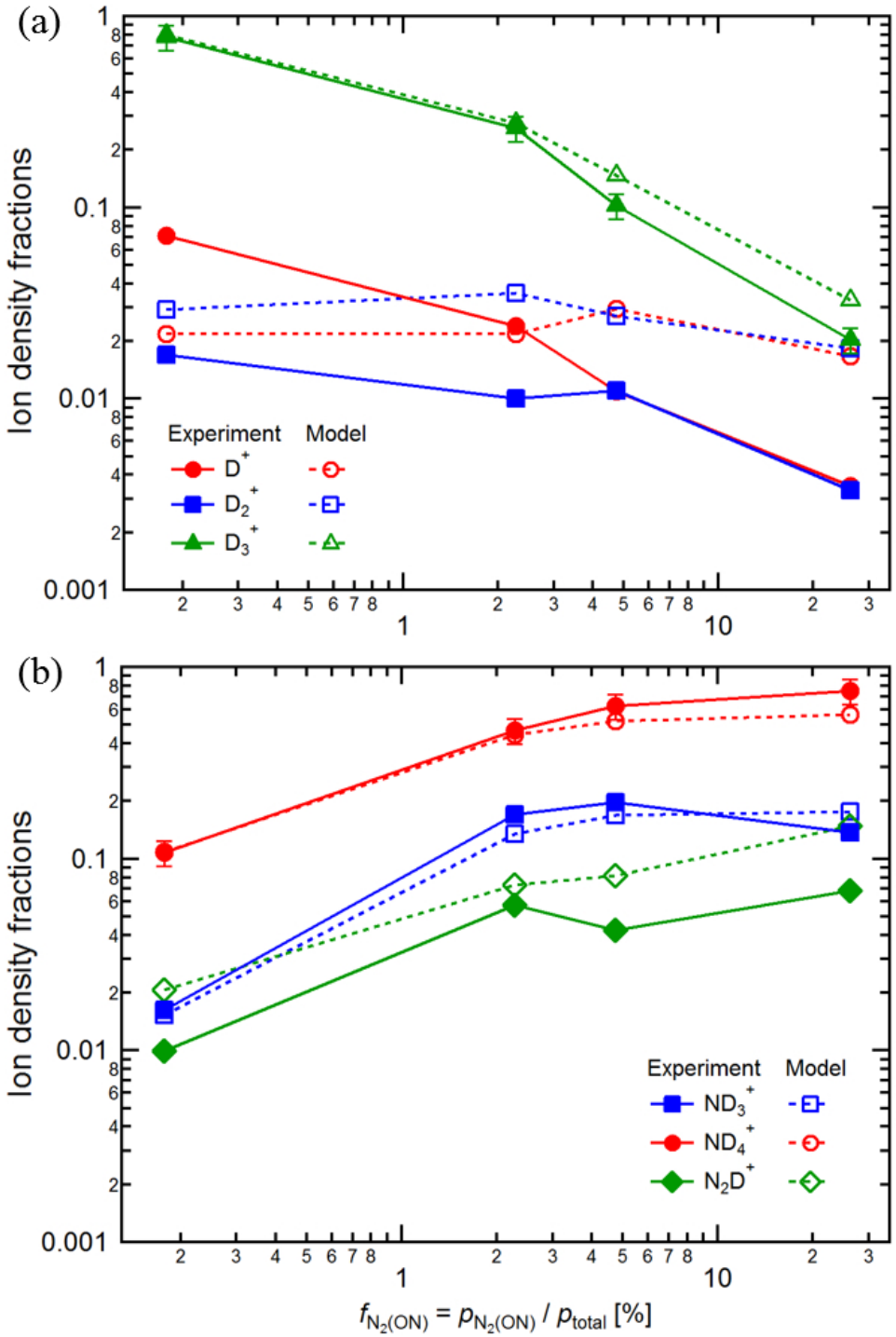

Figure 5.5: Measured and calculated ion density fractions as a function of the N_2 partial pressure fraction for (a) D^+, D_2^+, D_3^+, (b) ND_3^+, ND_4^+, and N_2D^+. [1]

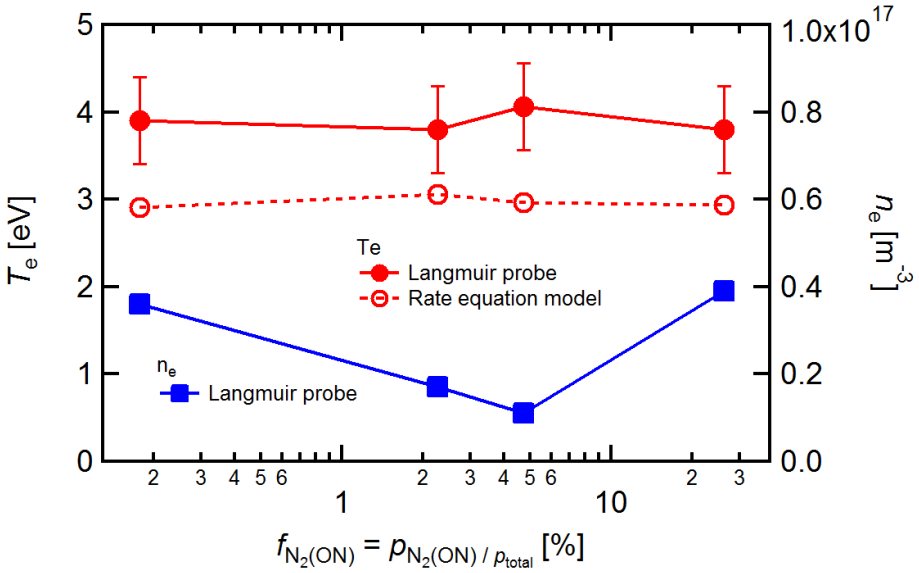

Figure 5.6: Electron temperatures and its densities as a function of f_{N_2} for plasma off phase. The error bar ± 0.5 eV of the electron temperature measured by the Langmuir probe is empirically obtained. [1]

5.3 Model calculation results about formation process of ND_3^+ and ND_4^+

In this section, the global chemical kinetics model (global model) is used to examine the formation process of ND_3^+ and ND_4^+ . The calculated rates of processes showing minor contribution for production are excluded from the figures for clarity.

5.3.1 Loss processes of D^+, D_2^+, and D_3^+

Fig. 5.7 shows the calculated loss processes of the deuterium atomic/molecular ions. According to fig. 5.7(a), the main D^+ loss path for $p_{N_2}/p_{tot} > 3\%$ is the charge exchange reaction with ND_3,

$$D^+ + ND_3 \rightarrow D + ND_3^+ \tag{5.1}$$

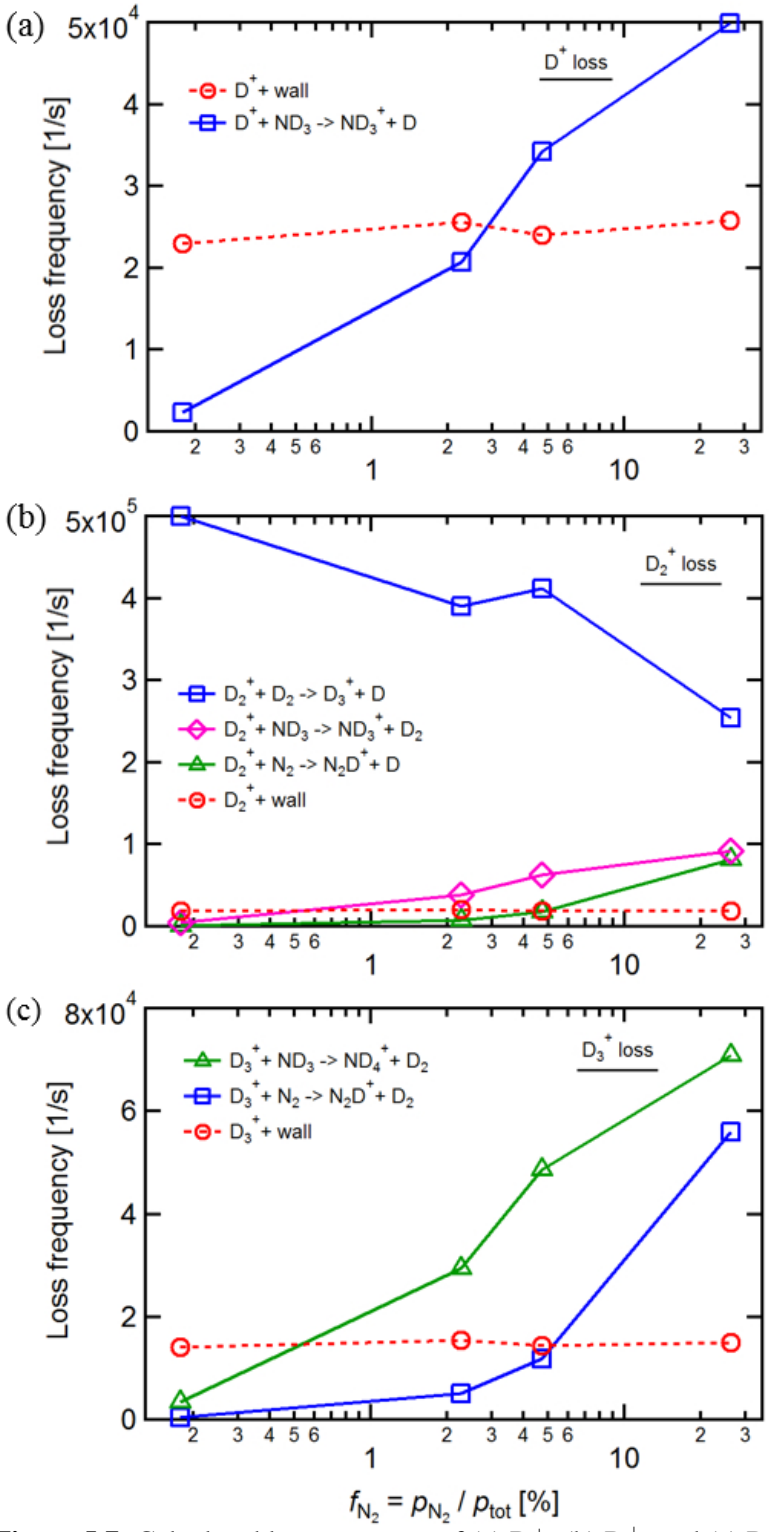

Figure 5.7: Calculated loss processes of (a) D^+, (b) D_2^+, and (c) D_3^+ [1]

which is identical with the reaction eq. (4.1). Fig. 5.7(b) shows

$$D_2^+ + D_2 \rightarrow D_3^+ + D \tag{5.2}$$

as the main loss process for D_2^+. The charge and D^+ exchange reaction with ND_3 and N_2 are listed as the second and third loss processes respectively,

$$D_2^+ + ND_3 \rightarrow D_2 + ND_3^+, \tag{5.3}$$

$$D_2^+ + N_2 \rightarrow D + N_2D^+. \tag{5.4}$$

Eq. (5.3) is identical with the reaction eq. (4.2). The model calculations predict that the latter reaction (eq. (5.4)) becomes dominant when $f_{N_2} > 25\%$. For D_3^+ (fig. 5.7(c)), the main loss channel for $p_{N_2}/p_{tot} > 0.5\%$ is the D^+ exchange with ND_3

$$D_3^+ + ND_3 \rightarrow D_2 + ND_4^+ \tag{5.5}$$

which is identical with the reaction eq. (4.3). Another significant loss process with N_2 is

$$D_3^+ + N_2 \rightarrow D_2 + N_2D^+ \tag{5.6}$$

which becomes a dominant process when $f_{N_2} > 5\%$. Therefore, the dominant volumetric loss processes, i.e. neutralization processes of D^+, D_2^+, and D_3^+, form ND_3^+, ND_4^+, and N_2D^+.

5.3.2 Loss process of N_2D^+

Fig. 5.8 shows calculated loss frequencies of N_2D^+. The wall loss reaction is the main loss process in low N_2 partial pressure condition. However, the D^+ exchange reaction with ND_3,

$$N_2D^+ + ND_3 \rightarrow N_2 + ND_4^+ \tag{5.7}$$

is the dominant loss process when $f_{N_2} > 2\%$. It means that neutralization processes of D_2^+ and D_3^+ mainly forms ND_3^+ and ND_4^+ as a consequence.

5.3.3 Formation processes of ND_3^+ and ND_4^+

Fig. 5.9 shows the calculated formation rates of ND_3^+ and ND_4^+. In fig. 5.9(a), we see that the dominant creation process of ND_3^+ is the direct electron impact ionization process,

$$ND_3 + e^- \rightarrow ND_3^+ + 2e^-. \tag{5.8}$$

The charge exchange reaction (eq. (5.3)) also contributes $20-30\%$ of the total ND_3^+ production rate. The charge exchange reaction (eq. (5.1)) is also the third channel ($\sim 10\%$) of the ND_3^+ production. On the other hand, in fig. 5.9(b), we see that the main creation process of ND_4^+ is the

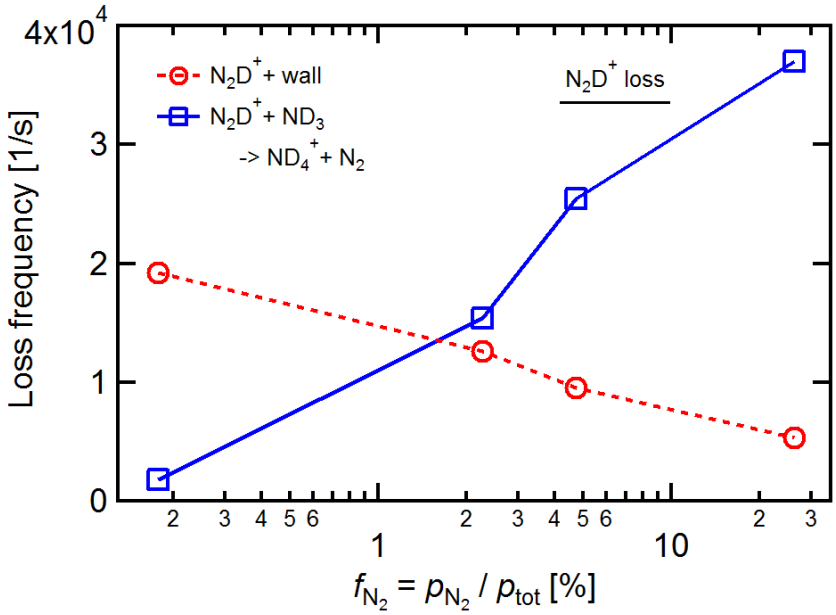

Figure 5.8: Calculated loss frequency of N_2D^+. When $f_{N_2} > 2\%$, the main loss process is the D^+ exchange reaction with ND_3. [1]

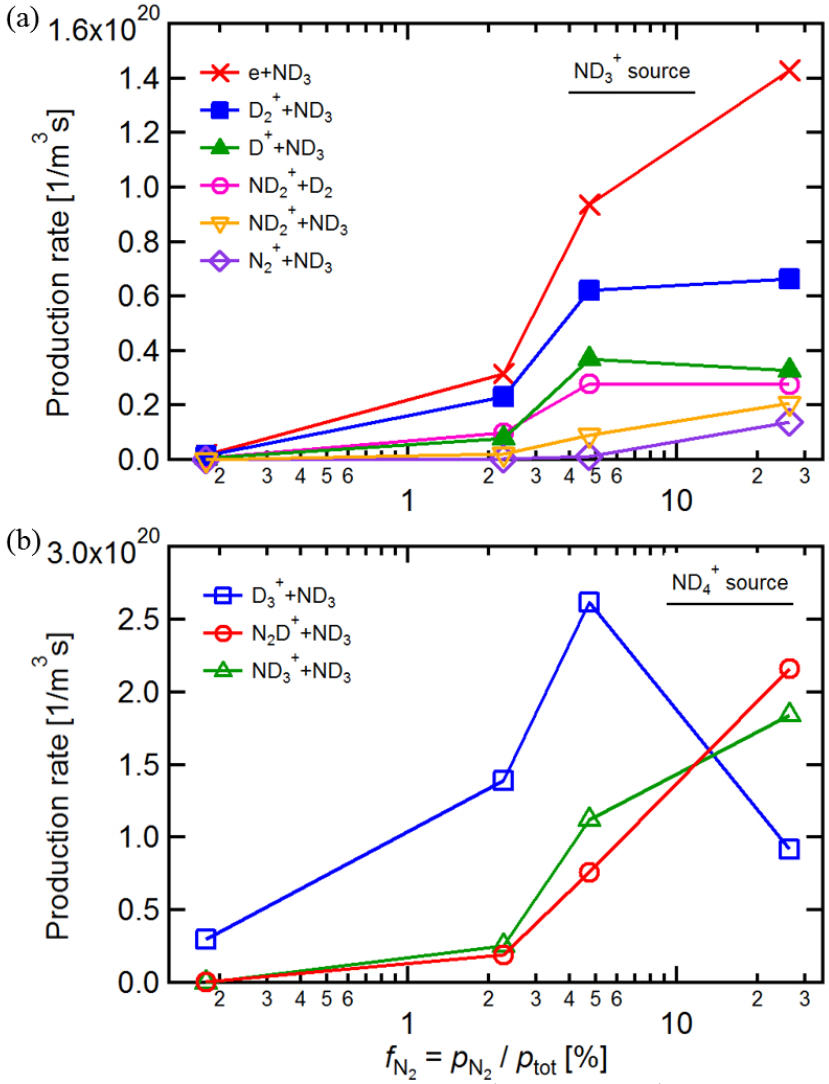

Figure 5.9: Calculated production rate of (a) ND_3^+ and (b) ND_4^+ as a function of N_2 partial pressure fraction. [1]

D^+ exchange reaction (eq. (5.5)) in the range where $f_{N_2} < 10\%$. In this range, the D^+ exchange reaction of N_2D^+, eq. (5.7) and

$$ND_3^+ + ND_3 \rightarrow ND_2 + ND_4^+ \tag{5.9}$$

are the secondary production paths. When $f_{N_2} > 10\%$, those two reactions become dominant source reaction. Therefore, for the condition $f_{N_2} < 10\%$, it can be said that formation amount of

ND_4^+ would mainly dependent on D_3^+ while ND_3^+ would be formed through complex path ways not only related to D^+ and D_2^+ species.

5.4 Evidence of HN-MAR 1st step

The above results provide a testable prediction. In particular, the results shown in fig. 5.9(b) suggest that the formation process of ND_4^+ is dominated by eq. (5.5) and so the density of ND_4^+ should be positively correlated to the density of D_3^+ when the density of ND_3 is kept constant. In order to test this expectation, we carried out an experiment in which ammonia was directly injected into D_2 fueled discharges where the total pressure, ammonia partial pressure and n_e were kept constant at $P_{total} = 10$ mTorr, $P_{ND_3} = 0.3$ mTorr and $n_e = 2 \times 10^{16}$ m^{-3} respectively. In this experiment $P_{N_2} = 0.04$ mTorr was an order-of-magnitude lower than P_{ND_3}, and so the reactions involving N_2 can be neglected. During this experiment the measured T_e only increased from 4.4 to 4.8 eV as the input power increased from 1500 to 3000 W. According to eq. (2.11), the density of ions is inversely proportional to the wall loss which is proportional to the square root of T_e (eq. (2.21)) and so the estimated ion wall loss rate due to increased T_e only changes by a factor $\sqrt{T_{e,3000\ W}/T_{e,1500\ W}} \sim 1.04$. Thus in this low plasma density configuration, ND_3^+ and ND_4^+ are mainly lost onto the wall at a rate that does not change appreciably with heating power, and so the loss frequency of ND_3^+ and ND_4^+ can be considered nearly constant. Figure 5.10 shows the experimentally measured ion density fractions of ND_4^+ for D_2 plasmas with a fixed ND_3 seeding plotted vs. the RF power input.The results show that the fraction of D_3^+ density decreases from 63% to 50% with increasing of input power as the fraction of ND_4^+ also decreases more than half, from 12% to 5% - and thus the two are positively correlated as predicted. On the other hand, according to the results in fig. 5.9, the formation process of ND_3^+ includes several reactions. In particular, while the direct electron impact ionization is the dominant source, other processes show comparable contributions to ND_3^+ production. As a result, the fraction of ND_3^+ in fig. 5.10

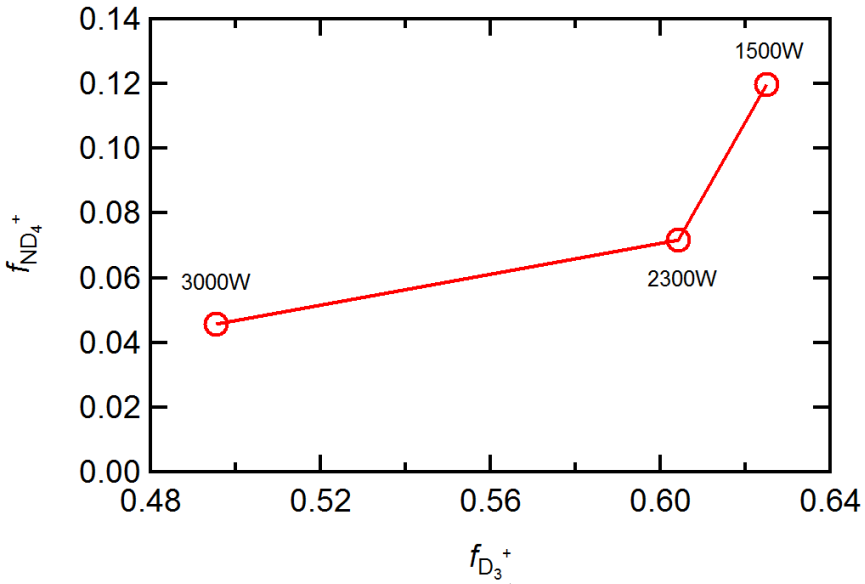

Figure 5.10: Measured ion density fractions of ND_4^+ as a function of the fractions of D_3^+ under $P_{tot} = 10$ mTorr, $n_e = 2 \times 10^{16}$ m^{-3}, $T_e = 4.5$ eV, and $P_{ND_3} = 0.3$ mTorr. [1]

does not show positive correlation with the fractions of D^+ and D_2^+, which increasingly can form ND_3^+ through eq. (5.1) and (5.3) as the input power is increased. This experimental result qualitatively supports the proposed ND_3^+ and ND_4^+ formation processes outlined in fig. 5.9.

5.5 Conclusion

In conclusion, the neutralization process of the deuterium atomic and molecular ions is thought to occur by the formation of ND_3^+ and ND_4^+ molecular ions via charge exchange reactions with ND_3. Fig. 5.11 shows a comprehensive cartoon model diagram of the dominant loss reactions of ions for the D_2-N_2 plasmas, based on the results from our modeling. The direct wall loss reactions of D^+, D_2^+, and D_3^+ are excluded. For the range of f_{N_2} explored in this work, D^+ are mainly lost by neutralization processes throughout the electron and D^+ charge exchange reactions with ND_3 (see fig. 5.7(a)). For $f_{N_2} < 10\%$ configuration, D_2^+ is mainly converted to D_3^+ due to charge exchange reaction with D_2. D_3^+ is subsequently converted to ND_4^+ through two dominant paths. First, the D^+ exchange process of D_3^+ with ND_3 produces ND_4^+, and the

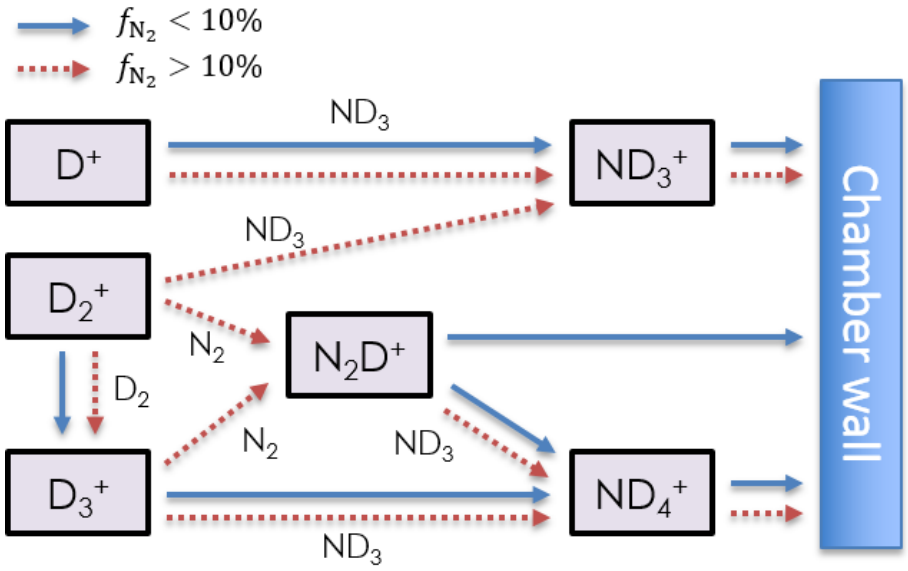

Figure 5.11: Schematic description of loss processes of D^+, D_2^+, and D_3^+ for $f_{N_2} < 10\%$ (solid) and $> 10\%$ (dashed). The direct wall loss reactions of D^+, D_2^+, and D_3^+ are not shown here. Arrows correspond to a path having rates larger than 10% of the total loss rate of each species. [1]

evidence of this process is observed experimentally (Section 5.4). Second, D_3^+ is neutralized by D^+ exchange reaction with N_2. The resulting N_2D^+ ion undergoes another D^+ exchange reaction again with ND_3, and finally ND_4^+ is produced. For $f_{N_2} > 10\%$ configuration, D_2^+ is also converted to N_2D^+ by D^+ exchange with N_2 besides forming D_3^+. D_3^+ is neutralized by a dominant path to N_2D^+.

Summarizing this chapter, we found that the main neutralization process of D^+, D_2^+, and D_3^+ involves CX with ammonia, ND_3, producing ND_3^+ and ND_4^+ in the weakly ionized D-N plasma. This process is the first step of the new HN-MAR process (eqs. (4.1)-(4.3)). In this experiment, electrons are mainly lost onto the chamber wall due to low density electrons. However, model calculations suggest that the electron-ion recombination process of ND_3^+ and ND_4^+ (eqs. (4.4)-(4.7)) will exceeds the wall loss when high density plasma, namely, $n_e > 10^{17}$ m^{-3}. Therefore, to observe this second step in the HN-MAR recombination process, the high density plasma has to be used. In next chapter, the results about these experiments are reported.

5.6 Acknowledgements

Chapter 5, including text and data, is in part a reprint of the material as it appears in S. Abe, R.P. Doerner, G.R. Tynan, Neutralization processes of atomic/molecular deuterium ions assisted by ND_3 in low density D_2-N_2 plasmas, Physics of Plasmas, 25, 073507 (2018). The dissertation author was the primary investigator and author of this paper. This work was supported by the U.S. Department of Energy Grants No. DE-FG02-07ER54912.

Chapter 6

Hydronitrogen Molecular Assisted Recombination (HN-MAR) processes in ammonia seeded deuterium plasmas

6.1 Introduction

The previous chapter provided experimental and modeling results that focused on the formation processes of ND_3^+ and ND_4^+, which form the first step in the HN-MAR two-step recombination process. Those experiments were intentionally carried out at a low densities, $n_e < 10^{16}$ m^{-3} in order to avoid the second step in the HN-MAR process. That study provided evidence that ammonia molecules formed upon injection of N into D-containing plasmas play the key role in the HN-MAR process. This finding then suggested the question: What happens if we simply directly inject ammonia into D-containing plasmas, and thereby skip the formation of ammonia within the discharge? In this chapter, we use higher plasma density of up to $n_e \sim 3 \times 10^{17}$ m^{-3} to investigate the volumetric recombination scheme of the HN-MAR for ITER relevant plasma detachment operation. Working at this higher plasma density allows us to see the

importance of the electron impact recombination reactions which is negligible compared with the wall loss reaction in low density plasmas. The formation and destruction processes of intermediate products of HN-MAR, namely ND_3^+ and ND_4^+, are investigated in plasmas formed in D-ND_3-Ar mixtures. The ion density fractions measured by a calibrated electrostatic quadrupole plasma analyzer is compared with a rate equation model to obtain detailed chemical processes in the plasmas. The flow rates of injected gasses, D_2, ND_3, and Ar are kept constant while the density of neutral gas species is measured by a residual gas analyzer. When the RF input power is scanned from $P_{RF} = 500 - 3300$ W, the plasma parameters vary from $n_e \sim 4 \times 10^{15} - 3 \times 10^{17}$ m^{-3}, $T_e \sim 2.5$ eV, and $T_g = 390 - 910$ K. An actinometry method using D and Ar emission lines gives the deuterium dissociation degree $n_D/(2n_{D_2} + n_D) = 4 - 19\%$. As increasing the plasma density above $n_e > 10^{17}$ m^{-3}, the EQP measured decreasing of ND_4^+ density fraction. We found this phenomenon would be the evidence for the dissociative recombination reactions in the HN-MAR process.

6.2 Description of Experiment

The PISCES-E device was put into configuration [B] (Chapter 3) for these experiments in this chapter. The input power is scanned from 500 W to 3300 W in this experiment while the reflected power is less than 1% of input power. Ar is additionally injected with D_2 and ND_3 to realize the high density plasmas up to $n_e \sim 10^{17}$ m^{-3}. Partial pressures of each gas species during plasma OFF phase are $p_{D_2} = 10$ mTorr, $p_{ND_3} = 0.2$ mTorr, $p_{Ar} = 10$ mTorr. The two magnetic coils are centered on and surround the double loop antennas. Two other magnet coils are located directly below and centered on the chamber. Those coils make a magnetic field in the same direction. Operating the top coils with the current 50 A and the bottom coils with 120 A creates a magnetic field of 25 gauss at the center of the belljar, and 30-40 gauss at the entrance orifice of the EQP (fig. 6.1). The density of D atom is determined by measuring emission line

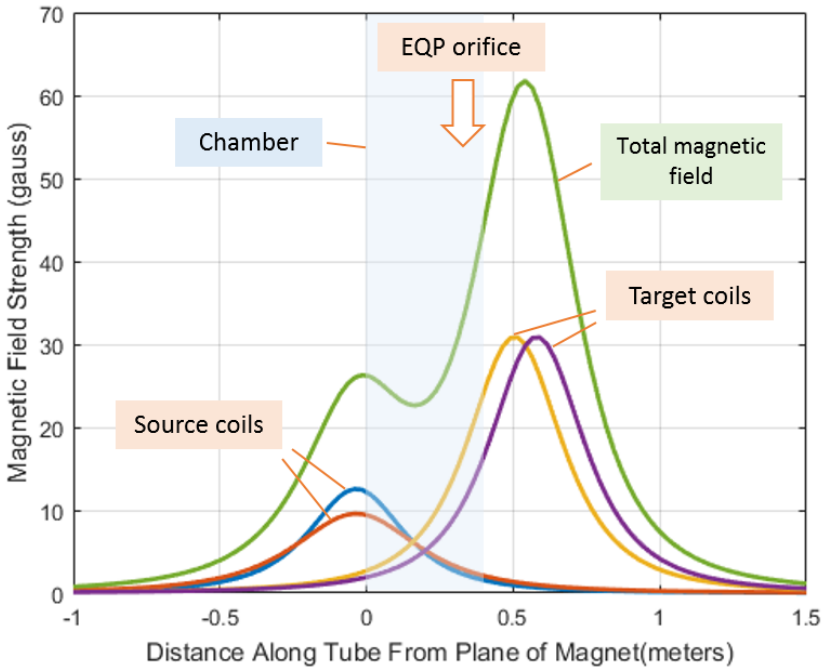

Figure 6.1: Calculated magnetic field for configuration [B] along z axis.

from D and Ar atoms with a low dispersion spectrometer. The heat shield used to protect the mass spectrometer head from these higher density plasmas had a 1.5 mm diameter orifice.

6.3 Rate equation model

The model used in this paper is identical with one used in previous Chapter 5 [1] with the addition of equations to describe the chemical kinetics of Ar-containing species (including meta-stable argon species). Those coefficients are listed in tables 2.1-2.7. The coefficients for the most of the Ar species are taken from [97] except for the recombination processes,

$$Ar^+ + e^- \rightarrow Ar \tag{6.1}$$

taken from [49] and

$$ArH^+ + e^- \rightarrow Ar + H \tag{6.2}$$

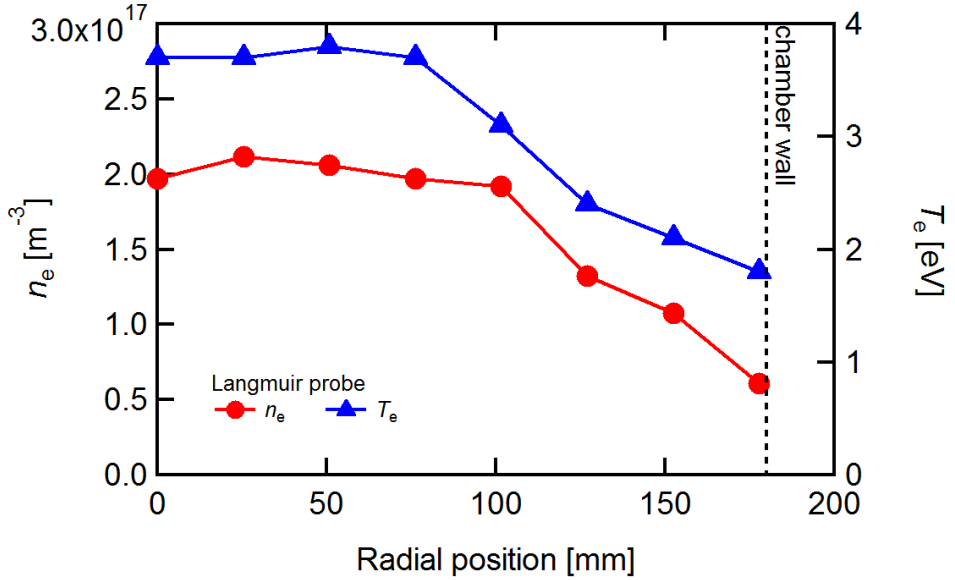

Figure 6.2: Radial profile of plasma parameters T_e and n_e of 1500 W plasma at $z = 130$ mm. Both parameters drop for $r = 100$ mm, and n_e around chamber wall becomes less than a half of the centeral location parameters

taken from [17].

6.4 Parameter measurements

6.4.1 Radial plasma profiles

Fig. 6.2 shows a radial profile of plasmas parameters T_e and n_e of 1500 W plasma at $z = 130$ mm. It is seen that both parameters drop for $r > 100$ mm, and become less than a half of the central location parameters around the chamber wall. The effective wall loss rate $X^i_{loss} = n_{b,i}\nu_{wi}$ is used in the model instead of eq. (2.14), where $n_{b,i}$ is the ion density near the chamber wall region and

$$\nu_{wi} = \frac{A}{V} u_b, \tag{6.3}$$

the wall loss frequency, in which ions are assumed to enter the sheath region with the Bohm velocity u_b. As it can also be seen in fig. 6.2, the plasma density around the chamber wall is

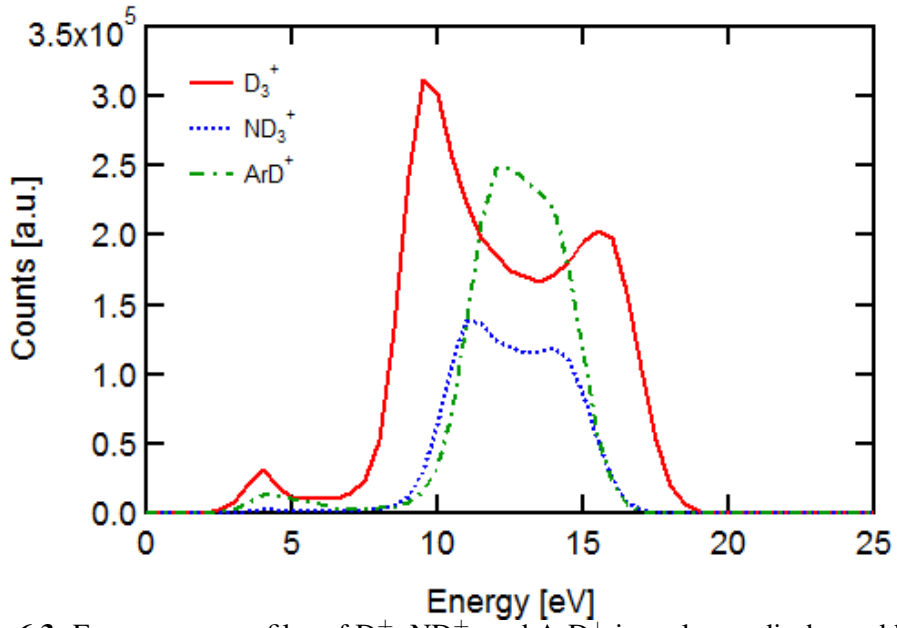

Figure 6.3: Energy scan profiles of D_3^+, ND_4^+, and ArD^+ in a plasma discharged by 3300 W input power. The profiles show broad and bi-modal function especially for light species.

about 1/3 of the center value. Therefore, we assume $n_{b,i} = n_{c,i}/3$ in the model to estimate the wall loss rate where c notes a parameter at center. It should be noted that the rate coefficients of ion-molecular reactions are mainly obtained by experiments at room temperature while the T_g range is $390-910$ K in experiments. However, this will not affect the rate coefficients significantly because almost of those coefficients are not function of T_g (see Section 2.3 and tables 2.1-2.7).

6.4.2 EQP signals

Fig. 6.3 shows energy scan profiles of I_j for different ion species in a high power plasma ($P_{input} = 3300$ W). In our apparatus, for high power plasmas > 1500 W, a broad and bi-modal profile is observed, similar to results reported elsewhere [11]. This type of profile can be explained by recognizing that the EQP is measuring the time-averaged potential, while the instantaneous plasma potential likely experiences a sinusoidal oscillation of about 6-8 V due to weak capacitive coupling between the RF antenna and the plasma discharge. The actual instantaneous distribution function is most certainly a Maxwell-Boltzmann distribution with an ion temperature in the range

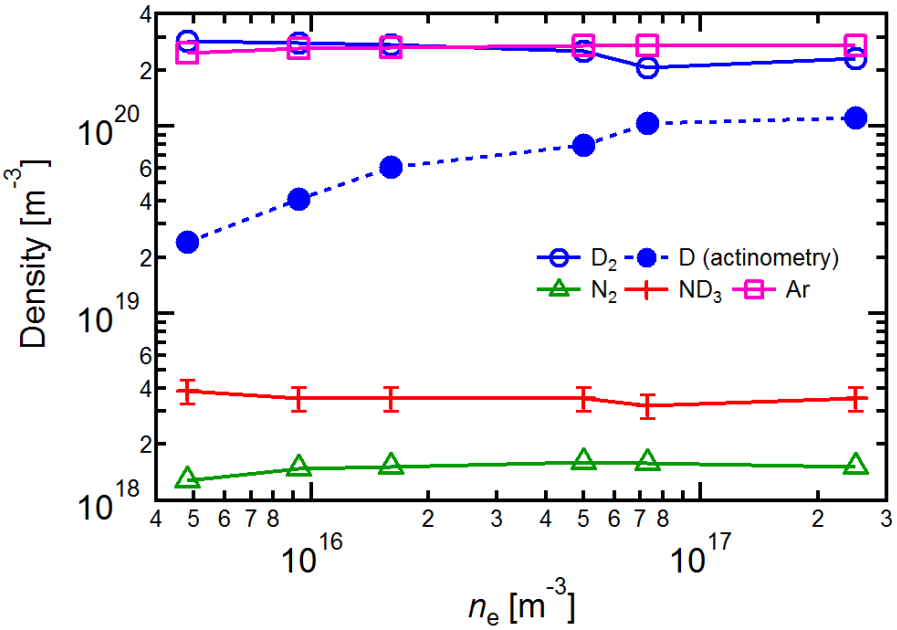

Figure 6.4: Density of neutral gas measured by a calibrated RGA and actinometry during plasma ON phase as a function of the electron density.

of $0.1-1.0$ eV. This type of scanned profiles can be converted to the ion density using the method mentioned in Section 3.2.4.

6.4.3 Densities of neutral gasses

The flow rates of input gas species, D_2, ND_3, and Ar, are kept constant. Fig. 6.4 shows the measured density of D_2, D, N_2, ND_3, and Ar. Density of D is measured by the actinometry method. Densities of other species are measured by the calibrated RGA. The density of ND_3 and N_2 is not strongly dependent on the input power. On the other hand, the density of D depends on input power, i.e. the dissociation degree, $p_D/(2p_{D_2}+p_D) = 4-19\%$ while input power increases from 500 to 3300 W. Those measured densities are used as input parameters in the rate equation.

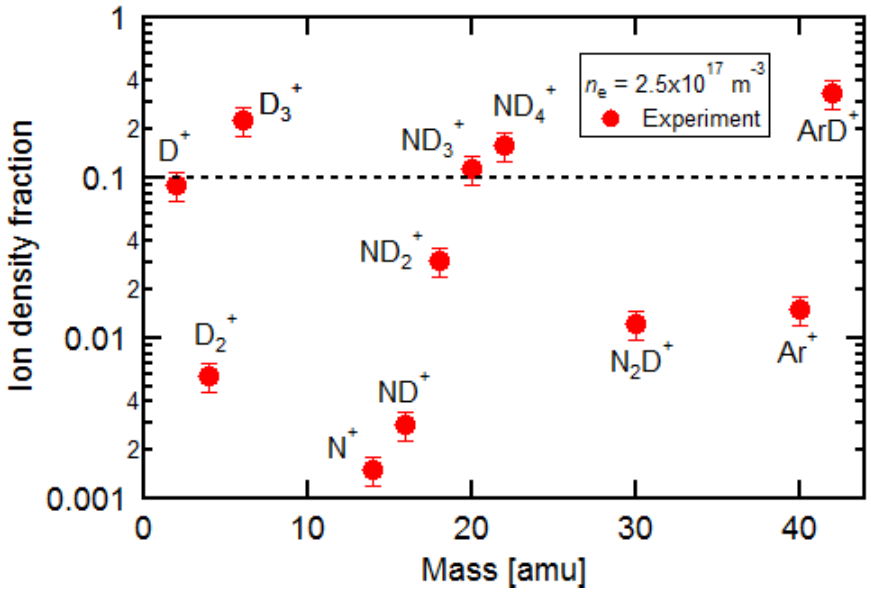

Figure 6.5: Ion density fractions measured by the EQP analyzer for the high density $n_e = 2.5 \times 10^{17}$ m^{-3} plasma when $P_{input} = 3300\,W$.

6.5 Ion concentration and formation/destruction processes

6.5.1 Ion fractions of ND_3^+ and ND_4^+

Fig. 6.5 shows measured ion density fractions for each species in the 3300 W discharged plasma. In this chapter, we focus on the dominant ion species which fraction > 0.1 such as D_3^+, ND_3^+, ND_4^+, ArD^+ to investigate the formation and destruction process of the ion species ND_3^+ and ND_4^+ because those are the intermediate products during the HN-MAR process. Fig. 6.6 shows the ion density fractions of ND_3^+ and ND_4^+ as a function of the electron density. Two types of model calculation results are shown. The first includes the electron-ion recombination terms (model A), while the second neglects the recombination terms (model B). In fig. 6.6(a) for ND_3^+, the both model A and B show comparable results for the entire electron density range. Although both calculation results shows discrepancy with the experimental results in a lower density range $n_e < 10^{17}$ m^{-3}, in a higher density region $n_e \sim 10^{17}$ m^{-3} the calculations approach the experimental value in a factor of 2. The reason of discrepancy might be due to plentiful Ar^+

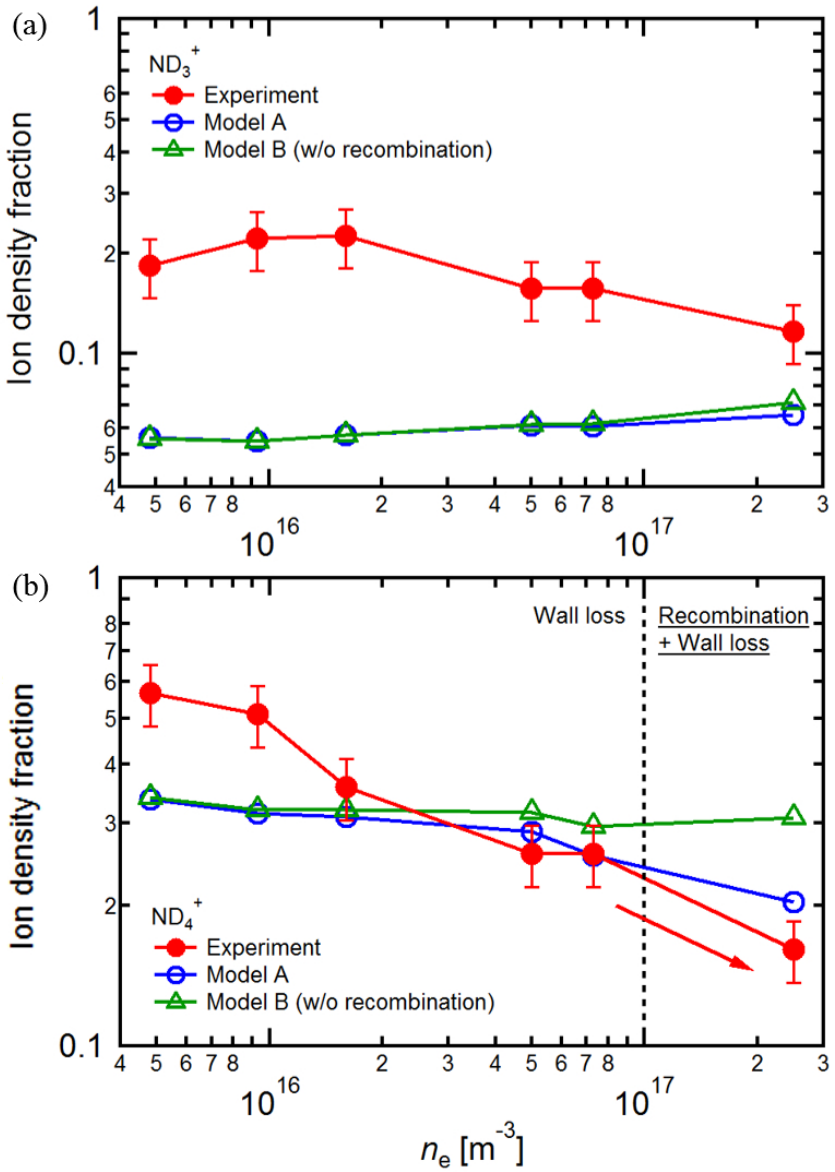

Figure 6.6: Ion density fraction of ND_3^+ and ND_4^+ in an electron density range $4 \times 10^{16} < n_e < 3 \times 10^{17}$. For ND_4^+, the experimental result well follows the calculation result in the case including the e-i recombination terms.

ions in the source legion do charge exchange with ND_3 and it forms ND_3^+ which may drift to the main reaction chamber ($Ar^+ + ND_3 \rightarrow Ar + ND_3^+$) (in Section 7.7.2). On the other hand, in high power discharge the ND_3 might be dissociated by high energy electron collisions in source region so our measurement could reflect reactions mainly in the main chamber region. While there is the discrepancy, the model calculation would still give us a hint of understanding formation process

of ND_3^+. Fig. 6.6(b) shows ND_4^+ ion density fractions from calculations and experiments. While both calculation shows similar results in $n_e < 10^{17}$ m^{-3}, model A becomes to show reduction to 20% when n_e becomes higher while model B calculation still shows 30% of concentration (constant for n_e). In low density range ($n_e < 10^{16}$ m^{-3}), model calculations show discrepancy with the model for a factor of 2. It can also be due to plentiful Ar^+ in the source region as well as ND_3^+ case. Ar^+ reacts with D_2 molecules via an ion exchange reaction $Ar^+ + D_2 \rightarrow ArD^+ + D$. Then, ND_4^+ would be formed $ArD^+ + ND_3 \rightarrow ND_4^+ + Ar$. This reaction also includes ND_3 which could be dissociated in high power discharges around source region. This can be why the model A well follows the experimental results in higher density region. Why can this reduction be observed when the electron density is increased? The answer can be suggested by examining its formation/destruction processes from the model calculation.

6.5.2 ND_3^+ formation/destruction process

Fig. 6.7(a) shows the production rates of ND_3^+ for the dominant reactions as estimated by model A. We find that the rates of these five formation reactions are in the same order. Fig. 6.7(b) shows the loss frequencies of ND_3^+ for dominant reactions. For the plasmas used here, the wall loss reaction rate is dominant in loss process and does not change much while the electron density is changes by a factor of 50 because the wall loss is assumed to be proportional to Bohm velocity $\sqrt{k_B T_e / m_i}$ where k_B is Boltzmann constant. The ion exchange reaction with ND_3 is also significant loss process for these low density plasmas which rates are about 25% of the wall loss rates. The rate of this reaction decreases as the ND_3 density decreases because T_g increases from 390 to 910 K as the discharge power input is increased. The e-i recombination rate increases with plasma density but it is still relevant with another loss reaction, ion exchange with ND_3, even in the high electron density plasma ($n_e = 2.5 \times 10^{17}$ m^{-3}). Those reactions having relevant production rates and loss frequencies make the quantitative prediction of ND_3^+ difficult.

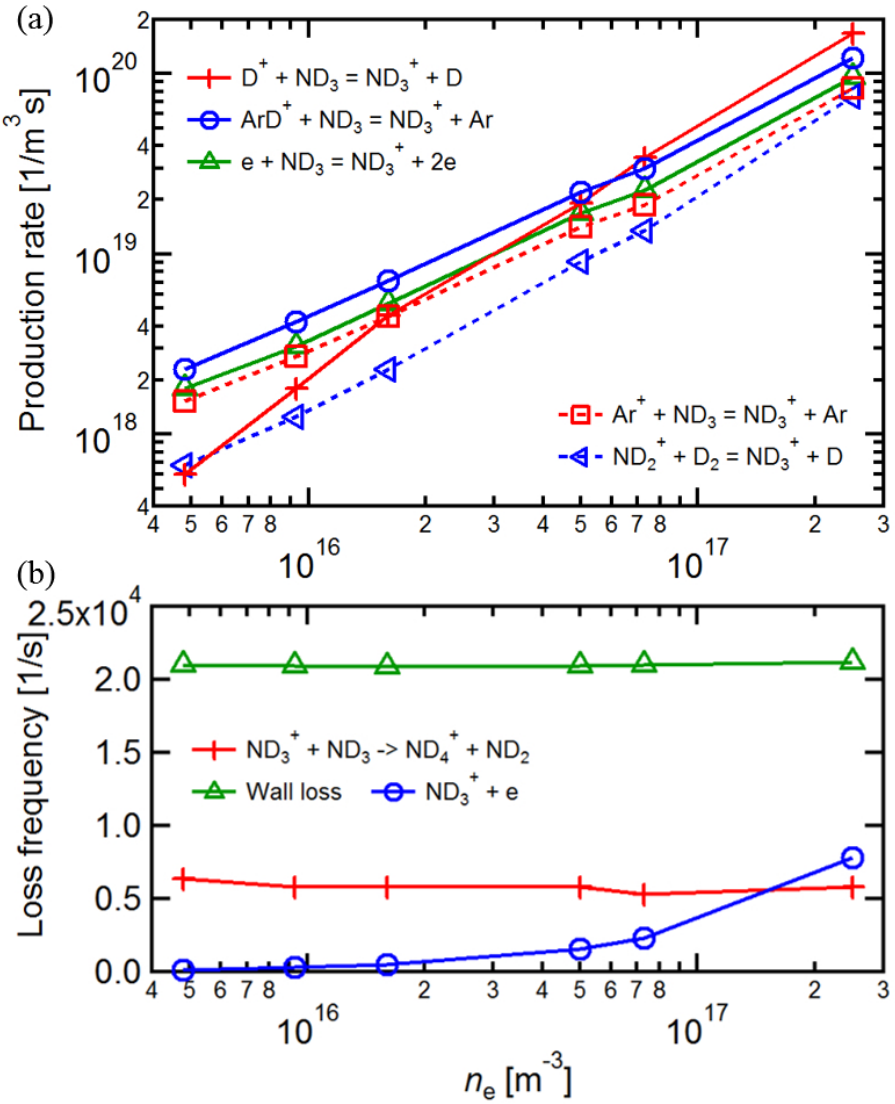

Figure 6.7: Production rates (a) and loss frequencies (b) of ND_3^+ estimated by the model A. Reactions which contributes less than 10% of the highest rate/frequency are excluded.

6.5.3 ND_4^+ formation/destruction process

Examining the results in fig. 6.6(b), we find that the predicted ND_4^+ density agrees with the measured value when HN-MAR is included in the model in $n_e > 10^{16}$ m^{-3}, while the model does not show good agreement when recombination is neglected; the largest discrepancy is seen in the highest density plasma which is when the volumetric recombination rate would be highest. Fig. 6.8(a) shows the production rates of ND_4^+ for dominant processes. The most dominant

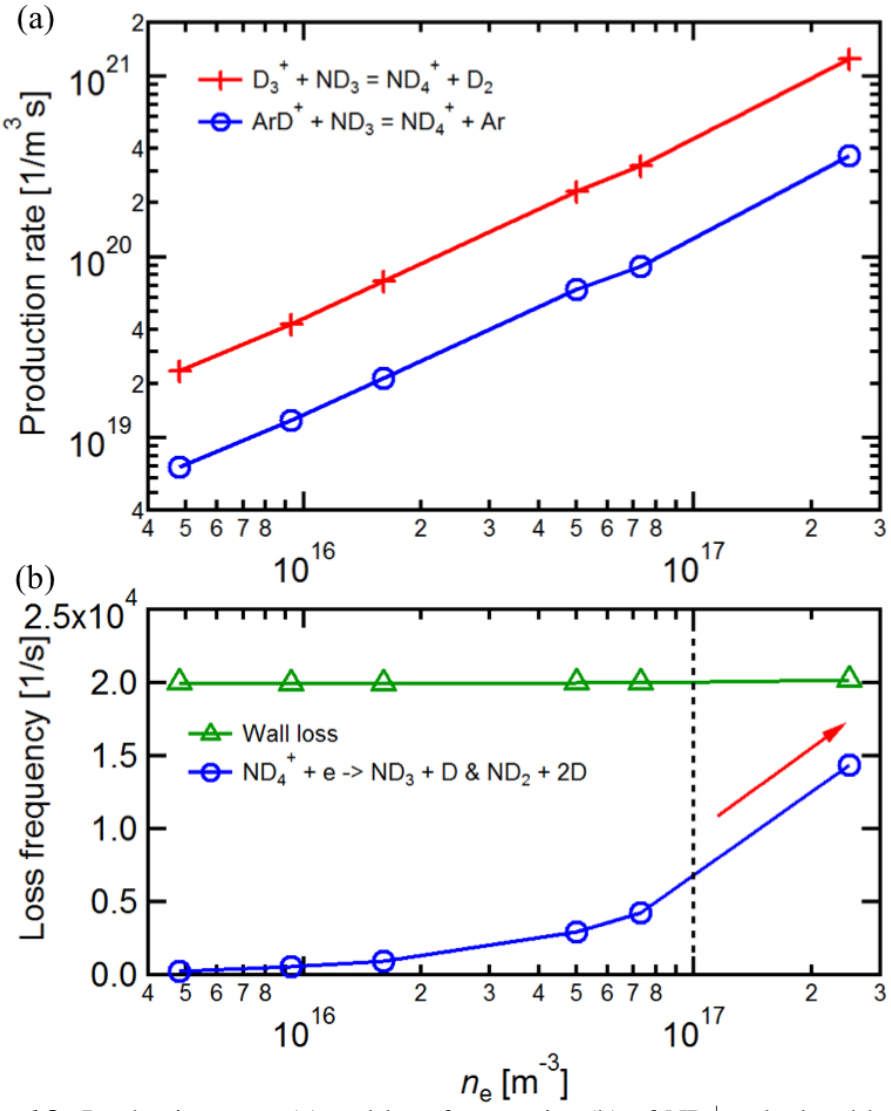

Figure 6.8: Production rates (a) and loss frequencies (b) of ND_4^+ calculated by the model. Reactions which contributes less than 10% of the highest rate/frequency are excluded. D_3^+ and ArD^+ are the dominant source species to form ND_4^+. The volumetric recombination term increases proportionally as a function of electron density while the wall loss rate is almost constant. Around $n_e \sim 2 \times 10^{17}$ m^{-3}, the recombination frequency becomes comparable to the wall loss.

formation process is the ion exchange reaction between D_3^+ and ND_3 which is the first step of HN-MAR (eq. (1.3)). The rate of the secondary formation process, the ion exchange between ArD^+ and ND_3, is 1/3 of the eq. (1.3) reaction. While the formation process of ND_3^+ includes many competing paths, the main formation scheme of ND_4^+ is relatively simple. Fig. 6.8(b) shows

the dominant loss process of ND_4^+. Though the wall loss reaction is the most effective loss process in lower density condition as well as ND_3^+, the recombination frequency, which is proportional to the electron density, becomes relevant to the wall loss rate around $n_e \sim 2 \times 10^{17}$ m^{-3}. Therefore, possible paths to form and destroy ND_4^+ are represented by only two source and two loss reactions. In the rate equation form we then have a balance given as

$$R^S_{IX(D_3^+)} + R^S_{IX(ArD^+)} = X^L_{wloss} + R^L_{DR} \tag{6.4}$$

where R^S_{IX}, X^L_{wloss}, and R^L_{DR} are the rate of the ion exchange reaction with ND_3, wall loss, and dissociative recombination, respectively. Here,

$$R^S_{IX(A^+)} = n_{A^+} n_{ND_3} k_{IX}(T_e). \tag{6.5}$$

The ion density fraction of a source species D_3^+ is shown in fig. 6.9(a) and follows the experimental results quantitatively and qualitatively in the electron density range, $n_e > 10^{16}$ m^{-3}. The experimental results show almost constant value $0.23 - 0.25$ varying within the error bar in $n_e > 10^{16}$ m^{-3} while calculation results showing constant value around 0.3. Fig. 6.9(b) shows the density fraction of ArD^+, the other source species of ND_4^+. Although the model prediction shows good agreement in $n_e > 5 \times 10^{16}$ m^{-3} with the experimental results. The discrepancy in the lower density range can be explained by the ion exchange reaction with ammonia in the source region (Sec. 6.5.1). ArD^+ can be dominant in the source region and form ND_4^+ immediately. It might explain why the measured ArD^+ concentration is an order smaller than prediction and ND_4^+ concentration is about twice of calculated value in the low power discharges $n_e < 10^{16}$ m^{-3}. While the plasma density increases from 5×10^{16} to 2.5×10^{17} m^{-3}, the experimental value increases from 0.21 to 0.34. Because the densities of those 2 source species show constant or increasing traits while the plasma density increases from 5×10^{16} to 2.5×10^{17} m^{-3} (fig. 6.9(a)), those source term cannot be the reason the observed ND_4^+ fraction decreases about half. ND_3

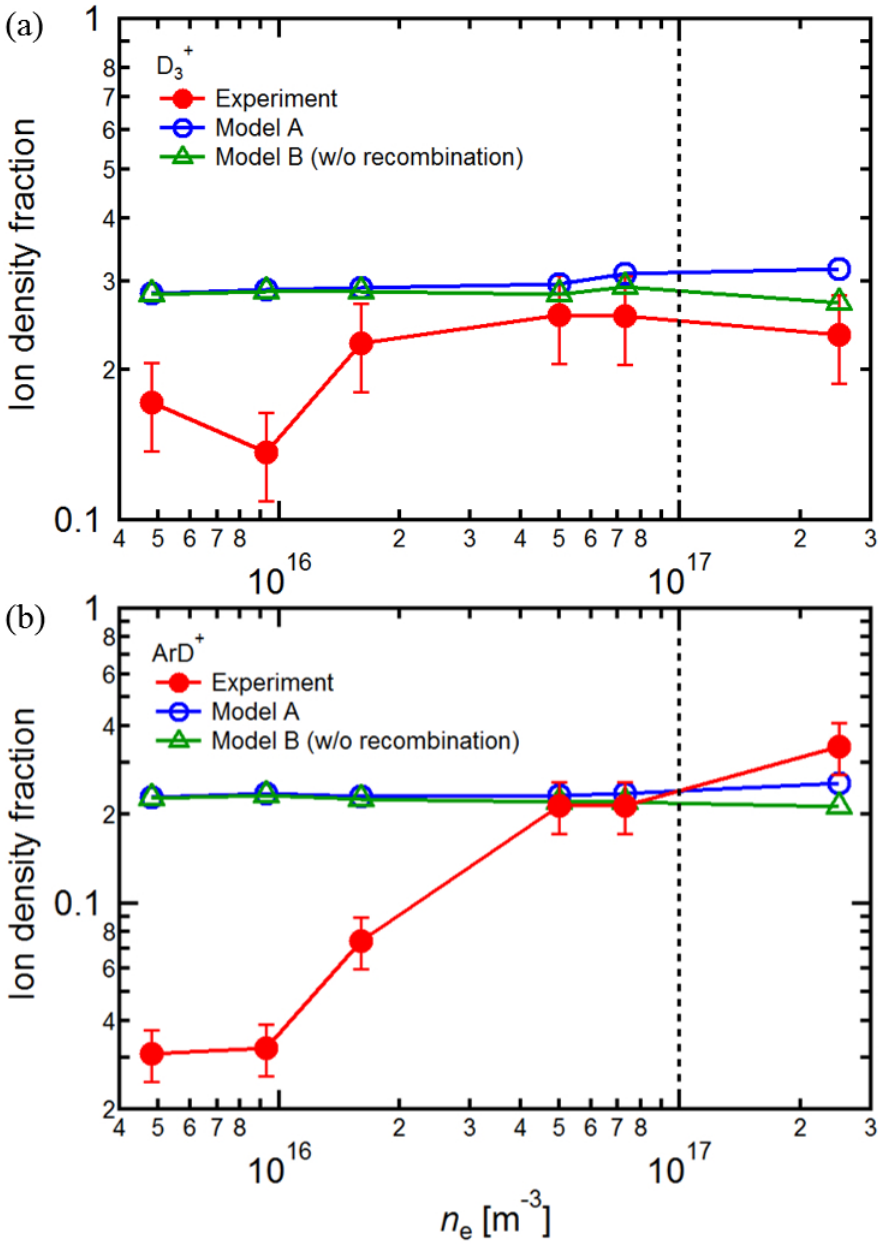

Figure 6.9: Ion density fractions of (a) D_3^+ and (b) ArD^+ which contribute to form ND_4^+ by the D^+ exchange reaction with ND_3. Both profiles show constant or slightly increasing trait as increasing n_e.

molecules react with those D_3^+ or ArD^+ ions to form ND_4^+ (eq. (6.5)) but, as fig. 6.4 showing, the ND_3 density is also independent of the electron density. The rate coefficients for these ion change exchange reactions vary as the electron temperature changes. Fig. 6.10 shows measured and calculated electron temperatures. The electron temperatures experimentally obtained do not

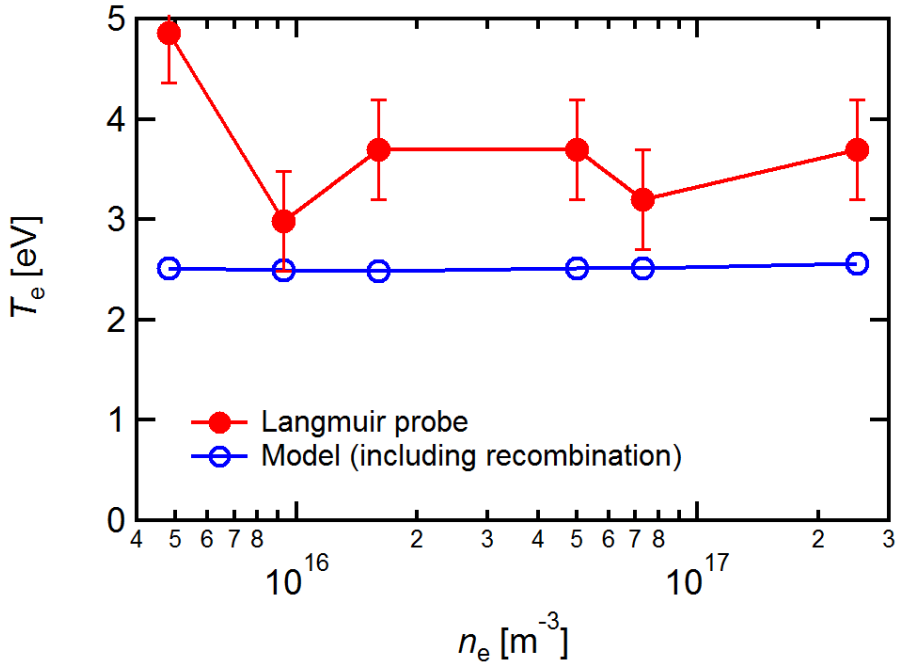

Figure 6.10: Measured and calculated electron temperatures as a function of the electron density. The error bar ± 0.5 eV of the electron temperature measured by the Langmuir probe is empirically obtained.

change much in $n_e > 10^{16}$ m^{-3} within the error bar. The calculated temperatures shows constant value $T_e \sim 2.5$ eV. On the other hand, according to the calculation shown in fig. 6.9(b), the dissociative recombination term makes the loss rates twice in the highest density plasma. This enhancement of the loss rate due to the recombination can be the plausible reason to make ND_4^+ fraction half as the electron density increases in fig. 6.6(b). Thus, those results strongly suggest the recombination process takes place in our plasmas.

6.6 Conclusion

In this chapter, the whole steps of HN-MAR process is examined by scanning the input RF power so that the electron density is scanned in the range $4 \times 10^{16} < n_e < 3 \times 10^{17}$ by feeding D_2, ND_3, and Ar. The ion fraction densities are measured by the calibrated EQP analyzer, and compared with the calculated fractions by the rate equation model. Two types of models

were then used and compared against the measured ion composition: the first included the volumetric electron-ion recombination terms, while the second did not include recombination terms. In the low density range, both models show similar results because the recombination reactions are negligible compared with the wall loss reaction at low density. For ND_4^+ which is an intermediate product of the HN-MAR process, however, the recombination frequency becomes comparable to the wall loss frequency at the highest electron density $n_e \sim 2 \times 10^{17}$ m^{-3} so that the calculation results from model B (without recombination terms) show discrepancy with experimental measurements. While the source species of ND_4^+ show constant fractions in high density range in the experiments, a drop in the ND_4^+ fractions is observed in the experiment as the plasma density is increased. It can be explained by existence of the dissociative recombination reaction $ND_4^+ + e^- \rightarrow ND_3 + D$ and $ND_2 + 2D$, whose rates become comparable with the wall loss rate in sufficiently high density plasma. The model calculation including the dissociative recombination terms reproduces the observed fractions within the expected uncertainties.

These results indicate that if the plasma density could be raised to sufficiently high values in our experiment, the loss frequency of the recombination terms should come to dominate the reaction kinetics and pronounced HN-MAR effects should occur. For example, when $n_e = 10^{18}$ m^{-3}, estimated loss frequency ratio of the recombination and wall loss $\nu_{DR}/\nu_{wloss} > 10$ so that the discrepancy between model A and B becomes large enough to clearly exceed the experimental errors. In the next chapter we present experimental results obtained in such high density plasmas up to 10^{18} m^{-3} , that were achieved by using the shorter chamber bucket. Those results are then compared against the global model predictions.

6.7 Acknowledgements

Chapter 6, including text and data, is in part a reprint of the material as it appears in S. Abe, S. Chakraborty Thakur, R.P. Doerner, G.R. Tynan, Hydronitrogen Molecular Assisted

Recombination (HN-MAR) processes in ammonia seeded deuterium plasmas, Journal of Nuclear Materials, submitted, (2018). The dissertation author was the primary investigator and author of this paper. This work was supported by the U.S. Department of Energy Grants No. DE-FG02-07ER54912.

Chapter 7

Dissociative recombination process of ammonium for HN-MAR process in high density D-N plasmas

7.1 Introduction

This chapter shows the results obtained by using a higher plasma density up to $n_e \sim 2 \times 10^{18}$ m^{-3} to investigate the volumetric recombination scheme of the HN-MAR for ITER relevant plasma detachment operation. Such high density plasmas can be realized by using a shorter chamber than one reported in Chapter 6 [3], which results in a higher volumetric power input into the discharge. Working at this higher plasma density allows us to clearly see the effects of the electron impact recombination reactions which becomes 20 times faster than the wall loss reaction in such high density region. The formation and destruction processes of the intermediate product of HN-MAR, namely ND_4^+, are investigated in plasmas formed in D-N-Ar mixtures. The ion density fractions measured by a calibrated electrostatic quadrupole plasma analyzer is compared with a rate equation model to obtain detailed chemical processes in the plasmas. Used

gases are D_2, N_2, and Ar while the flow rates are kept constant while the densities of the neutral gas species are measured by a residual gas analyzer. When the RF input power is scanned from $P_{RF} = 500 - 3300$ W, the plasma parameters vary from $n_e \sim 1 \times 10^{17} - 2 \times 10^{18}$ m^{-3}, $T_e \sim 3$ eV, and $T_g = 470 - 700$ K. An actinometry method using D and Ar emission lines gives the deuterium dissociation degree $n_D/(2n_{D_2} + n_D) = 1 - 5\%$. The results show that as the plasma density is increased to these larger values the ND_4^+ density fraction undergoes a drastic decrease from 0.55 to 0.11, in good agreement with the 0-d chemical kinetics model. Because of the existence of other significant reaction pathways, however, similar studies of the ND_3^+ concentration do not provide clear evidence for dissociative recombination processes mediated by that species. These results provide evidence and importance of the dissociative recombination reactions of ammonium (ND_4^+) ion in the HN-MAR process. The results of our other work together with these new results suggest that directly injecting ammonia into the divertor plasma instead of nitrogen might achieve plasma detachment with a lower rate of molecular gas injection.

7.2 Description of Experiment

For the experiments reported in this chapter, the anodized aluminum reaction chamber 350 mm diameter and 300 mm high is used while the chamber used in previous chapters 5-6 [1][3] had a height of 400 mm. This short chamber helps to make the distance between the source and sampling orifice closer, so that the high plasma density in the sampling region can be realized. The input power is varied from 500 to 3300 W in this experiment while the reflected power is less than 1% of input power. The incoming gas flow rates of D_2, N_2, and Ar are kept constant by mass flow controllers. Ar is injected to realize the high density plasmas up to $n_e \sim 10^{18}$ m^{-3} as well as the experiment in Chapter 6 while the maximum density for D-N mixtures is $n_e \sim 5 \times 10^{17}$ m^{-3}. Partial pressures of each gas species during plasma OFF phase are $p_{D_2} = 8.6$ mTorr, $p_{N_2} = 1.0$ mTorr, $p_{Ar} = 1.3$ mTorr. Operating the top coils with the current

20 A and the bottom coils with 120 A creates a magnetic field of 15 gauss at the center of the bell-jar, and about 40 gauss at the entrance orifice of the Electrostatic Quadrupole Plasma (EQP) analyzer.

7.3 Rate equation model

The model used in this chapter is almost identical with one used in previous chapters 5-6 [1][3], the only difference being that we have included the charge exchange reaction,

$$H_2 + H^+ \rightarrow H_2^+ + H \tag{7.1}$$

which was ignored in the model because it was assumed to be cancelled out by its inverse reaction,

$$H_2^+ + H \rightarrow H_2 + H^+ \tag{7.2}$$

However, the model of Hollmann [40] showed the rate of the exchange reaction, which is the initiation step of the H-MAR process, may not be negligible for some plasma conditions of interest. The cross-section data is taken form the collisional-radiative atomic-molecular database (CRAMD) code [84] as well as the model of Hollmann *et al.* [40] while the vibrational temperature of H_2 is assumed as $T_{\mathrm{vib}} = 3000$ K.

7.4 Parameter measurements

7.4.1 Radial plasma profiles

Fig. 7.1 shows a radial profile of electron density n_{e} of 500, 1500, and 3300 W plasma at $z = 78$ mm. It is seen that parameters drop for $r > 75 - 100$ mm. The particle loss to the

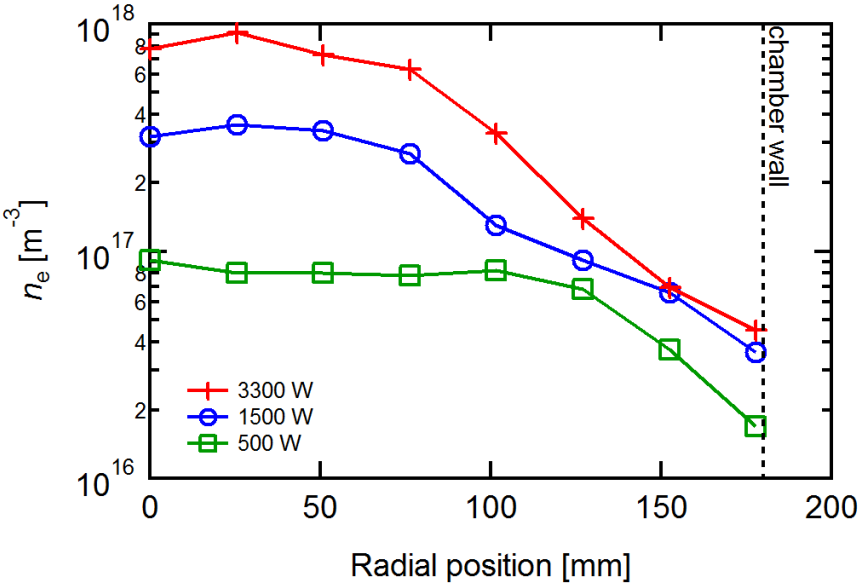

Figure 7.1: Radial profile of plasma parameters n_e of $P_{input} = 500, 1500, and 3300\ W$ plasma at $z = 78$ mm. The parameters drop for $r > 75 - 100$ mm, and n_e around chamber wall becomes $6 - 20\%$ of the centeral location parameters.

chamber wall is volume averaged while the model predicts species densities in the plasma center while measurements are performed. The effective wall loss rate $X^i_{loss} = n_{b,i}\nu_{wi}$ is used in the equations [1] as well as Chapter 6 experiment (Sec. 6.4.1). In fig. 7.1, the ratio of the plasma densities at the center and edge changes $n_{b,e}/n_{c,e} = 20 - 6\%$ while $P_{RF} = 500 - 3300$ W, respectively.

7.4.2 Density of neutral gasses

Fig. 7.2 shows the measured density of D_2, D, N_2, ND_3, and Ar for various plasma electron densities. The D density is measured by the actinometry method [3]. The densities of other species are measured by the calibrated RGA. The density of ND_3 and N_2 is not strongly dependent on the input power, i.e. plasma density. On the other hand, the density of D depends on input power, i.e. the dissociation degree, $n_D/(2n_{D_2} + n_D) = 1 - 5\%$ while input power increases from 500 to 3300 W, respectively. Those measured neutral gas densities are used as input parameters in the rate equation.

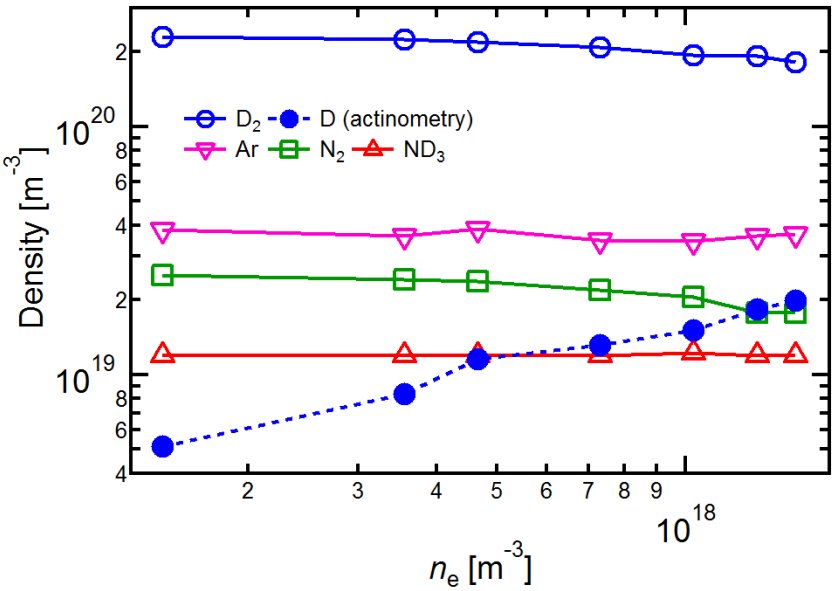

Figure 7.2: Density of neutral gas species measured by a calibrated RGA and actinometry during plasma ON phase as a function of the electron density.

7.5 Ion concentration and formation/destruction processes

7.5.1 Ion concentration of ammonium ND_4^+

Fig. 7.3 shows the ion density fractions of ammonium ND_4^+, which is an intermediate product of the HN-MAR, as a function of the electron density. The experiments show a drastic (factor of ~ 5) reduction in ND_4^+ concentration as the plasma density is increased to its highest value. The question then arises: what changes occur in the discharge chemical kinetics to cause this result? To begin to address this question, two types of model calculation results are also shown in fig. 7.3. The first comprehends the electron-ion recombination processes including the DR reactions shown in eqs. 4.6 and 4.7 (denoted here as model A), while the second neglects these recombination terms (denoted here as model B). The discrepancy between model A and B is obvious especially in the high plasma density range. In the highest density plasma [$n_e = 1.5 \times 10^{18}$ m^{-3}], model A predicts the ion density fraction $f_{A,ND_4^+} = 0.17$, close to the

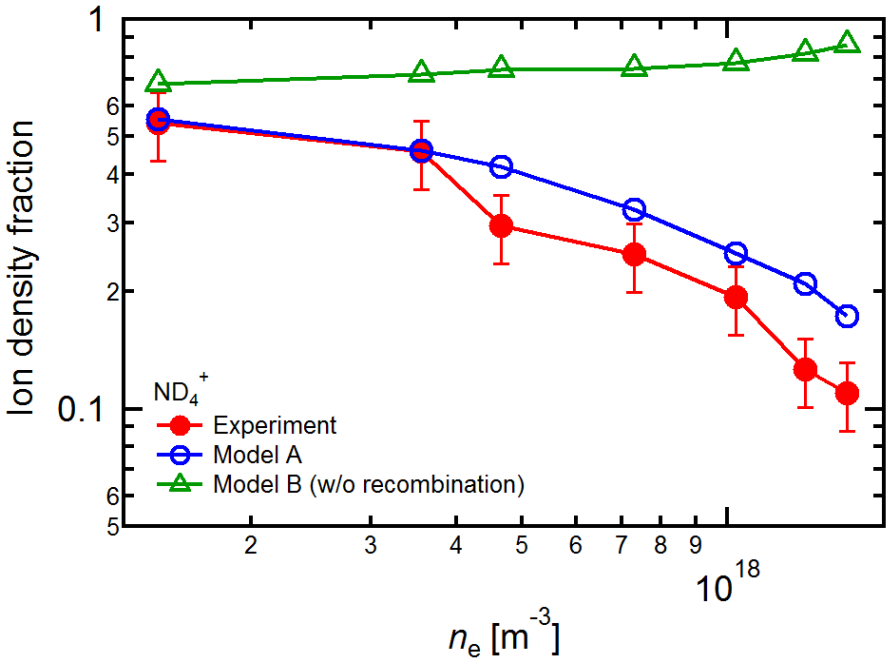

Figure 7.3: Ion density fraction of ND_4^+ in an electron density range $1 \times 10^{17} < n_e < 2 \times 10^{18}$. The experimental result well follows the calculation result in the case including the dissociative recombination terms.

observed value, while model B predicts $f_{B,ND_4^+} = 0.86$ (mostly dominated by ND_4^+). On the other hand, the experimental result follows the model A prediction well both qualitatively and quantitatively even though model A predicts about 50% higher fraction than the experiment in a range [$n_e > 4 \times 10^{17}$ m^{-3}]. These results suggest that volumetric DR processes begin to play a significant role in the equilibrium density of the ND_4^+ species.

7.5.2 Formation/destruction process of ammonium ND_4^+

To explore the origin of the results in fig. 7.4 we examine the production and loss rates for the relevant reactions. Fig. 7.4(a) shows the computed production rates of ND_4^+ for the dominant formation processes. The dominant formation process is the ion exchange reaction between D_3^+ and ND_3 which is the first step of HN-MAR (eq. (4.3)). The rate of the secondary formation process, namely D^+ ion exchange between ND_3^+ and ND_3, is about half of the primary reaction. Another ion exchange reaction of ND_3 with N_2D^+ also contribute to form ND_4^+. Though ArD^+

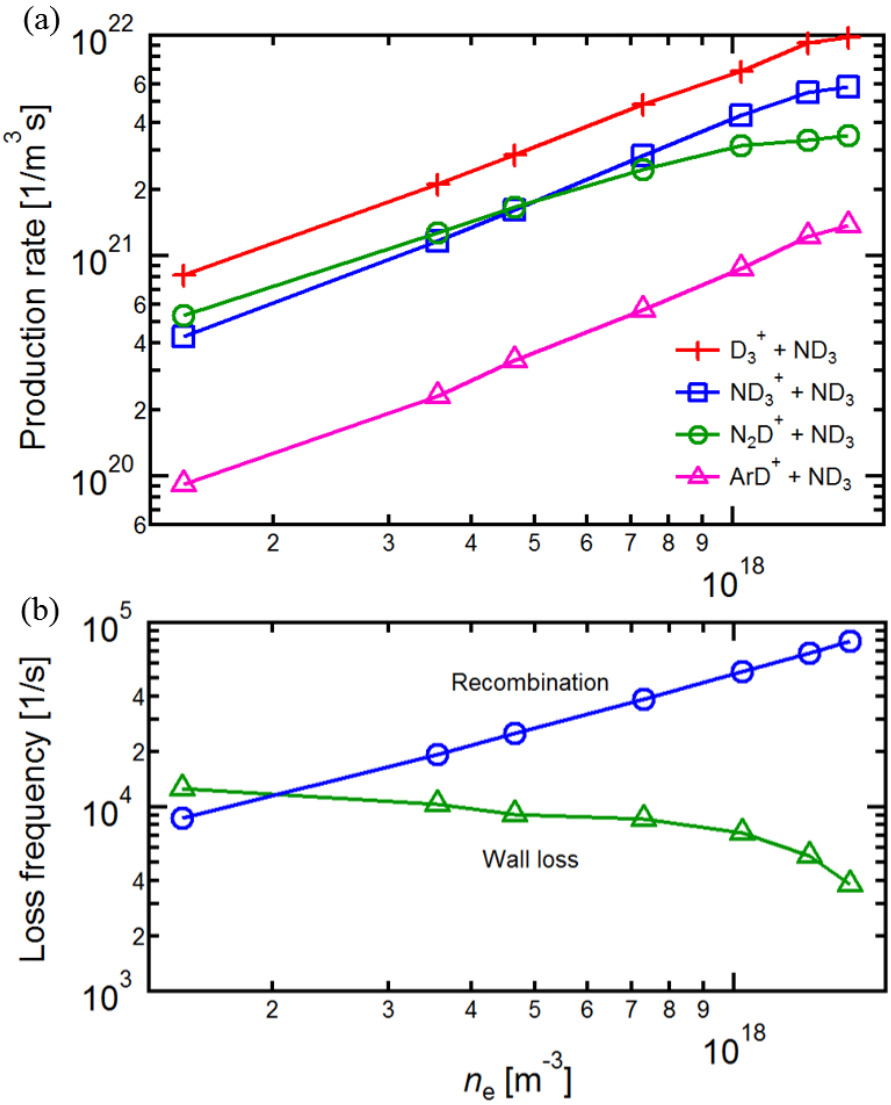

Figure 7.4: Production rates (a) and loss frequencies (b) of ND_4^+ calculated by the model A. Reactions which contributes less than 10% of the highest rate/frequency are excluded. D_3^+, ND_3^+, and N_2D^+ are the dominant source species to form ND_4^+. The volumetric recombination term increases proportionally as a function of electron density while the effective wall loss rate decreases.

also forms ND_4^+ by ion exchange, its contribution is estimated to be an order-of-magnitude smaller than the dominant D_3^+ formation pathway. Therefore, Ar present in the plasma, it does not appear to significantly affect the plasma molecular kinetics of ND_4^+. Fig. 7.4(b) shows the dominant loss processes of ND_4^+. The recombination frequency is proportional to the electron density while the effective wall loss decreases due to decreasing of $n_{b,e}/n_{c,e}$. Thus, at the highest

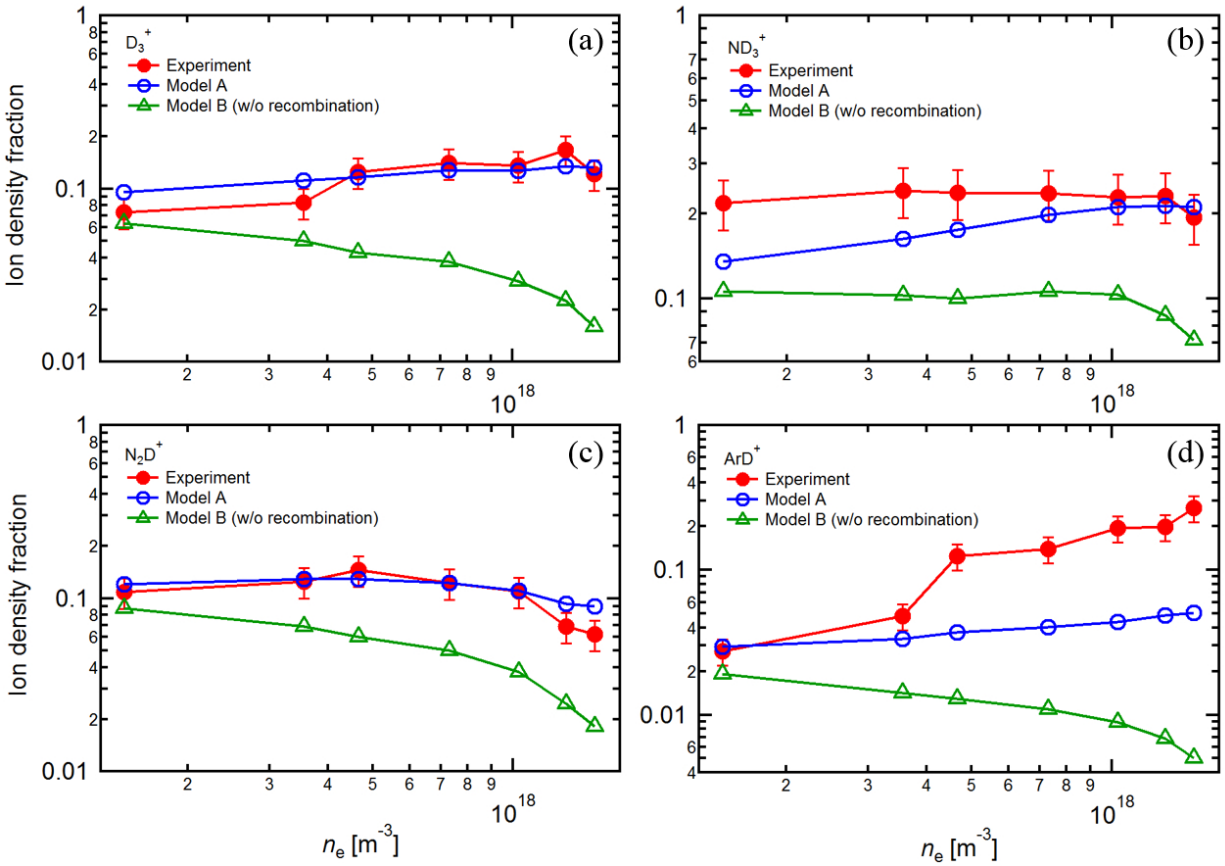

Figure 7.5: Ion density fractions of species dominantly forming ND_4^+ due to ion exchange reaction with ND_3. Experimental results show agreement with model calculation (w/ recombination terms) especially in the high density range. [2]

density achieved in our experiment the estimated recombination rate is about 20 times larger than the wall loss rate and can begin to dominate the ND_4^+ losses.

Using these dominant production and loss processes we then have a rate balance given as

$$R^{\mathrm{S}}_{\mathrm{IX}(D_3^+)} + R^{\mathrm{S}}_{\mathrm{IX}(ND_3^+)} + R^{\mathrm{S}}_{\mathrm{IX}(N_2D^+)} + R^{\mathrm{S}}_{\mathrm{IX}(ArD^+)} = X^{\mathrm{L}}_{\mathrm{wloss}} + R^{\mathrm{L}}_{\mathrm{DR}} \tag{7.3}$$

where $R^{\mathrm{S}}_{\mathrm{IX}}$, $X^{\mathrm{L}}_{\mathrm{wloss}}$, and $R^{\mathrm{L}}_{\mathrm{DR}}$ are the rate of the ion exchange reaction with ND_3, wall loss, and dissociative recombination, respectively, and described by equations $k2.15, 2.35, 2.38, 2.41$, eq. (2.14), and $k3.10-11$ in Chapter 2. The measured and predicted ion density fractions of the 4 ion species that dominate the production of ND_4^+ are shown in fig. 7.5. Fig. 7.5(a) and

(c) show the D_3^+ and N_2D^+ fractions from experiment and calculations. At higher densities when DR processes dominate wall losses, the predictions for these concentrations by model A agree with experimental results within the error bar. In fig. 7.5(b) for ND_3^+, model A follows the experimental result in the high density range $n_e > 5 \times 10^{17}$ m^{-3}. In fig. 7.5(d) for ArD^+, while the experimental results show about 4 times larger fraction than the model A prediction for $n_e > 5 \times 10^{17}$ m^{-3}, model A reproduces the slightly increasing concentration with increasing electron density. We note that model B predictions, which neglect the DR loss processes, never follow experimental results quantitatively and qualitatively for any of the species shown in fig. 7.5; this discrepancy increases with higher density plasmas. The results shown in fig. 7.5 indicate that the underlying ion density fraction of the ND_4^+ precursors experiences very little change across the range of plasma electron densities studied in these experiments. Thus, the large change in ND_4^+concentration as the plasma density is increased seen in fig. 7.3 must be due to some other mechanisms.

In principle the reaction rates could also change as the plasma electron density is changed. As mentioned in Chapter 2, the rate coefficients k_{ij} are a function of electron temperature and thus changes there could also perhaps be responsible; however measured and calculated electron temperatures (fig. 7.6) show almost constant across the whole electron density range. Therefore, the rate coefficients do not change much while the input power and plasma electron density changes. Thus one cannot explain the large changes in ND_4^+ concentration by appealing to a change in reaction rates. The only process then left is the sink terms. Fig. 7.4(b) shows the dissociative recombination term is the dominant sink term in this experimental configuration [$n_e > 10^{17}$ m^{-3}]. Furthermore, we note that the total loss rate (which will be given by the sum of the recombination and wall losses) increases by $\sim 4\times$ for the reported density range shown here. This enhancement of the loss rate due to the recombination can be a plausible reason to decrease ammonium ND_4^+ fraction drastically as the electron density increases. These losses then allow model A to do a reasonably job of explaining the neutral and ionized molecular

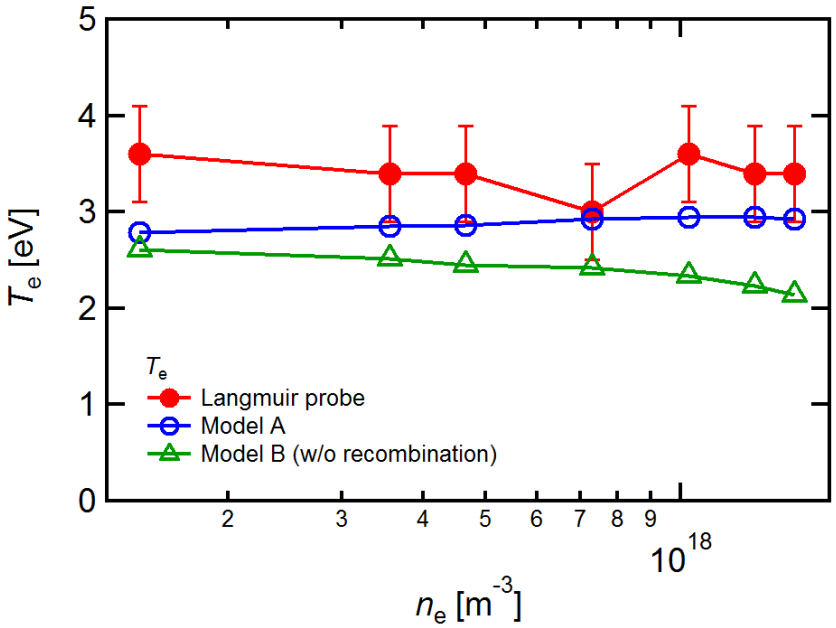

Figure 7.6: Measured and calculated electron temperatures as a function of the electron density. The error bar ± 0.5 eV of the electron temperature measured by the Langmuir probe is empirically obtained. Both measured and calculated temperatures do not change much in the whole electron density range.

concentrations for the range of conditions explored here, and provide strong evidence that the HN-MAR recombination processes are taking place in our plasmas.

7.6 Conclusion

In this chapter, we studied the HN-MAR process by scanning the input RF power so that the electron density is scanned in the range $1 \times 10^{17} < n_e < 2 \times 10^{18}$ by feeding D_2, N_2, and Ar. The ion fraction densities are measured by the calibrated EQP analyzer, and compared with the calculated fractions by the rate equation model. The two types of model are used: the first includes the volumetric electron-ion recombination terms, and the second does not include these recombination terms. For the ammonium ND_4^+ which is an intermediate product of the HN-MAR process, as the electron density increases, the model including the recombination effects well follows experiments. The density fractions of source species forming ND_4^+ are almost constant

or show negligible changes, while the ND_4^+ fraction drops from 0.55 to 0.11 as the electron density increases. This drastical reduction of ND_4^+ can only be explained by the enhancement of the recombination rate that proportionally increases as a function of the electron density. The model calculation including the dissociative recombination terms also reproduces the observed molecular ion fractions. Thus, this result clearly shows the importance of the recombination reactions in such a high density plasmas to complete the HN-MAR process.

7.7 Appendix: Calculation results of secondary HN-MAR reactions

In this appendix section, slower (or secondary) reactions of the HN-MAR process in the plasmas are investigated and summarized by using the model calculations.

7.7.1 D_3^+ neutralization process supported by ammonia

Fig. 7.7 shows the HN-MAR reaction (eq. (4.3)) as the dominant reaction to deconstruct D_3^+ while the electron impact recombination reaction becomes comparable in high density plasmas. The secondary loss process is the ion exchange reaction with nitrogen showing about half of the HN-MAR reaction rate. Although in our nitrogen seeded plasmas the density of N_2 is about twice of ND_3 (fig. 7.2), the HN-MAR reaction shows higher loss rate than the reaction related to nitrogen molecules. Therefore, we suggest the recombination efficiency can be enhanced by increasing ND_3 density rather than N_2 in fusion devices. It can be achieved by puffing ammonia directly instead of nitrogen as proposed in previous reports [1][3].

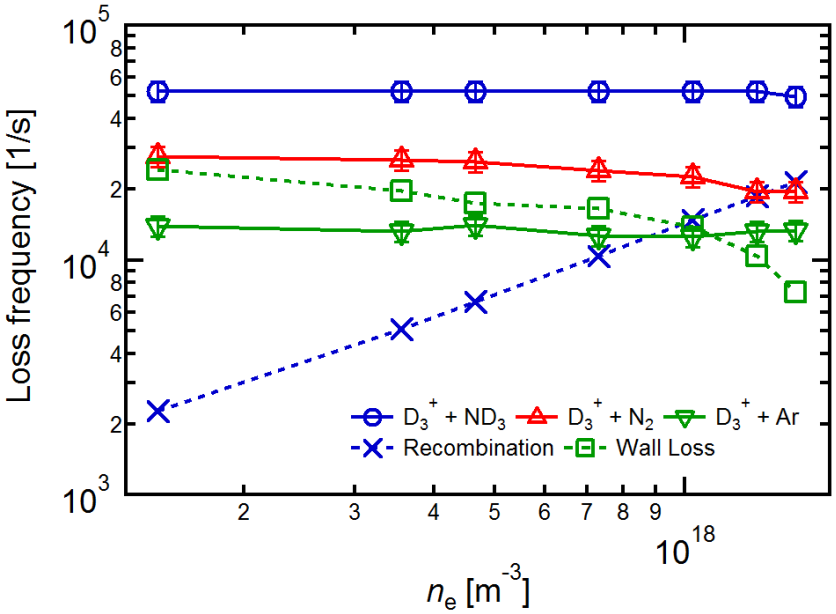

Figure 7.7: Loss frequencies of D_3^+ as the function of the electron density. Error bars correspond to rate coefficient measurements.

7.7.2 HN-MAR process in regard to ND_3^+

In fig. 7.8(a), the calculated formation rates of ammonia ion ND_3^+, which is the other intermediate product of HN-MAR, are shown. The figure shows that the charge exchange reaction D^+ and ND_3, which is the first step of HN-MAR (eq. (4.1)), becomes the dominant reactions in the highest density plasma, while the direct electron impact ionization is the dominant source of ND_3^+ in an electron density range [$n_e > 10^{18}$ m^{-3}]. It has to be noted that the figure shows the rates of 6 source reactions, which are all of the same order, making it difficult to identify the dominant formation/destruction process of ND_3^+ with the experimental method performed in the ND_4^+ case (Sec. 7.5.2). Although fig. 7.8(a) shows that a complex formation process, it may also help explain the discrepancy of the model A prediction of ND_3^+ ion concentration in a low electron density range [$n_e < 5 \times 10^{17}$ m^{-3}] (fig. 7.5(b)). As also discussed in Section 6.5.1, in the source region around the bell-jar, the plasma may be dominated by Ar^+ because of the low ionization energy of Ar. Ar^+ ion could then form ND_3^+ through the reaction $Ar^+ + ND_3 \rightarrow Ar + ND_3^+$ (shown in fig. 7.5(a)) in the source region; the resulting ND_3^+ ion would drift into the downstream reaction

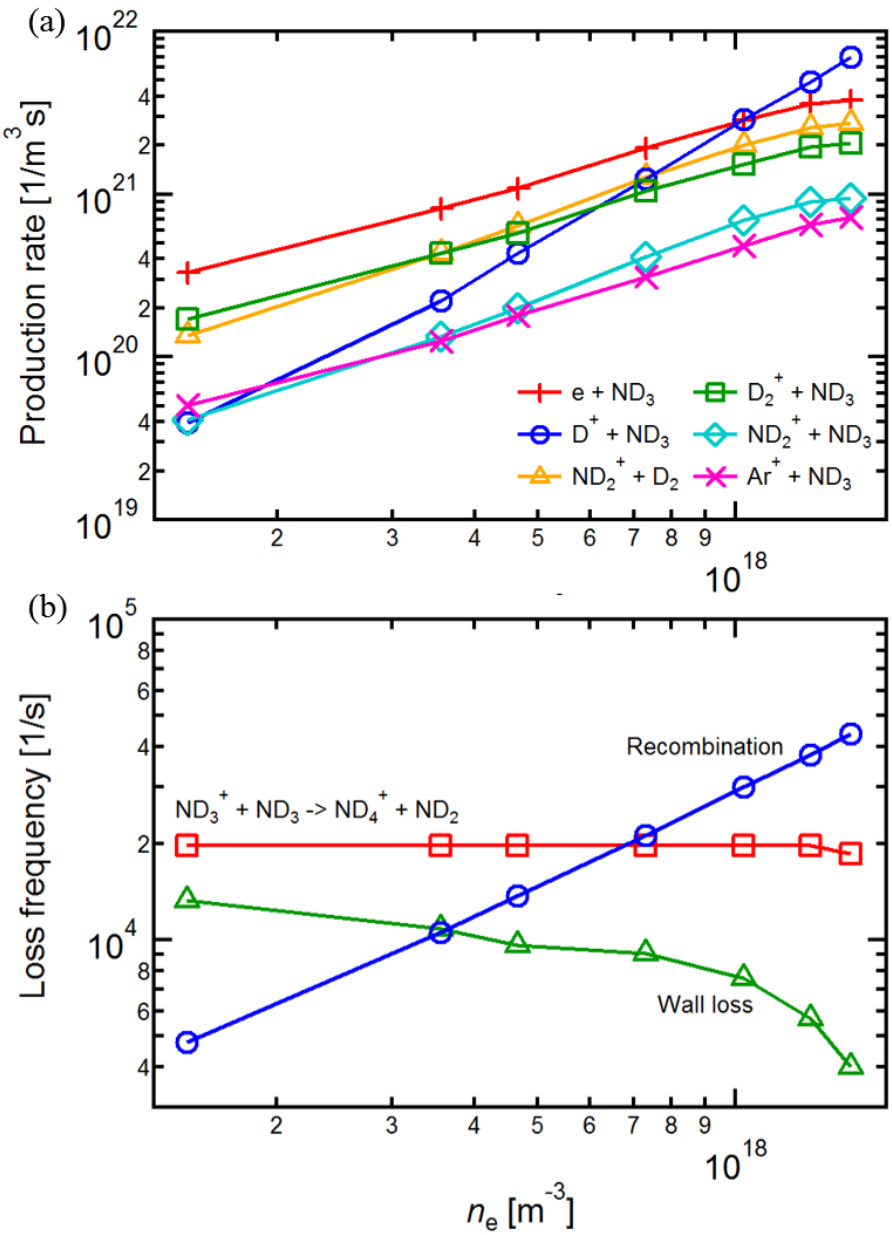

Figure 7.8: Production rates (a) and loss frequencies (b) of ND_3^+ calculated by the model A. Reactions which contributes less than 10% of the highest rate/frequency are excluded.

chamber. That could be the reason why the measurement shows about two times higher density than the model A calculations. On the other hand, in the higher density [$n_e > 5 \times 10^{17}$ m^{-3}] i.e. high power discharges, the electron temperature in the source region could be high enough to directly dissociate a portion of the incoming ammonia formed in the main reaction chamber.

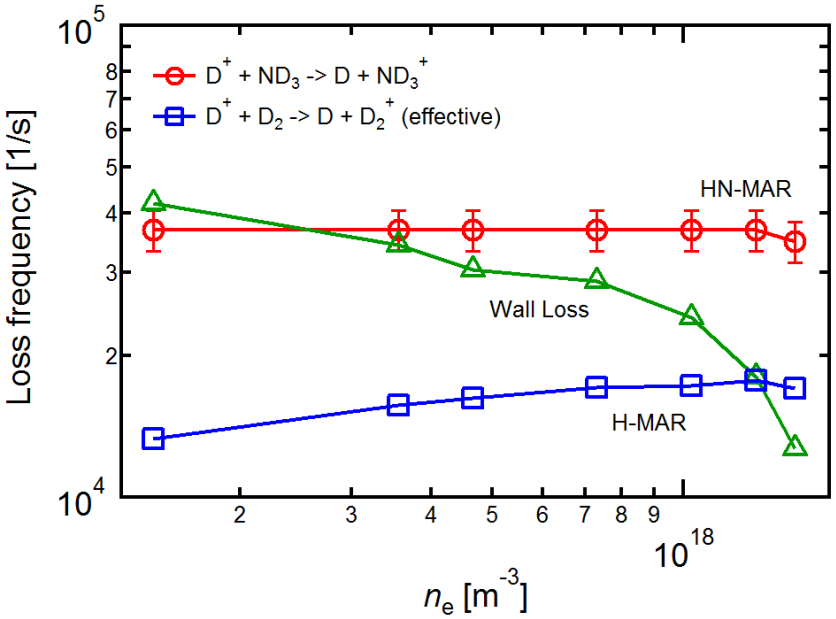

Figure 7.9: Loss frequencies of D^+ calculated by the model A. It suggests that HN-MAR reaction (eq. (4.1)) is about 2 times more efficient the H-MAR process in our plasmas. Error bars correspond to rate coefficient measurements.

This would then allow better agreement between the measured ND_3^+ density and the model A calculation for the high density plasmas [$n_e < 10^{18}$ m^{-3}] because ND_3^+ would mainly be formed by reactions in the chamber where we perform measurements. However, these mechanisms also rely upon spatially dependent effects and thus inherently are not included in our global (i.e. 0-d) model which assumes uniform kinetics throughout the system.

Fig. 7.8(b) shows the direct electron impact recombination, which is the HN-MAR step 2 process (eqs. (4.4) and (4.4)), that becomes the main loss channel of ND_3^+ in the density range [$n_e > 10^{18}$ m^{-3}]. The ion exchange reaction with ammonia is the other significant loss mechanism of ND_3^+. This reaction forms ND_4^+, which is subsequently lost by the dissociative recombination reaction of the HN-MAR process (fig. 7.4). Fig. 7.9 shows taht one of the dominant loss reactions of D^+ is the charge exchange with ND_3, which is the HN-MAR step 1 reaction (eq. (4.1)). The wall loss is also shown as the other primary D^+ loss reaction in a range [$n_e < 10^{18}$ m^{-3}]. The figure also shows the effective rate of the first step of the H-MAR process (eq. (7.1)). The effective rate means that the rate of inverse reaction (eq. (7.2)) is subtracted from the rate of eq. (7.1)

reaction. We can see the HN-MAR rates is about 2 times higher than H-MAR rates while the presence of ammonia is only 5% of deuterium in those experiments. Thus, also in this case as well as Sec. 7.7.1, it can be suggested that puffing the ammonia gas directly into the divertor plasmas to increase its density can enhance the recombination of the hydrogen ions.

7.8 Acknowledgements

Chapter 7, including text and data, is in part a reprint of the material as it appears in S. Abe, S. Chakraborty Thakur, R.P. Doerner, G.R. Tynan, Electron impact recombination process of ammonium for HN-MAR process in high density D-N plasmas, Physics of Plasmas, submitted (2018). The dissertation author was the primary investigator and author of this paper. This work was supported by the U.S. Department of Energy Grants No. DE-FG02-07ER54912.

Chapter 8

Conclusions and Future Work

8.1 Conclusion and summary

The experiments presented here shows understanding and a proposal of the new recombination process of hydrogen ions assisted by the ammonia molecules. The key results from this thesis are narrated below.

- We proposed a new recombination scheme of hydrogen ions supported by ammonia molecules, called Hydronitrogen Molecular Assisted Recombination [HN-MAR].
- We demonstrated HN-MAR process in D-N plasmas as dominant reactions by showing results below.

– Ammonia formation was observed by RGA measurement in the D-N plasmas.

– The ion density fractions were calculated by the rate equation model (global model), and showed good agreement with experimentally measured ion density fractions for dominant ion species.

– The model explained that CX/IX reactions of HN-MAR produce ND_3^+ and ND_4^+ as dominant ion species in D-N plasma (low electron density $n_e \sim 10^{16}$ m^{-3}).

– The drastic reduction of ND_4^+ density was observed experimentally when the electron density was increased from 10^{17} to 10^{18} m^{-3} due to dissociative recombination reactions in the volume [HN-MAR step 2] dominating the wall losses.

According to those results, we would like to conclude that there is the Hydronitrogen-enhanced Molecular Assisted Recombination [HN-MAR] process as dominant reactions in D-N plasmas and it drastically increases the recombination rate of the hydrogen plasmas. The HN-MAR process found in this thesis will be enhanced by increasing ammonia molecules in the volume. Therefore, to increase the ammonia density the direct injection of ammonia instead of nitrogen gas can be proposed.

To apply the HN-MAR process to actual tokamak divertor system, here some future research plans are suggested.

- Modifiying the global model to take spatial dependence into account (1D) or integrating HN-MAR reactions into 2D multi-fluid simulation code such as SOLPS-ITER.

- HN-MAR can also be induced for recombination of helium plasma. In that case, the first step can be $He^+ + NH_3 \rightarrow He + NH_{3-x}^+ + H_{x=0-2}$. Those reactions are already integrated in the global model used in this thesis. The similar experiment demonstrated in this thesis can be applied.

- Plasma detachment simulation using a linear plasma divertor simulator (ex. CSDX [UCSD]) with actual impurity gas puffing of several gas species such as NH_3/N_2/Ar/H_2/Ne to the hydrogen plasma in downstream region, can be a strong option.

- Although the ammonia was observed by RGA in our system, here is still a question: For which parameter range can ammonia survive in the divertor plasma without decomposition? In a high electron/gas temperature and high density plasma, the ammonia could be directly dissociated by the electron impact. To certify the existence of ammonia in a part of plasma,

the spectroscopy method would be useful instead of RGA measurement. Laser-induced fluorescence (LIF) measurement can be used for the measurement. Ammonia's resonance bands exist in a range $170 - 215$ nm [39].

Bibliography

[1] S. Abe, R. P. Doerner, and G. R. Tynan. Neutralization processes of atomic/molecular deuterium ions assisted by ND_3 in low density D_2-N_2 plasmas. Physics of Plasmas, 25(7):073507, 2018.

[2] S. Abe, S. Chakraborty Thakur, R. P. Doerner, and G. R. Tynan. Dissociative recombination process of ammonium for HN-MAR process in high density D-N plasmas. Physics of Plasmas, 2018. accepted.

[3] S. Abe, S. Chakraborty Thakur, R. P. Doerner, and G. R. Tynan. Hydronitrogen Molecular Assisted Recombination (HN-MAR) processes in ammonia seeded deuterium plasmas. Journal of Nuclear Materials, 2018. submitted.

[4] Daniel Alegre, Jose A. Ferreira, and Francisco L. Tabarés. Surface effects on the diagnostic of carbon/nitrogen low-pressure plasmas studied by differentially pumped mass spectrometry. Journal of Mass Spectrometry, 49(5):342–352, 2014.

[5] T. Amano. The dissociative recombination rate coefficients of H_3^+, HN_2^+, and HCO^+. The Journal of Chemical Physics, 92(11):6492–6501, 1990.

[6] Vincent G. Anicich. Evaluated bimolecular ionmolecule gas phase kinetics of positive ions for use in modeling planetary atmospheres, cometary comae, and interstellar clouds. Journal of Physical and Chemical Reference Data, 22(6):1469–1569, 1993.

[7] Vincent G. Anicich. An index of the literature for bimolecular gas phase cation-molecule reaction kinetics. JPL Publication, 19, 01 2003.

[8] Ramesh A. Arakoni, Ananth N. Bhoj, and Mark J. Kushner. H_2 generation in Ar/NH_3 microdischarges. Journal of Physics D: Applied Physics, 40(8):2476, 2007.

[9] P. B. Armentrout. Fundamentals of ionmolecule chemistry. J. Anal. At. Spectrom., 19:571–580, 2004.

[10] S. A. Astashkevich, M. Käning, E. Käning, N. V. Kokina, B. P. Lavrov, A. Ohl, and J. Röpcke. Radiative characteristics of $3p\Sigma$, Π; $3d\Pi^-$, Δ^- states of H_2 and determination of gas temperature of low pressure hydrogen containing plasmas. J. Quantum Spectrosc. Radiat. Transfer, 56:725, 1996.

[11] D. Barton, D. J. Heason, R. D. Short, and J. W. Bradley. The measurement and control of the ion energy distribution function at a surface in an RF plasma. Measurement Science and Technology, 11(12):1726, 2000.

[12] M. Bernert, M. Wischmeier, A. Huber, F. Reimold, B. Lipschultz, C. Lowry, S. Brezinsek, R. Dux, T. Eich, A. Kallenbach, A. Lebschy, C. Maggi, R. McDermott, T. Pütterich, and S. Wiesen. Power exhaust by SOL and pedestal radiation at ASDEX upgrade and JET. Nuclear Materials and Energy, 12:111 – 118, 2017. Proceedings of the 22nd International Conference on Plasma Surface Interactions 2016, 22nd PSI.

[13] M. N. A. Beurskens, J. Schweinzer, C. Angioni, A. Burckhart, C. D. Challis, I. Chapman, R. Fischer, J. Flanagan, L. Frassinetti, C. Giroud, J. Hobirk, E. Joffrin, A. Kallenbach, M. Kempenaars, M. Leyland, P. Lomas, G. Maddison, M. Maslov, R. McDermott, R. Neu, I. Nunes, T. Osborne, F. Ryter, S. Saarelma, P. A. Schneider, P. Snyder, G. Tardini, E. Viezzer, E. Wolfrum, the ASDEX Upgrade Team, and JET-EFDA Contributors. The effect of a metal wall on confinement in JET and ASDEX upgrade. Plasma Physics and Controlled Fusion, 55(12):124043, 2013.

[14] Costel Biloiu, Xuan Sun, Zane Harvey, and Earl Scime. An alternative method for gas temperature determination in nitrogen plasmas: Fits of the bands of the first positive system ($B^3\Pi_g \rightarrow A^3\Sigma_u^+$). Journal of Applied Physics, 101(7):073303, 2007.

[15] J. P. Booth and N. Sadeghi. Oxygen and fluorine atom kinetics in electron cyclotron resonance plasmas by timeresolved actinometry. Journal of Applied Physics, 70(2):611–620, 1991.

[16] K. Borrass, D. Coster, D. Reiter, and R. Schneider. Study of recombining gas targets. Journal of Nuclear Materials, 241-243:250 – 254, 1997.

[17] J. Brian and A. Mitchell. The dissociative recombination of molecular ions. Physics Reports, 186(5):215 – 248, 1990.

[18] C. V. Budtz-Jørgensen. Studies of electrical plasma discharges. PhD thesis, Aarhus University, Denmark, 2001.

[19] Laizhong Cai, George R. Tynan, and Eric M. Hollmann. Evidence for molecular-assisted recombination of He^+ from particle balance measurements in helium-hydrogen mixture plasmas in PISCES-A. Physics of Plasmas, 15(10):102505, 2008.

[20] Esther Carrasco, Miguel Jiménez-Redondo, Isabel Tanarro, and Víctor J. Herrero. Neutral and ion chemistry in low pressure dc plasmas of H_2/N_2 mixtures: routes for the efficient production of NH_3 and NH_4^+. Phys. Chem. Chem. Phys., 13:19561–19572, 2011.

[21] P. J. Chantry. A simple formula for diffusion calculations involving wall reflection and low density. Journal of Applied Physics, 62(4):1141–1148, 1987.

[22] P. J. Chantry, A. V. Phelps, and G. J. Schulz. Theory of electron collision experiments at intermediate and high gas densities. Phys. Rev., 152:81, 1966.

[23] J. E. Chilton, J. B. Boffard, R. S. Schappe, and C. C. Lin. Measurement of electron-impact excitation into the $3p^5 4p$ levels of argon using Fourier-transform spectroscopy. Phys. Rev. A, 57:267–277, January 1998.

[24] A. de Castro, D. Alegre, and F.L. Tabarés. Ammonia formation in N_2/H_2 plasmas on ITER-relevant plasma facing materials: Surface temperature and N_2 plasma content effects. Journal of Nuclear Materials, 463:676 – 679, 2015. PLASMA-SURFACE INTERACTIONS 21.

[25] R. D. DuBois, J. B. Jeffries, and G. H. Dunn. Dissociative recombination cross sections for NH_4^+ ions and electrons. Phys. Rev. A, 17:1314, 1978.

[26] EFDA. Fusion electricity - A roadmap to the realisation of fusion energy. https://www.euro-fusion.org/fileadmin/user_upload/EUROfusion/Documents/Roadmap.pdf, 2012.

[27] A. Eftekhari, editor. Nanostructured Materials in Electrochemistry. Wiley-VCH, 2008.

[28] L. El-Guebaly. Worldwide Timelines for Fusion Energy. The National Academies of Sciences, Engineering, and Medicine, 2017.

[29] K Ellmer, R Wendt, and K Wiesemann. Interpretation of ion distribution functions measured by a combined energy and mass analyzer. International Journal of Mass Spectrometry, 223-224:679 – 693, 2003. In Memoriam of Werner Lindinger.

[30] N. Ezumi, D. Nishijima, H. Kojima, N. Ohno, S. Takamura, S.I. Krasheninnikov, and A.Yu Pigarov. Contribution of molecular activated recombination to hydrogen plasma detachment in the divertor plasma simulator NAGDIS-II. Journal of Nuclear Materials, 266-269:337 – 342, 1999.

[31] T. Fujita, T. Hatae, T. Oikawa, S. Takeji, H. Shirai, Y. Koide, S. Ishida, S. Ide, Y. Ishii, T. Ozeki, S. Higashijima, R. Yoshino, Y. Kamada, and Y. Neyatani. High performance reversed shear plasmas with a large radius transport barrier in JT-60U. Nuclear Fusion, 38(2):207, 1998.

[32] T. Fujita, Y. Kamada, S. Ishida, Y. Neyatani, T. Oikawa, S. Ide, S. Takeji, Y. Koide, A. Isayama, T. Fukuda, T. Hatae, Y. Ishii, T. Ozeki, H. Shirai, and JT-60 Team. High performance experiments in JT-60U reversed shear discharges. Nuclear Fusion, 39(11Y):1627, 1999.

[33] V. A. Godyak. Soviet Radio Frequency Discharge Research. Delphic Associates, Falls Church, VA, 1986.

[34] Monica Grosman and Daniel G. Löffler. Kinetics of ammonia decomposition on polycrystalline tungsten. Journal of Catalysis, 80(1):188 – 193, 1983.

[35] E.A.G. Hamers, W.G.J.H.M. van Sark, J. Bezemer, W.J. Goedheer, and W.F. van der Weg. On the transmission function of an ion-energy and mass spectrometer. International Journal of Mass Spectrometry and Ion Processes, 173(1):91 – 98, 1998.

[36] Y. Hayashi, K. Jeko, H.J. van der Meiden, J.W.M. Vernimmen, T.W. Morgan, N. Ohno, S. Kajita, M. Yoshikawa, and S. Masuzaki. Plasma detachment study of high density helium plasmas in the Pilot-PSI device. Nuclear Fusion, 56(12):126006, 2016.

[37] T. Hirai, S. Panayotis, V. Barabash, C. Amzallag, F. Escourbiac, A. Durocher, M. Merola, J. Linke, Th. Loewenhoff, G. Pintsuk, M. Wirtz, and I. Uytdenhouwen. Use of tungsten material for the ITER divertor. Nuclear Materials and Energy, 9:616 – 622, 2016.

[38] A T Hjartarson, E G Thorsteinsson, and J T Gudmundsson. Low pressure hydrogen discharges diluted with argon explored using a global model. Plasma Sources Science and Technology, 19(6):065008, 2010.

[39] Odd Magnar Hole. Development and application of measurement techniques for the detection of ammonia. PhD thesis, LUND UNIVERSITY, SWEDEN, 2012.

[40] E. M. Hollmann and A. Yu. Pigarov. Measurement and modeling of molecular ion concentrations in a hydrogen reflex-arc discharge. Physics of Plasmas, 9(10):4330–4339, 2002.

[41] Jungmi Hong, Steven Prawer, and Anthony B. Murphy. Plasma catalysis as an alternative route for ammonia production: Status, mechanisms, and prospects for progress. ACS Sustainable Chemistry & Engineering, 6(1):15–31, 2018.

[42] W.T. Huntress, J.K. Kim, and L.P. Theard. On the reaction of protons with methane, ammonia, water and oxygen. Chemical Physics Letters, 29(2):189 – 190, 1974.

[43] Yukikazu Itikawa. Cross sections for electron collisions with nitrogen molecules. Journal of Physical and Chemical Reference Data, 35(1):31–53, 2006.

[44] G. Janeschitz, H.D. Pacher, G. Federici, Yu. Igitkhanov, A. Kukushkin, E. Martin, D. Post, M. Sugihara, R. Tivey, T. Ando, A. Antipenkov, S. Chiocchio, S. Hiroki, P. Ladd, H. Nakamura, R. Parker, and K. Schaubel. Proc. 15th Int. Conf. on fusion energy. IAEA, Vienna, 2:755, 1997.

[45] R. K. Janev, T. Kato, and J. G. Wang. Catalytic mechanism of divertor plasma recombination provided by hydrocarbon impurities. Physics of Plasmas, 7(11):4364–4367, 2000.

[46] R. K. Janev, D. Reiter, and U. Samm. Collision processes in low-temperature hydrogen plasmas, volume 4105 of Berichte des Forschungszentrums Jlich. Forschungszentrum, Zentralbibliothek, Jlich, 2003. Record converted from VDB: 12.11.2012.

[47] S. Kado, H. Kobayashi, T. Oishi, and S. Tanaka. Experimental investigations on hydrocarbon-enhanced mar processes in low temperature plasma in divertor simulator MAP-II. Journal of Nuclear Materials, 313-316:754 – 758, 2003. Plasma-Surface Interactions in Controlled Fusion Devices 15.

[48] A. Kallenbach, R. Dux, J. C. Fuchs, R. Fischer, B. Geiger, L. Giannone, A. Herrmann, T. Lunt, V. Mertens, R. McDermott, R. Neu, T. Pütterich, S. Rathgeber, V. Rohde, K. Schmid, J. Schweinzer, W. Treutterer, and ASDEX Upgrade Team. Divertor power load feedback with nitrogen seeding in ASDEX upgrade. Plasma Physics and Controlled Fusion, 52(5):055002, 2010.

[49] T. Kato and E. Asano. Comparison of recombination rate coefficients given by empirical formulas for ions from hydrogen through nickel. NIFS-DATA, 54, 1999.

[50] J. K. Kim and W. T. Huntress. Ion cyclotron resonance studies on the reaction of H_2^+ and D_2^+ ions with various simple molecules and hydrocarbons. The Journal of Chemical Physics, 62(7):2820–2825, 1975.

[51] Yong-Ki Kim and Jean-Paul Desclaux. Ionization of carbon, nitrogen, and oxygen by electron impact. Phys. Rev. A, 66:012708, Jul 2002.

[52] Takashi Kimura and Hiroki Kasugai. Experiments and global model of inductively coupled rf Ar/N_2 discharges. Journal of Applied Physics, 108(3):033305, 2010.

[53] Takashi Kimura and Hiroki Kasugai. Properties of inductively coupled rf Ar/H_2 plasmas: Experiment and global model. Journal of Applied Physics, 107(8):083308, 2010.

[54] I. A. Kossyi, A. Yu Kostinsky, A. A. Matveyev, and V. P. Silakov. Kinetic scheme of the non-equilibrium discharge in nitrogen-oxygen mixtures. Plasma Sources Science and Technology, 1(3):207, 1992.

[55] I. Kovacs. Rotational structure in the spectra of diatomic molecules. Akademiai Kiado, 1969.

[56] S. I. Krasheninnikov, A. S. Kukushkin, and A. A. Pshenov. Divertor plasma detachment. Physics of Plasmas, 23(5):055602, 2016.

[57] S. I. Krasheninnikov, A. Yu. Pigarov, D. A. Knoll, B. LaBombard, B. Lipschultz, D. J. Sigmar, T. K. Soboleva, J. L. Terry, and F. Wising. Plasma recombination and molecular effects in tokamak divertors and divertor simulators. Physics of Plasmas, 4(5):1638–1646, 1997.

[58] S. I. Krasheninnikov, A. Yu. Pigarov, and D. J. Sigmar. Plasma recombination and divertor detachment. Contributions to Plasma Physics, 36(23):314–318, 1996.

[59] A.S. Kukushkin, S.I. Krasheninnikov, A.A. Pshenov, and D. Reiter. Role of molecular effects in divertor plasma recombination. Nuclear Materials and Energy, 12:984 – 988, 2017. Proceedings of the 22nd International Conference on Plasma Surface Interactions 2016, 22nd PSI.

[60] A.S. Kukushkin, H.D. Pacher, V. Kotov, D. Reiter, D. Coster, and G.W. Pacher. Effect of neutral transport on ITER divertor performance. Nuclear Fusion, 45(7):608, 2005.

[61] K. Van Laer, S. Tinck, V. Samara, J. F. de Marneffe, and A. Bogaerts. Etching of low- k materials for microelectronics applications by means of a N_2/H_2 plasma: modeling and experimental investigation. Plasma Sources Science and Technology, 22(2):025011, 2013.

[62] M. A. Lieberman and A. J. Lichtenberg. Principles of Plasma Discharges and Materials Processing. Wiley, New York, 2005.

[63] D. Lumma, J. L. Terry, and B. Lipschultz. Radiative and three-body recombination in the Alcator C-Mod divertor. Physics of Plasmas, 4(7):2555–2566, 1997.

[64] G. Lj. Majstorovi and N. M. iovi. Rotational and gas temperatures of molecular deuterium in a hollow cathode glow discharge. Journal of Research in Physics, 38-39(1):11 – 22, 2015.

[65] T. D. Märk, F. Egger, and M. Cheret. Ionization of ammonia and deuterated ammonia by electron impact from threshold up to 180 ev. The Journal of Chemical Physics, 67(8):3795–3802, 1977.

[66] J. B. Marquette, C. Rebrion, and B. R. Rowe. Proton transfer reactions of H_3^+ with molecular neutrals at 30 K. Astron. Astrophys., 213:L29, 1989.

[67] ONO Masataka, T Akira, KUMITA Kentaro, Y Hiroyuki, SHIBUYA Takehisa, and KAWAMURA Kazutaka. Observation of dissociative recombination in the hydrogen sheet plasma. J. Plasma Fusion Res., 7:50–53, 2006.

[68] G.F. Matthews. Plasma detachment from divertor targets and limiters. Journal of Nuclear Materials, 220-222:104 – 116, 1995. Plasma-Surface Interactions in Controlled Fusion Devices.

[69] Jerome McAllister and Robert S. Hansen. Catalytic decomposition of ammonia on tungsten (100), (110), and (111) crystal faces. The Journal of Chemical Physics, 59(1):414–422, 1973.

[70] I. Méndez, F. J. Gordillo-Vzquez, V. J. Herrero, and I. Tanarro. Atom and ion chemistry in low pressure hydrogen dc plasmas. The Journal of Physical Chemistry A, 110(18):6060–6066, 2006. PMID: 16671676.

[71] J. B. A. Mitchell, O. Novotny, J. L. LeGarrec, A. Florescu-Mitchell, C. Rebrion-Rowe, A. V. Stolyarov, M. S. Child, A. Svendsen, M. A. El Ghazaly, and L. H. Andersen. Dissociative recombination of rare gas hydride ions: II. ArH^+. Journal of Physics B: Atomic, Molecular and Optical Physics, 38(10):L175, 2005.

[72] J.B.A. Mitchell. The dissociative recombination of molecular ions. Physics Reports, 186:215–248, 1990.

[73] J. Mlynar. Focus on: JET. European Centre of Fusion Research, EFD-R(07)91, 2007.

[74] R. Neu, A. Kallenbach, M. Balden, V. Bobkov, J.W. Coenen, R. Drube, R. Dux, H. Greuner, A. Herrmann, J. Hobirk, H. Hhnle, K. Krieger, M. Koan, P. Lang, T. Lunt, H. Maier, M. Mayer, H.W. Mller, S. Potzel, T. Ptterich, J. Rapp, V. Rohde, F. Ryter, P.A. Schneider, J. Schweinzer, M. Sertoli, J. Stober, W. Suttrop, K. Sugiyama, G. van Rooij, and M. Wischmeier. Overview on plasma operation with a full tungsten wall in ASDEX Upgrade. Journal of Nuclear Materials, 438:S34 – S41, 2013. Proceedings of the 20th International Conference on Plasma-Surface Interactions in Controlled Fusion Devices.

[75] D. Neuwirth, V. Rohde, T. Schwarz-Selinger, and ASDEX Upgrade Team. Formation of ammonia during nitrogen-seeded discharges at ASDEX Upgrade. Plasma Physics and Controlled Fusion, 54(8):085008, 2012.

[76] NIST. `https://www.nist.gov/pml/atomic-spectra-database/`, accessed 2018.

[77] M. Oberkofler, D. Douai, S. Brezinsek, J.W. Coenen, T. Dittmar, A. Drenik, S.G. Romanelli, E. Joffrin, K. McCormick, M. Brix, G. Calabro, M. Clever, C. Giroud, U. Kruezi, K. Lawson, Ch. Linsmeier, A. Martin Rojo, A. Meigs, S. Marsen, R. Neu, M. Reinelt, B. Sieglin, G. Sips, M. Stamp, and F.L. Tabares. First nitrogen-seeding experiments in JET with the ITER-like wall. Journal of Nuclear Materials, 438:S258 – S261, 2013. Proceedings of the 20th International Conference on Plasma-Surface Interactions in Controlled Fusion Devices.

[78] D. O'Connell, R. Zorat, A. R. Ellingboe, and M. M. Turner. Comparison of measurements and particle-in-cell simulations of ion energy distribution functions in a capacitively coupled radio-frequency discharge. Physics of Plasmas, 14(10):103510, 2007.

[79] N. Ohno, N. Ezumi, S. Takamura, S. I. Krasheninnikov, and A. Yu. Pigarov. Experimental evidence of molecular activated recombination in detached recombining plasmas. Phys. Rev. Lett., 81:818–821, Jul 1998.

[80] A. Okamoto, S. Kado, S. Kajita, and S. Tanaka. Laser thomson scattering system applicable to low-temperature plasma in the divertor simulator MAP-II. Review of Scientific Instruments, 76(11):116106, 2005.

[81] A. Okamoto, S. Kado, K. Sawada, Y. Kuwahara, Y. Iida, and S. Tanaka. Contribution of hydrogen molecular assisted recombination processes to population of hydrogen atom

in divertor simulator MAP-II. Journal of Nuclear Materials, 363-365:395 – 399, 2007. Plasma-Surface Interactions-17.

[82] ITER Organization. https://www.iter.org/, 2018 (accessed September 28, 2018).

[83] Y. K. Peng and P. T. Dawson. Study of the interaction of ammonia with tungsten surfaces by thermal desorption spectrometry. The Journal of Chemical Physics, 54(3):950–961, 1971.

[84] A. Y. Pigarov and S. I. Krasheninnikov. Application of the collisional-radiative, atomic-molecular model to the recombining divertor plasma. Physics Letters A, 222:251–257, February 1996.

[85] R. A. Porter and W. R. Harshbarger. Gas rotational temperature in an rf plasma. J. Electrochem. Soc., 126:460, 1979.

[86] P-H Rebut. The JET preliminary tritium experiment. Plasma Physics and Controlled Fusion, 34(13):1749, 1992.

[87] M.L. Reinke. Heat flux mitigation by impurity seeding in high-field tokamaks. Nuclear Fusion, 57(3):034004, 2017.

[88] V. Rohde and M. Oberkofler. Ammonia production in nitrogen seeded plasma discharges in ASDEX Upgrade. Journal of Nuclear Materials, 463:672 – 675, 2015. PLASMA-SURFACE INTERACTIONS 21.

[89] S. Grünhagen Romanelli, S. Brezinsek, B. Butler, J. P. Coad, A. Drenik, C. Giroud, S. Jachmich, T. Keenan, U. Kruezi, M. Mozetic, M. Oberkofler, A. Parracho, M. Romanelli, R. Smith, J. Yorkshades, and JET-EFDA Contributors. Gas analyses of the first complete JET cryopump regeneration with ITER-like wall. Physica Scripta, 2014(T159):014068, 2014.

[90] B.R. Rowe and J.B. Marquette. CRESU studies of ion/molecule reactions. International Journal of Mass Spectrometry and Ion Processes, 80:239 – 254, 1987.

[91] Takeshi Sakamoto, Haruaki Matsuura, and Hiroshi Akatsuka. Spectroscopic study on the vibrational populations of N_2 $C\Pi_3$ and $B\Pi_3$ states in a microwave nitrogen discharge. Journal of Applied Physics, 101(2):023307, 2007.

[92] P. A. Schneider, E. Wolfrum, M. G. Dunne, R. Dux, A. Gude, B. Kurzan, T. Pütterich, S. K. Rathgeber, J. Vicente, A. Weller, R. Wenninger, and the ASDEX Upgrade Team. Observation of different phases during an ELM crash with the help of nitrogen seeding. Plasma Physics and Controlled Fusion, 56(2):025011, 2014.

[93] M. B. Shah, D. S. Elliott, and H. B. Gilbody. Pulsed crossed-beam study of the ionisation of atomic hydrogen by electron impact. Journal of Physics B: Atomic and Molecular Physics, 20(14):3501, 1987.

[94] M. Shimada. Experimental and numerical studies of neutral gas depletion in an inductively coupled plasma. PhD thesis, UNIVERSITY OF CALIFORNIA SAN DIEGO, 2006.

[95] Harmeet Singh, J. W. Coburn, and David B. Graves. Recombination coefficients of O and N radicals on stainless steel. Journal of Applied Physics, 88(6):3748–3755, 2000.

[96] D. Smith and N.G. Adams. The selected ion flow tube (Sift): Studies of ion-neutral reactions. Advances in Atomic and Molecular Physics, 24:1 – 49, 1988.

[97] M. Sode, W. Jacob, T. Schwarz-Selinger, and H. Kersten. Measurement and modeling of neutral, radical, and ion densities in H_2-N_2-Ar plasmas. Journal of Applied Physics, 117(8):083303, 2015.

[98] M. Sode, T. Schwarz-Selinger, and W. Jacob. Ion chemistry in H_2-Ar low temperature plasmas. Journal of Applied Physics, 114(6):063302, 2013.

[99] M. Sode, T. Schwarz-Selinger, and W. Jacob. Quantitative determination of mass-resolved ion densities in H_2-Ar inductively coupled radio frequency plasmas. Journal of Applied Physics, 113(9):093304, 2013.

[100] M. Sode, T. Schwarz-Selinger, W. Jacob, and H. Kersten. Surface loss probability of atomic hydrogen for different electrode cover materials investigated in H_2-Ar low-pressure plasmas. Journal of Applied Physics, 116(1):013302, 2014.

[101] H. C. Straub, P. Renault, B. G. Lindsay, K. A. Smith, and R. F. Stebbings. Absolute partial cross sections for electron-impact ionization of H_2, N_2, and O_2 from threshold to 1000 eV. Phys Rev A., 54:2146–2153, September 1996.

[102] K. Tao, D. Mao, and J. Hopwood. Ionized physical vapor deposition of titanium nitride: A global plasma model. Journal of Applied Physics, 91(7):4040–4048, 2002.

[103] V. Tarnovsky, H. Deutsch, and K. Becker. Cross-sections for the electron impact ionization of $ND_x(x = 1 - 3)$. International Journal of Mass Spectrometry and Ion Processes, 167-168:69 – 78, 1997. In Honour of Chava Lifshitz.

[104] E. Tatarova, F. M. Dias, B. Gordiets, and C. M. Ferreira. Molecular dissociation in N_2-H_2 microwave discharges. Plasma Sources Science and Technology, 14(1):19, 2005.

[105] G. De Temmerman. Report mechanisms of ammonia formation in low-T plasmas and fusion-relevant conditions. ITER report, No.ITER_D_QFF9XY, 2015.

[106] E. G. Thorsteinsson and J. T. Gudmundsson. A global (volume averaged) model of a nitrogen discharge: I. steady state. Plasma Sources Science and Technology, 18(4):045001, 2009.

[107] G. R. Tynan. Neutral depletion and transport mechanisms in large-area high density plasma sources. Journal of Applied Physics, 86(10):5356–5364, 1999.

[108] G. R. Tynan, A. D. Bailey, G. A. Campbell, R. Charatan, A. de Chambrier, G. Gibson, D. J. Hemker, K. Jones, A. Kuthi, C. Lee, T. Shoji, and M. Wilcoxson. Characterization of an azimuthally symmetric helicon wave high density plasma source. Journal of Vacuum Science & Technology A, 15(6):2885–2892, 1997.

[109] L. Vikor, A. Al-Khalili, H. Danared, N. Djuric, G.H. Dunn, M. Larsson, A. Le Padellec, S. Rosaen, and Af Ugglas M. Branching fractions in the dissociative recombination of NH_4^+ and NH_2^+ molecular ions. Astron. Astrophys., 344:1027–1033, apr 1999.

[110] U. Wenzel, K. Behringer, A. Carlson, J. Gafert, B. Napiontek, and A. Thoma. Volume recombination in divertor I of ASDEX Upgrade. Nuclear Fusion, 39(7):873, 1999.

[111] Robert C. Wetzel, Frank A. Baiocchi, Todd R. Hayes, and Robert S. Freund. Absolute cross sections for electron-impact ionization of the rare-gas atoms by the fast-neutral-beam method. Phys. Rev. A, 35:559–577, Jan 1987.

[112] Jung-Sik Yoon, Mi-Young Song, Jeong-Min Han, Sung Ha Hwang, Won-Seok Chang, BongJu Lee, and Yukikazu Itikawa. Cross sections for electron collisions with hydrogen molecules. Journal of Physical and Chemical Reference Data, 37(2):913–931, 2008.

[113] M. Yousfi and M. D. Benabdessadok. Boltzmann equation analysis of electronmolecule collision cross sections in water vapor and ammonia. Journal of Applied Physics, 80(12):6619–6630, 1996.

[114] Seokmin Yun, Kurt Taylor, and George R. Tynan. Measurement of radial neutral pressure and plasma density profiles in various plasma conditions in large-area high-density plasma sources. Physics of Plasmas, 7(8):3448–3456, 2000.